FRAGMENTATION OF A BRITTLE POLYMERIC TONER LINE CAUSED BY SWELLING OF A PAPER SUBSTRATE DURING IMMERSION IN WATER

A Dissertation Submitted by

Joel C. Panek

B.S. 1992, Michigan Technological University

M.S. 1994, Institute of Paper Science and Technology

in partial fulfillment of the requirements
of the Institute of Paper Science and Technology
for the degree of Doctor of Philosophy,
Atlanta, GA

February 1999

FRAGMENTATION OF A BRITTLE POLYMERIC TONER LINE CAUSED BY SWELLING OF A PAPER SUBSTRATE DURING IMMERSION IN WATER

A Dissertation Submitted by

Joel C. Panek

B.S. 1992, Michigan Technological University

M.S. 1994, Institute of Paper Science and Technology

in partial fulfillment of the requirements
of the Institute of Paper Science and Technology
for the degree of Doctor of Philosophy,
Atlanta, GA

February 1999

ABSTRACT

Recycling of paper that was printed with polymeric toner (laser printing, photocopying) consists of repulping the paper then removing the toner from the paper fiber. Repulping involves immersing the paper in water and applying mechanical forces to disintegrate the paper into an aqueous slurry of toner particles and fiber. The ability to remove the toner from the slurry is affected by the size and shape of toner particles. This thesis addresses the fragmentation of the toner into smaller particles during the initial immersion of paper in water before mechanical forces are applied.

Toner on paper was modeled as composite consisting of a brittle, hydrophobic line on a ductile, hygroscopic substrate. The line fractures into segments (fragmentation) due to stresses that develop from expansion of the substrate due to absorption of water. The fragmentation of the toner line on paper was best described with a bond-site model that was developed in this thesis. The bond-site model is based on the Kelly-Tyson stress transfer model in which the interface is assumed to yield plastically. This model includes discrete bond-sites to account for the discontinuity of the toner-paper interface. Based on the model, the average segment length after fragmentation increases with:

- increasing effective thickness of the toner line
- increasing tensile strength of the toner line
- increasing distance between toner-paper bonds
- decreasing effective length per toner-paper bond
- decreasing shear strength of the toner-paper bond

Fragmentation was experimentally quantified using model samples of toner lines on paper and cellulose acetate. The samples were immersed in water and distance between cracks (segment length) was measured. The average segment length ranged from 100 to 400 microns and the coefficient of variation was approximately 54% for all sample sets. The segment length distribution was empirically fitted with a gamma curve, using parameters calculated from the mean and variance of the data.

The fragmentation experiments showed that cellulose acetate cannot be used as a model substrate for studying the fragmentation of toner on paper. The toner-cellulose acetate interface is elastic and cleanly fractures rather than yields, prohibiting transfer of the results.

TABLE OF CONTENTS

LIST OF FIGURES

LIST OF TABLES

LIST OF SYMBOLS AND NOMENCLATURE

A	cross-sectional area of line [μm^2]
A_f	cross-sectional area of fiber [μm^2]
A/W	effective thickness of line [μm]
d	fiber diameter [μm]
$\bar{e}$	effective bond length [μm]
$\dot{e}$	fractional effective bond length
E	tensile modulus of line [MPa]
F_x	force along axis of line [N]
h	effective line thickness [μm]
H	proportionality constant for Cox model (Eq. 3-9)
$\bar{i}$	ineffective length per bond [μm]
l	distance along line [μm]
$\bar{l}$	bond-spacing [μm]
l_c	critical line length [μm]
L	length of line segment [μm]
$\bar{L}$	expected segment length [μm]
n	number of bond-sites
n_c	critical bond-site number
$\bar{n}_c$	expected critical bond-site number (whole number)
N	segment number
N_i	segment number equals i
$\bar{N}$	expected segment number
p	perimeter of fiber [μm]
w	width of line [μm]
x	distance along line [μm]
β	defined in Eq. 3-9
ε	strain [$\mu m/\mu m$]
ε_S	strain in substrate
ε_c^C, ε_c^A	critical substrate strains for cohesive and adhesive failure, respectively
σ	axial stress in line [MPa]
σ_l	axial stress at distance l [MPa]
σ_c	critical axial stress [MPa]
σ^m	maximum axial stress [MPa]
$\Delta\sigma$	change in axial stress [MPa]
$\Delta\sigma_B$	change in axial stress over a single bond-site [MPa]

τ	interfacial shear stress [MPa]
τ^m	maximum shear stress [MPa]
τ_y	yield strength of the substrate [MPa]
τ_c	critical shear stress [MPa]
τ_β	shear strength of a toner-paper bond [MPa]

1 INTRODUCTION

Toner-printed paper is a major component of office waste paper. The value of recycled office waste paper depends in part on the amount and type of contaminants (including toner particles) remaining after recycling. The removal of contaminants from paper fibers (deinking) is conventionally done on an aqueous slurry of the waste paper. Deinking may be classified into two processes: preparing the paper furnish for separation processes (repulping) and separating contaminants from paper fibers. Repulping involves the initial disintegration of the waste paper into an aqueous slurry. The physical state of the contaminants in the output stream from repulping has a large effect on the effectiveness of contaminant separation.

Repulping of toner-printed paper produces a fiber slurry with toner particles that are typically plate-like (one dimension much smaller than the other two). These particles have been difficult to separate from the fibers in conventional deinking processes because of their shape, a large size distribution (longest dimensions), and fibers remaining attached to the particles (Vidotti, 1994; Johnson and Thompson, 1994). It appears that the best way to control the particle size and shape is to either agglomerate the particles to a larger, three-dimensional shape (Borchardt *et al.*, 1994) or to use excessive mechanical treatment to break the particles down to a smaller size (Kakogiannos *et al.*, 1997). A better understanding of the fragmentation of toner should lead to more efficient processes for producing particles of an optimum size.

The fragmentation of toner is typically discussed in terms of the application of external mechanical forces during repulping and kneading. However, Vander Wielen *et al.* (1999) showed that significant fracture of toner may occur upon immersion of toner-printed paper in water, without any external mechanical forces. Fracture occurred as a result of the mechanical stress between the swelling paper and the non-swelling toner. A printed line of toner was observed to fracture into segments of uniform length. The segment length gives an approximate

measurement of the toner particle size produced through the swelling of paper when first immersed in a repulper.

The objective of this thesis is to produce a model for the fragmentation of a line of toner during immersion of toner-printed paper into water. A theoretical model will be discussed to mathematically describe the fragmentation and identify the important parameters. Fragmentation is quantified as the distance between cracks (segment length) that form in toner lines upon immersion in water. An experimental technique for preparing lines of toner on paper and cellulose acetate will be described.

1.1 Repulping Toner-Printed Paper

1.1.1 Repulping - general

The purpose of repulping is to break up the paper and contaminants so that the contaminant can be more easily separated. Waste paper is added to water to produce a slurry that can range from an aqueous suspension (low consistency, 3 to 8% paper to water) to a wet solid (medium to high consistency, 8 to 40%) (Fallows, 1992; Cleveland, 1993). Mechanical forces are applied to the slurry to exceed the strength of the fiber-fiber bonds of the paper and disintegrate it into fibers (defibering). The pulper temperature, consistency of the slurry, time of repulping, power input, and chemical addition are adjusted to optimize repulping.

Fallows (1992) proposed that the mechanical forces in a repulper include direct mechanical forces (paper hitting rotors), fiber-fiber shear forces, shear stress from differences in flow velocity, attrition, and mechanical shearing between two plates. The magnitude of each of these forces is believed to be largely a factor of the consistency of the pulp and the type of rotor used. Low consistency (3 to 8%) repulping uses a flat, attrition-type rotor with a low clearance between the plate and rotor. Medium (sometimes referred to as high) consistency (8 to 18%) repulping uses a screw rotor, which forces the stock downward and inward to cause fiber-fiber

friction. High consistency (15 to 40%) uses a rotating drum which breaks up the furnish by essentially picking up the furnish and dropping it (Cleveland, 1993). Bennington *et al.* (1998) showed that the rate of defibering is a function of the contact between the rotor and slurry, strength of the paper structure, and the force from the rotor.

1.1.2 Repulping toner-printed paper

Research on the repulping of toner-printed paper has primarily involved laboratory-scale repulpers. Typically, the results of repulping are quantified with the size range of toner particles remaining after testing or the brightness of handsheets. Tests have included repulping consistency, time, temperature, and chemical addition.

1.1.2.1 Process conditions

The effect of increasing mechanical forces during repulping has been clearly established. In general, increasing mechanical force input decreases the particle size (Dorris and Sayegh, 1997; Berg *et al.*, 1997). The mechanical forces may be increased by increasing the repulping consistency or time. The effect was explained by the expected increase in shear forces on the particles to break the larger particles down into smaller ones.

Vander Wielen *et al.* (1999), Berg *et al.* (1997), and Kakogiannos *et al.* (1997) all showed that a lower repulping temperature produces relatively more smaller particles, because the toner is more brittle at the lower temperature. Berg *et al.* (1997) and Kakogiannos *et al.* (1997) also both showed that typically the largest toner particles have fibers attached to them, except at higher temperatures at which there were very few particles with toner attached. They attributed this to weaker bonding between the toner and paper at the higher repulping temperature.

The effect of chemical addition is much less clear. Vander Wielen *et al.* (1999) and Berg *et al.* (1997) did not find a significant effect of pH on the particle size distribution formed upon

repulping, while Borchardt and Rask (1993) did see a difference. Borchardt and Rask suggested that esterfication of a polyester resin was occurring at a higher pH. It appears that the effect of pH depends on the composition of the toner; however, there has not been any work clearly showing the effect of pH on a toner's mechanical properties.

1.1.2.2 Effects of furnish properties

A number of groups have attempted to relate the properties of toner, paper surface, and the printing process to both the size distribution of toner after repulping and the deinkability of the toner. Cathie *et al.* (1992, 1993) clearly showed an effect from the base paper and the printer used, but were unable to produce evidence on why they were different. They suggested that the print density and degree of fusing may have an effect.

Vidotti *et al.* (1993) found the size distribution of toner particles from repulping to be dependent on the furnish. They suggested that the size distribution was affected by the composition of the toner, namely the effect of the composition on the thickness of the toner layer and how the toner breaks up. It was pointed out that the fusing conditions, which were not studied in this case, may be an important factor.

Snyder and Berg (1994) showed a difference in toner particle size distributions and flotation efficiencies between faster-printing and slower-printing machines. They hypothesized that slower-printing machines produce a layer with a higher print density and a more intimate fusing to the paper. It is believed that this will result in larger toner particles and a greater number of particles retaining fibers. The authors suggested a relation between particle size and fiber retention, and that the retention of fibers is believed to decrease the flotation efficiency.

Dorris and Sayegh (1997) proposed that the cohesiveness of a printed toner layer governs the fragmentation of toner in a repulper. The cohesion of a toner layer was characterized in terms of apparent print thickness. The apparent print thickness is a hypothetical thickness of

toner, which is defined as the mass of toner per unit print area divided by the density of the toner. Repulping experiments showed that the speck area of particles larger than 250 microns increased with increased apparent layer thickness. They showed that print with a lower apparent layer thickness had a smaller area of large particles after repulping, i.e., these "thinner" layers were more easily broken up into smaller particles. They also showed that the size of the print area may have an effect on the size of particles resulting from repulping. In a print from one experiment, they showed that repulping of a solid print resulted in lower speck area coverage (for specks >250 microns) than a smaller dot pattern, thus fewer large particles. They also proposed that toner does not detach from the surface of paper; rather, that the network of paper disintegrates and fibers are progressively detached from the toner. They support this by the observation that fibers remain attached to toner particles and that the dots used in the printed pattern remained essentially intact. Printing with a layer of toner decreased the rate of defibering of a sheet since flakes of paper were apparently held together by a layer of toner.

1.1.3 Model studies on repulping toner-printed paper

There have been relatively few studies to isolate the mechanisms occurring during repulping. In nearly all cases, the results were reported in terms of percentage toner removal, which is largely determined by optical measurements on handsheets prepared after deinking. While these methods will provide a comparative relation within the experiment, they do not always give a quantitative result that can be extrapolated to other systems. Studies of model systems have the advantage of isolating important mechanisms. Understanding of the mechanisms provides a more solid basis for interpreting results and predicting effects.

Morsink and Daane (1992) simulated the effect of mechanical forces on the detachment of toner in an aqueous surfactant solution. Toner-printed sheets were wrapped around a cylinder and immersed in solution. A foam rubber roller made contact with the sheet to simulate

mechanical force. The results were quantified in terms of regained whiteness and particle size distribution. An alkaline environment promoted the best detachment, while an acidic environment produced better removal than a neutral environment. Increased temperature improved removal, as did increasing the hydrophilic content of the surfactant. Again, this test does not necessarily simulate any mechanisms in repulping and lacks a theoretical basis. The detachment of toner in this experiment is primarily an effect of the friction of the rubber roller against the toner. It is possible that these conditions affected the state of the roller and the friction between the roller and the toner rather than affecting the attachment of the toner to the paper.

1.1.4 Separation of toner particles

The size and shape of toner particles resulting from conventional repulping are frequently described as incompatible with a typical deinking system. These particles are considered too large for washing and flotation, while too small and flat for separation by centrifugal cleaning and screening. Vidotti *et al.* (1994) showed that the flotation of toner strongly depends on the particle size, but also pointed out that this is a phenomenon that is not well understood. Johnson and Thompson (1994) showed that fibers adhering to toner will reduce flotation efficiency. They explain this effect in terms of the increased hydrodynamic volume of the toner and attached fibers when compared to the volume of the toner only. They found that retention of fibers on toner is common, and that the fibers cannot be completely separated.

1.1.5 Summary – repulping toner-printed paper

While the effects of different variables have been shown and there are no major discrepancies in the results from different researchers, there is still a lack of precise descriptions of the physical mechanisms. Increasing repulping consistency and time produced smaller particles, while increasing temperature produced larger particles. The effect of pH differed,

apparently due to the toner used. Characterization of printed toner is largely qualitative. Differences were largely attributed to effects of the fusing process, including the thickness and cohesiveness of the toner layer and the degree of fusing of toner to paper.

1.2 Printed Toner on Paper

1.2.1 Toner

Toner is the "ink" used in photocopier and laser printers. It consists of a polymeric binder containing a coloring agent in addition to other components to modify its properties. The binders may be co-polymers or polymer blends. The polymers used include polystyrene acrylates, polystyrene butadienes, polyesters, polyethylene, polypropylene, and epoxies (Gruber and Julien, 1991). The base polymers have glass transition temperatures from 50 to 150°C and molecular weights from 500 to 100,000. The toner typically has a T_G from 50 to 65°C, and the polymers may be blended to reach this range (Mort, 1989). The binder may comprise from 60 to 95 wt.-% of the toner, typically 90% or more. The main additive to the base polymer is the colorant, mainly carbon black and iron oxide (Gruber and Julien, 1991). Carbon black may be used at levels from 5 to 15 wt.-%, while the iron oxide may be used up to 60 wt.-%. The toner also may contain charge control additives, surface additives, magnetic additives, and waxes. Charge control agents include quaternary ammonium salts, nigrosine, acidified carbon blacks, fumed silica, and metal complexes. Fumed silica is often used as a surface additive to provide good flow properties for toner powder. Release agents, such as silicone oil, may be used to assist copy removal from rolls.

1.2.2 Printing process

The structure of the toner layer and its adhesion to paper is determined by the fusing steps in the xerographic process. Fusing is the process in which toner particles coalesce together and flow to conform intimately to the paper structure below it. Prime (1983) breaks this down into

heating of the toner (above its glass transition temperature), sintering of the toner particles, spreading of the molten toner over the fibers, capillary penetration of molten toner into pores, and solidification of the toner by cooling.

The adhesion of toner to paper is affected by the fusing conditions, viscoelastic properties of toner, and the relative surface energies of the toner and paper (Prime, 1983; Forgo *et al.,* 1993; Lee, 1975; Borch, 1982). Borch (1982) measured the adhesive strength of toner to paper by measuring the joint strength of two pieces of paper held together by an extruded toner filament. The results showed that the adhesive strength is at a maximum when the surface energies of the two solid phases are equal. The surface energy of the paper was decreased by the addition of a sizing agent.

1.3 Fragmentation

There is much work in the literature on the fragmentation of a brittle component of a composite under load to the composite (see references in Secs. 1.3.1 and 1.3.2). In this work, toner on paper will be modeled as a brittle hydrophobic line on a hygroscopic substrate. The load in this composite originates from hygroexpansion of the substrate. This section will address the general concepts of fragmentation and the basis for the models. The particular application of the models for toner on paper will be discussed in more detail in the theoretical section.

1.3.1 Fragmentation phenomenon

Fragmentation, as studied here, is the multiple fracture of brittle component of a composite into smaller segments. This phenomenon has been observed and modeled in composites of brittle fibers embedded in a matrix (*e.g.,* carbon fibers in epoxy) (see Sec. 1.3.2) or brittle films on a substrate (*e.g.,* ceramic on metal) (Agrawal and Raj, 1989; Hu and Evans, 1989; Wojciechowski and Mendolia, 1989). The fragmentation is a result of a mismatch in material properties of two well-bonded components. Under load, the brittle component fractures

by transfer of stress through the interface. The fiber fractures as long as the maximum axial stress exceeds the fiber's critical stress. The axial stress is determined by the shear stress transferred through the interface. Fracture is halted once the stress no longer reaches the critical fracture stress. The stress transfer is limited by the interface because the interface may either fracture or yield.

1.3.2 Single-fiber fragmentation test

Much of the modeling of fragmentation has been done by researchers in the area of single-fiber fragmentation testing. Researchers have used the fragmentation phenomenon as an analytical tool for studying the interfacial properties of composites. The test has been the subject of reviews (Feillard, 1994; Tripathi and Jones, 1998), and has been described in general composite textbooks (Gibson, 1994). This approach has become a common test for the fiber strength and interfacial shear strength for composites of embedded carbon fibers in an epoxy matrix. However, there are many criticisms of the material properties that are extracted from the test (Narkis *et al.*, 1988; Melantis *et al.*, 1992, Piggott, 1994). Even with extensive work, modeling fragmentation is complex and there does not appear to be a universally accepted approach (Feillard, 1994; Tripathi and Jones, 1998). The fragmentation test has been criticized because there has not yet been shown a clear relationship between the mean segment length and the theoretical critical length, the state of stress along the interface may be more complex than can be described by a single model, and an accurate measurement of the fiber strength is complicated. An accurate measurement of the fiber strength is complicated because the measured strength is dependent on length and must be extrapolated to the segment length. Also, the strength may be different in air (as measured) than embedded in the matrix.

In general, the fiber-matrix bond strength (or fiber strength) is derived from measurements of the lengths of fiber segments remaining after load has been applied to the

composite (Ohsawa *et al.*, 1978; Miwa *et al.* 1980). The composite is a single fiber aligned along the axis of load in a matrix. The fiber is assumed to fracture into segments with an average length equal to a factor of a critical length predicted from models of the stress distribution. The critical length is the length along the fiber that is necessary for the axial stress to reach the critical stress of the fiber. The Kelly-Tyson model (Kelly and Tyson, 1965a and 1965b) and Cox model (Cox, 1952) (shear-lag model) are conventionally used as a basis. The models differ in that the Kelly-Tyson model is for an interface that deforms plastically or slips, while the Cox model is for an interface that deforms linearly elastically.

2 APPROACH TO THE PROBLEM

Problem Statement

The size of toner fragments has a significant effect on deinking of toner-printed paper; however, a clear explanation of the fragmentation mechanism has not been developed. This research will produce a model for the fragmentation of toner during the initial processing step of immersion of toner-printed paper into water (before application of mechanical energy during repulping).

Significance of Research

It is difficult to completely separate toner from paper fibers during deinking of toner-printed paper, which limits the value of the deinked product. Effective separation is restricted by the size of the toner particles in the process streams. The mechanisms that determine the size of particles are not clear, which hinders control of the size (thus separation). This research will develop a model to explain the fracture of printed toner into smaller fragments during the initial step of immersion in water. The model will describe the fragmentation mechanism and identify the controlling parameters. The results will indicate the feasibility of controlling the particle size.

Theoretical Base for the Research

Stress transfer models have been used to explain the fragmentation of fibers embedded in a strained matrix. The models are based on the transfer of load to the fibers through the interface and fracture of the fiber when the fiber's critical stress has been exceeded. The fragmentation length is derived as the distance along the fiber for the axial stress to reach the critical stress. This research will determine the appropriate model to use for the fragmentation of toner on paper. In general, the model will predict the fragmentation of a brittle polymer line that is adhered to a substrate that swells due to absorption of water.

Research Approach

The fragmentation of a toner line will be generalized in terms of a stress-transfer model. The approach is based on the premise that printed toner on paper is a composite and that hygroexpansion of the paper produces cracks in the toner line. The fragmentation will be quantified as the distance between cracks (segment length) in the toner line. An appropriate stress transfer model will be selected that best describes the experimental results.

Printed toner on paper will be represented by model samples of toner lines on paper. The effects of hygroexpansion will be isolated by immersing the samples in water without any applied mechanical forces. The immersed samples are observed under a light microscope to measure the distance between cracks in the toner line. The data will be presented as average segment length versus effective thickness of the toner line.

3 THEORETICAL MODEL

3.1 Introduction

The fragmentation of toner on paper immersed in water will be described with stress transfer models. Toner on paper is considered a composite of a hydrophobic polymer line on a hygroscopic substrate. Stress transfer models can describe the axial stress on the line due to hygroexpansion of the substrate. Fragmentation is determined based on a critical length for the axial stress to reach the critical fracture stress of the line.

The Kelly-Tyson, Cox, and bond-site models will be discussed. The Kelly-Tyson and Cox models are models typically used for describing the transfer of stress between materials in a composite (Gibson, 1994). Both of these models assume a continuous interface. The main difference between these two models is the assumed matrix properties, which leads to a difference in the shape of the stress distributions and the type of interfacial failure.

The bond-site model was developed in this thesis for a noncontinuous interface. It is based on the same assumptions as the Kelly-Tyson model, except the interface is represented with discrete bond-sites. Modeling with discrete bond-sites should more accurately represent the fragmentation of toner on paper.

3.1.1 Physical model of toner on paper

Toner on paper is modeled as the toner line, toner-paper bonds, and the bulk paper (Figs. 3-1, 3-2). The toner line is assumed to be a brittle, hydrophobic, one-dimensional structure, while the bulk paper is considered only as a hygroscopic substrate. The key to modeling is providing an accurate description of the bonding between toner and paper.

Fig. 3-2 shows a schematic diagram of the interfacial region between the toner and paper. The drawing on top was based on published pictures of cross-sections of toner on paper (Dorris and Sayegh, 1997; Bhateja and Gilbert, 1985a, 1985b). The interfacial region may be modeled

as being either continuous or noncontinuous. The continuous model considers only the mechanical properties of the region. The mechanics for a continuous interface can be described by either the Kelly-Tyson (Sec. 3.2) or the Cox (Sec. 3.3) model. The noncontinuous model considers both the mechanical properties and the dimensions of the bonding. These will be incorporated together into discrete bond-sites in the bond-site model (Sec. 3.4).

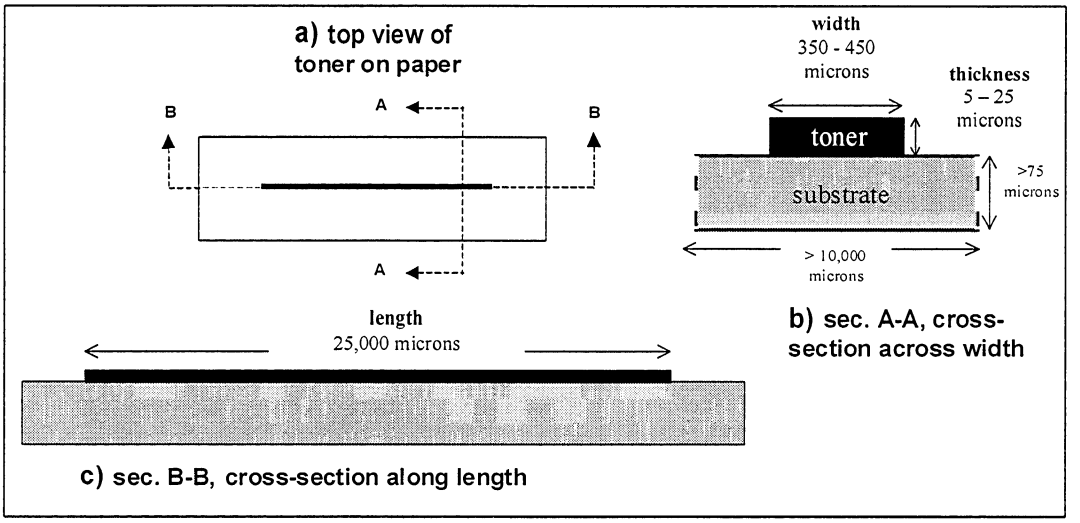

Figure 3-1: Simplified views of toner on paper. The length of the line is much greater than the thickness or width. The cross-sectional view along the length (sec. B-B) provides the basis for much of the discussion.

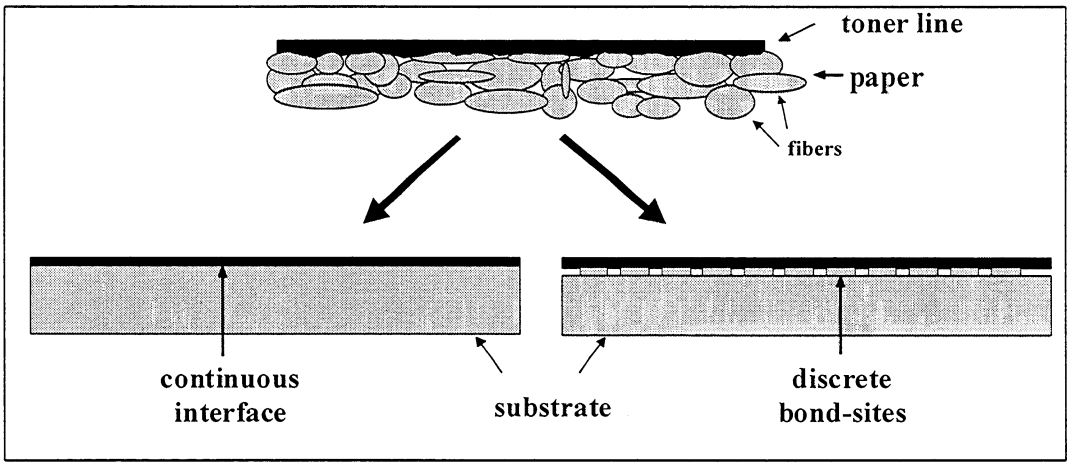

Figure 3-2: Simplification of toner on paper. The interfacial region between the toner line and paper is modeled either with a continuous interface or with discrete bond-sites.

3.1.2 Fragmentation mechanism

For simplification, the continuous model will be used here to describe the concept of fragmentation. Upon immersion in water, the substrate absorbs water and expands, while the line does not (Fig. 3-3). Because the materials are bonded together, the expansion of the substrate produces tensile stress on the line. The interfacial region between the materials is under shear forces because of a difference in deformation between the two materials. The axial stress in the line, σ, and the shear stress at the interface, τ, are the stresses that will be considered here.

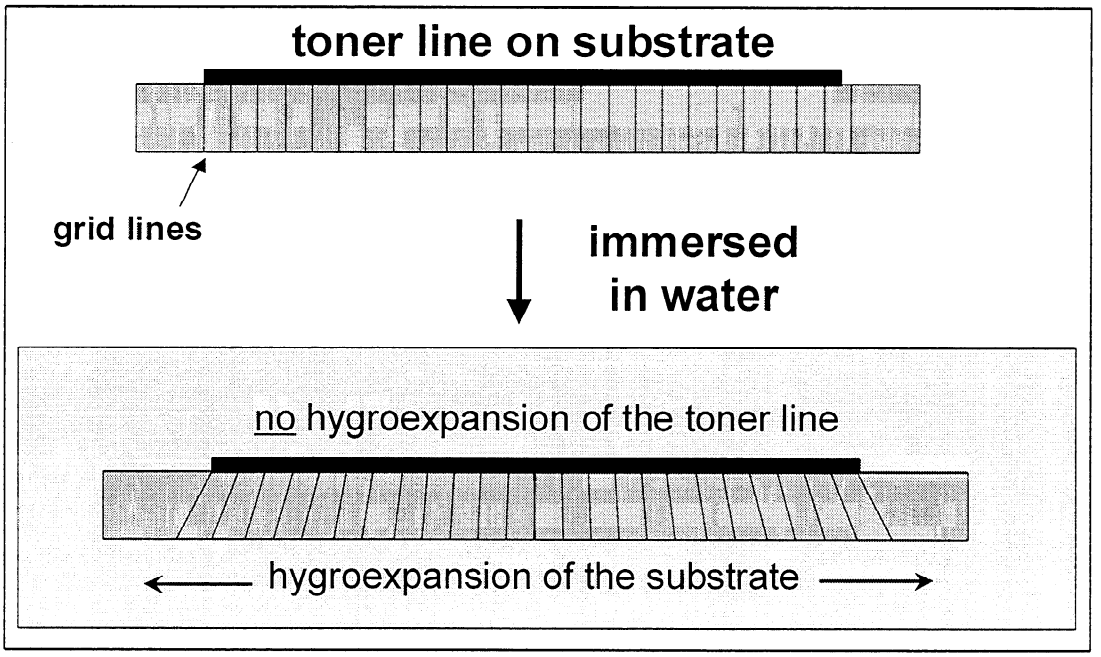

Figure 3-3: Hygroexpansion of the substrate produces axial tension on the line and shear stresses at the interface. The grid lines show the shear deformation of the substrate.

3.1.2.1 Force balance on the line

The basis for the models is a one-dimensional force balance on a differential element along the axis of the line (Fig. 3-4). In the simplified case of a line of toner on a substrate, there are shear forces only on the surface in contact with the substrate. The differential equation (Eq.

3-2) can be used to derive the axial stress from a known shear stress distribution, or the shear stress from a known axial stress.

$$\sum F_x = \tau \cdot w \cdot dx + \sigma \cdot A - (\sigma + d\sigma) \cdot A = 0 \tag{3-1}$$

$$d\sigma \cdot A = \tau \cdot w \cdot dx \tag{3-2}$$

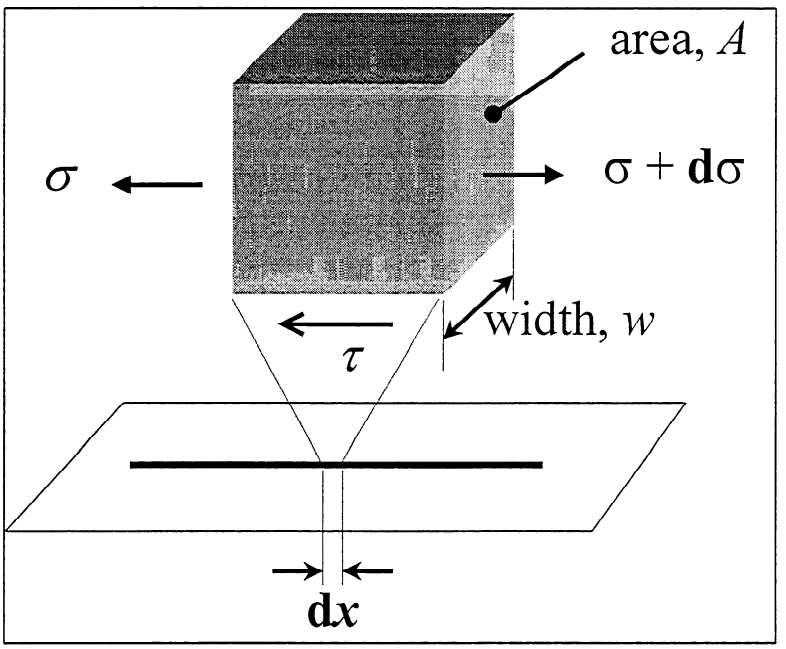

Figure 3-4: Representative volume element of the toner line. The one-dimensional force balance is based on the axial stress on the line, σ, and the shear stress at the interface, τ.

Both the Kelly-Tyson and Cox models were derived for a cylindrical geometry of the system. In the differential equation for cylindrical geometry, the cross-sectional area of the fiber, A_f, is divided by the perimeter of the fiber, p, and put in terms of the fiber diameter, d ($d/4$). In the line on a substrate system, the shear stress is transferred across the width at the base of the line, w, instead of around the fiber perimeter, p. The cross-sectional area, A (μm^2) and width, w (μm), are combined to give an effective thickness, $h = A/w$ (μm). The difference from the previously published equations developed for fibers is that $d/4$ is replaced by h.

3.1.2.2 Stress distribution

The axial and shear stresses are distributed along the length of the line depending on the properties of the line and the interface. The major difference between the Kelly-Tyson and Cox models is the properties of the interface. Both assume a linear elastic fiber (line). The Kelly-Tyson model assumes an interface that deforms plastically, while the Cox model assumes a linear elastic interface. These will be discussed in more detail in the following sections (Kelly-Tyson, Sec. 3.2; Cox, Sec. 3.3). Both the models result in an axial stress that is at a maximum at the midpoint of the line. The Kelly-Tyson model has a constant shear stress, while the Cox model has a shear stress that varies and is at a maximum at the ends.

The axial stress will be discussed in terms of an average stress across the cross-section. The stress distributions are used to identify the position along the line where the axial stress is at a maximum and where the axial stress exceeds the critical stress. There may be a distribution of stresses across the cross-section. However, at the position along the line where the average stress is at a maximum, the magnitude of stress at any point across the cross-section is also at a maximum relative to adjacent points along the axis.

3.1.2.3 Fragmentation

The line is assumed to fracture when the axial stress exceeds the line's critical stress (Fig. 3-5). The fracture of the line is halted because (a) there is not sufficient length for the stress to increase to the critical level (Kelly-Tyson and bond-site models), or (b) the interface fractures and can no longer transfer stress (Cox model). The models produce a critical length based on these criteria, from which the segment length can be estimated.

It should be noted that the critical stress refers to the strength of the line structure. This strength is not necessarily the same as the strength of the bulk material of the line. The line structure is likely relatively weaker than the bulk material because of stress concentrations arising from voids and sharp edges in the structure.

The use of the critical stress as a fracture criteria is valid assuming that the fracture strain of the line is less than the total extension of the composite. If the fracture strain is similar or greater than the total extension, the line may not fracture, even if the line is of low strength. Also, the fragmentation may become a function of the amount of extension. This introduces additional factors into the models and makes the relative strengths of the lines less meaningful. Therefore, this model should be applied to lines of low-elongation (high modulus) materials only.

The results of the models will be shown as segment length curves. This curve is the expected segment length v. effective thickness. These curves more clearly show the differences between the models, and allow the experimental data to be plotted against an independent variable.

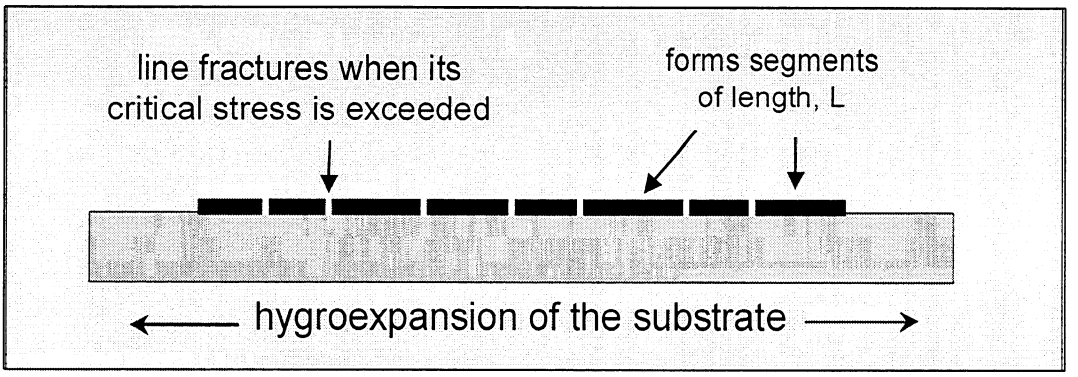

Figure 3-5: The line fractures into segments (fragmentation) when the axial stress exceeds the critical stress of the line.

3.2 Kelly-Tyson Model

Kelly and Tyson (1965a and 1965b) derived a model for the axial stress in a fiber for a composite of embedded fibers in a matrix. This model has been used extensively to describe the fragmentation of composites (Sec. 1-3). The fragmentation is limited by yield of the interface. The yield determines the length for the axial stress to reach the critical stress of the line. The critical length can be determined from a simple linear relationship.

The basic equation of the Kelly-Tyson model has been previously applied to paper (Shallhorn and Karnis, 1979; Yan and Kortsschot, 1996). This work has been on a fiber pull-out test, and does not address multiple fracture.

3.2.1 Kelly-Tyson equations

The substrate is assumed to be rigid-plastic, while the line is linear elastic. The shear stress is assumed to have reached the yield strength of the substrate, τ_y, which results in a constant shear stress along the length of the interface ($\tau = \tau_y$). The axial stress is derived from the one-dimensional force balance (Eq. 3-2). The constant shear stress results in an axial stress that increases linearly along the length (Fig. 3-6). The maximum axial stress, σ^M, in the fiber is at the midpoint, $x = l$.

$$\Delta\sigma = \frac{\tau_y}{h}\Delta x \tag{3-3}$$

$$\sigma^M = \frac{\tau_y}{h} \cdot l \tag{3-4}$$

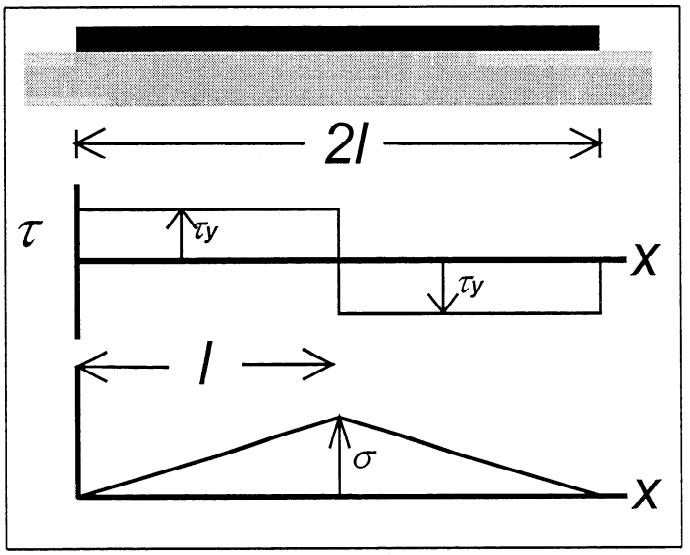

Figure 3-6: Distribution of axial and shear stresses for the Kelly-Tyson model. The axial stress, σ, is maximum at the midpoint and the shear stress, τ, is constant at the yield stress, τ_y.

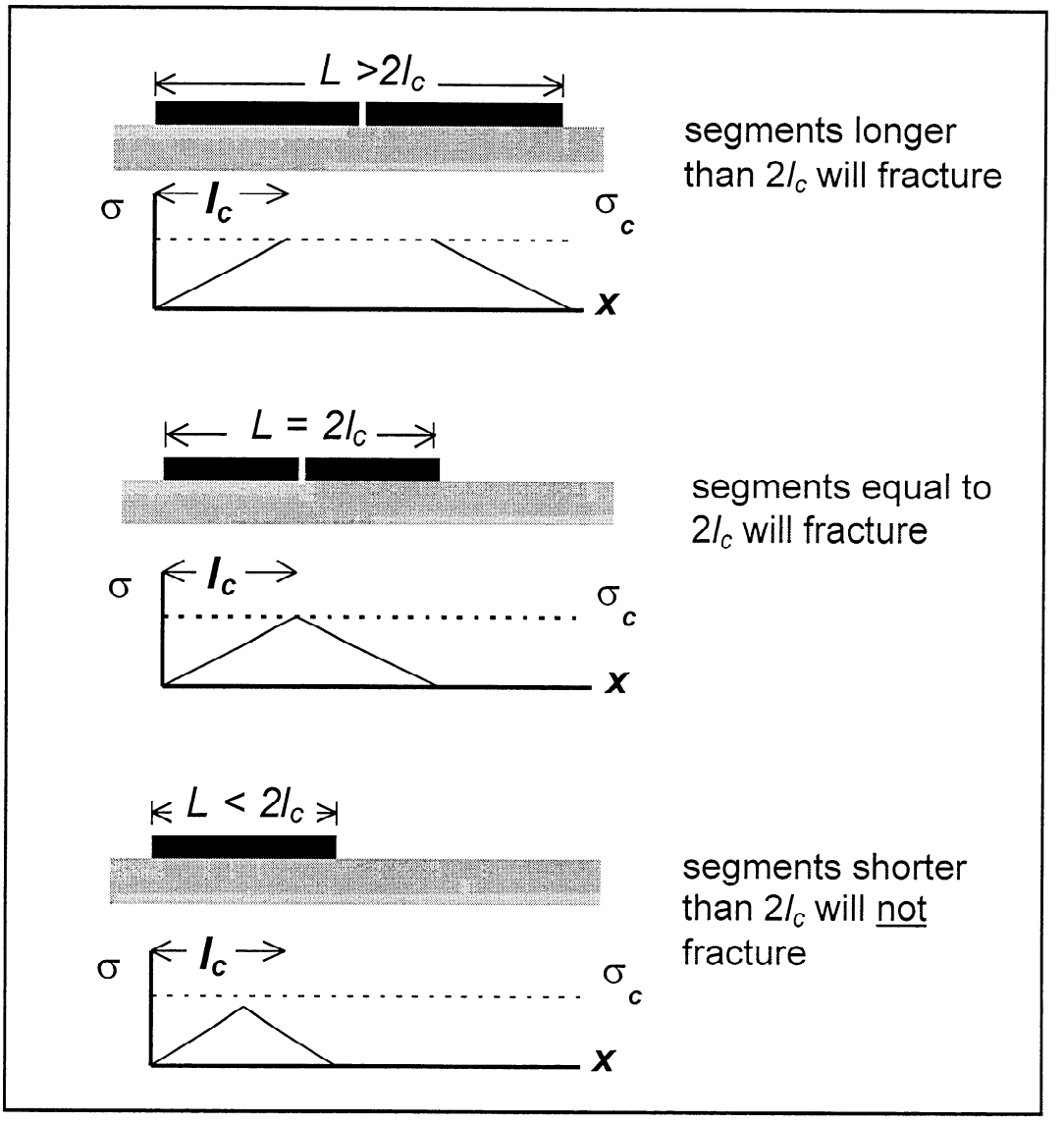

Figure 3-7: Fragmentation mechanism for the Kelly-Tyson model. Segments longer than or equal to $2l_c$ will fracture. The minimum and maximum lengths should be l_c and $2l_c$, respectively.

The critical segment length, l_c, is derived from Eq. 3-4 as the length along the line at which the maximum axial strength, σ^M equals the critical stress of the line, σ_c (Gibson, 1994).

$$l_c = \frac{\sigma_c}{\tau_y} \cdot h \tag{3-5}$$

3.2.2 Fragmentation mechanism

Under expansion of the substrate, the line will fracture until the segment length, L, is less than twice the critical length, $2l_c$ (Fig. 3-7). The segment lengths are expected to be distributed between l_c and $2l_c$ (Ohsawa, 1978).

Assuming a uniform distribution between l_c and $2l_c$, the expected segment length, $\overline{L}$, can be estimated as $\frac{3}{2}l_c$ (Eq. 3-6). Traditionally, a uniform distribution has been assumed, although there has been no experimental support for it (Tripathi and Jones, 1998). A plot of the expected length, $\overline{L}$, versus the effective thickness, h, is linear with a zero intercept.

$$\overline{L} = \frac{3}{2}\frac{\sigma_c}{\tau_y} \cdot h \tag{3-6}$$

3.3 Cox Model

Cox (1952) developed a model for the axial stress distribution in a fiber that is embedded in a continuous solid resin. The bulk of Cox's paper addressed the effect of fiber orientation on the elasticity and strength of paper. Of interest here is the section of the paper that takes into account the finite lengths of fibers (Cox, 1952, Sec. 8., Application of the Conclusions to Practical Materials). A similar model was presented by Rosen (1965).

The Cox model and its derivatives are often referred to as the shear-lag theory. The models are typically used to describe the effects of fiber length and fiber-matrix interfacial properties on the modulus and strength of the composite. It has been presented in discussions on fiber-reinforced composites (*e.g.,* Holister and Thomas, 1966; Kelly, 1973; Piggott, 1980), in standard composites texts (*e.g.,* Gibson, 1994), and has been further applied to paper (*e.g.,* Page and Seth, 1980; Perkins, 1980; Gates and Westcott, 1996). To this author's knowledge, none of the work with paper has addressed the multiple fracture of a single component (*i.e.*, fragmentation).

In this work, the model will be used to describe fragmentation of a line on a substrate. It has been previously used to study fragmentation (*e.g.,* Daoust *et al.*, 1993; Kim *et al.*, 1993; Ling and Wagner, 1993), but not as extensively as the Kelly-Tyson model. The description of fragmentation is more complex for the Cox model than the Kelly-Tyson model. The stress distributions are nonlinear functions and the fragmentation of the line is limited by the fracture of the interface, as opposed to the yield of the interface. In this section, substrate strain curves will be used to more clearly explain the fragmentation. The critical length is derived as the length at which the adhesive fracture preferentially occurs over cohesive fracture of the line.

3.3.1 Cox equations

The Cox model assumes that the rate of change of the axial load is proportional to the difference in displacement in a volume element with and without the fiber. Both the matrix and the fiber are linearly elastic, and no stress is transferred at the ends. The axial stress (Eq. 3-7) is derived in terms of the fiber modulus, E, the substrate strain with no line present, ε_S, the length of the line, $2l$, and a parameter for the geometry and material properties of the system, β. The shear stress (Eq. 3-8) can be derived from the axial stress using the one-dimensional differential equation (Eq. 3-2), as shown by Kelly (1973).

$$\sigma = E \cdot \varepsilon_S \cdot \left[1 - \frac{\cosh(\beta \cdot (l - x))}{\cosh(\beta \cdot l)}\right] \tag{3-7}$$

$$\tau = h \cdot \beta \cdot E \cdot \varepsilon_S \cdot \frac{\sinh(\beta \cdot (l - x))}{\cosh(\beta \cdot l)} \tag{3-8}$$

$$\beta^2 = \frac{H}{A \cdot E} \tag{3-9}$$

where H is a proportionality constant that is a function of the relative dimensions and mechanical properties of the components.

An example of the distribution of stresses along the length of the line is shown in Fig. 3-8. Equations for the maximum stresses are derived from Eqs. 3-7 and 3-8 based on a maximum tensile stress, σ^M, at $x = l$ and a maximum interfacial shear stress, τ^M, at $x = 0$.

$$\sigma^M = E \cdot \varepsilon_S \cdot \left(1 - \frac{1}{\cosh(\beta \cdot l)}\right) \tag{3-10}$$

$$\tau^M = h \cdot \beta \cdot E \cdot \varepsilon_S \cdot \tanh(\beta \cdot l) \tag{3-11}$$

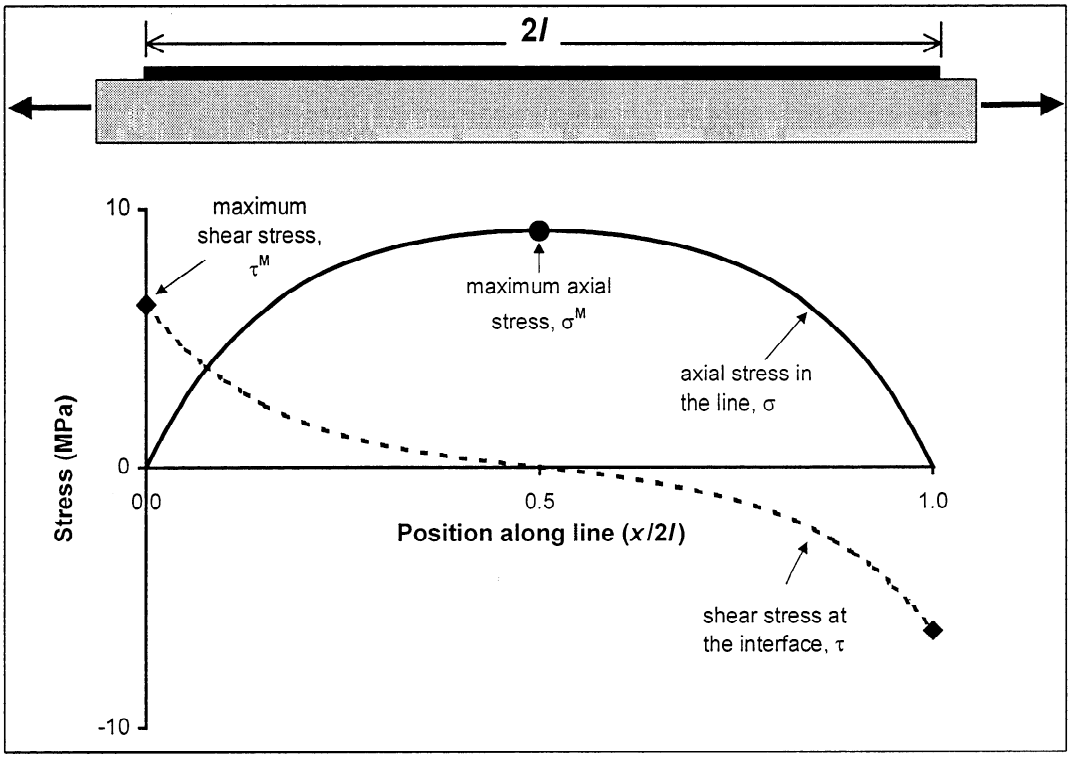

Figure 3-8: Distribution of axial and shear stresses along the length of the line based on the Cox model. The axial stress is maximum at the midpoint and the shear stresses are maximum at the ends.

3.3.2 Fragmentation mechanism

Under a load to the composite, fracture of either the line or the interface occurs when its maximum stress reaches the corresponding critical stress ($\sigma^M = \sigma_c$ or $\tau^M = \tau_c$)(Fig. 3-9). Cohesive fracture occurs at the midpoint and is assumed to occur as a clean break across the entire cross-section of the line. Adhesive fracture initiates at the ends of the line and propagates

along the interface with additional load to the composite. Adhesive fracture halts cohesive fracture and may produce complete detachment of segments.

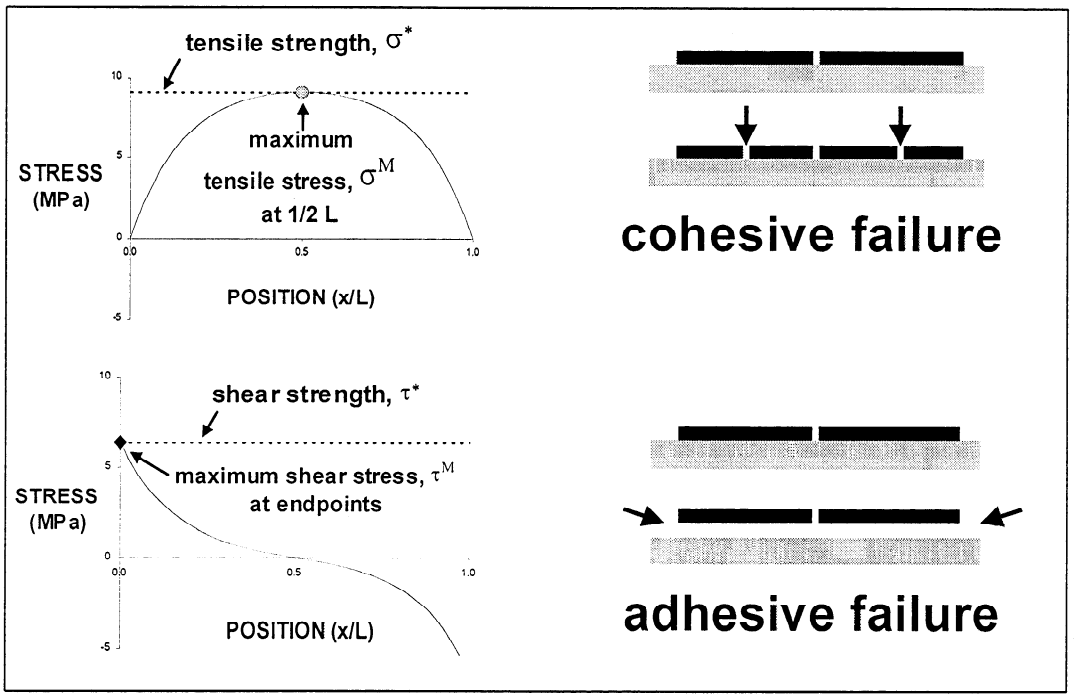

Figure 3-9: For the Cox model, cohesive or adhesive fracture occurs when the corresponding critical stress is reached.

The critical length is the segment length below which adhesive fracture preferentially occurs. Unless its length is less than the critical length, a segment will cohesively fracture into smaller segments. The critical length is determined based on the relative magnitude of stresses and critical stresses. The preferred fracture modes and the derivation of the critical length are better described in terms of critical substrate strains.

3.3.2.1 Critical substrate strains

The axial and shear stress can be related to each other in terms of the strain of the substrate. The critical substrate strains, ε_c^C and ε_c^A, are the substrate strains at which the maximum stresses reach their respective cohesive ($\sigma^M = \sigma_c$) and adhesive ($\tau^M = \tau_c$) critical stresses. The equations for the maximum stresses (Eqs. 3-10, 3-11) are substituted with the corresponding critical stresses, and rearranged to give:

$$\varepsilon_c^C = \frac{\sigma_c}{E} \cdot \frac{1}{\left(1 - \frac{1}{\cosh(\beta \cdot l)}\right)} \tag{3-12}$$

$$\varepsilon_c^A = \frac{\tau_c}{h \cdot \beta \cdot E} \cdot \frac{1}{\tanh(\beta \cdot l)} \tag{3-13}$$

Fig. 3-10 shows the critical strains as a function of segment length. The substrate strain increases from zero and critical strain with the lowest magnitude will occur first. The plot can be used to determine the preferred fracture mode at a given segment length. The intersection of the curves gives the critical length.

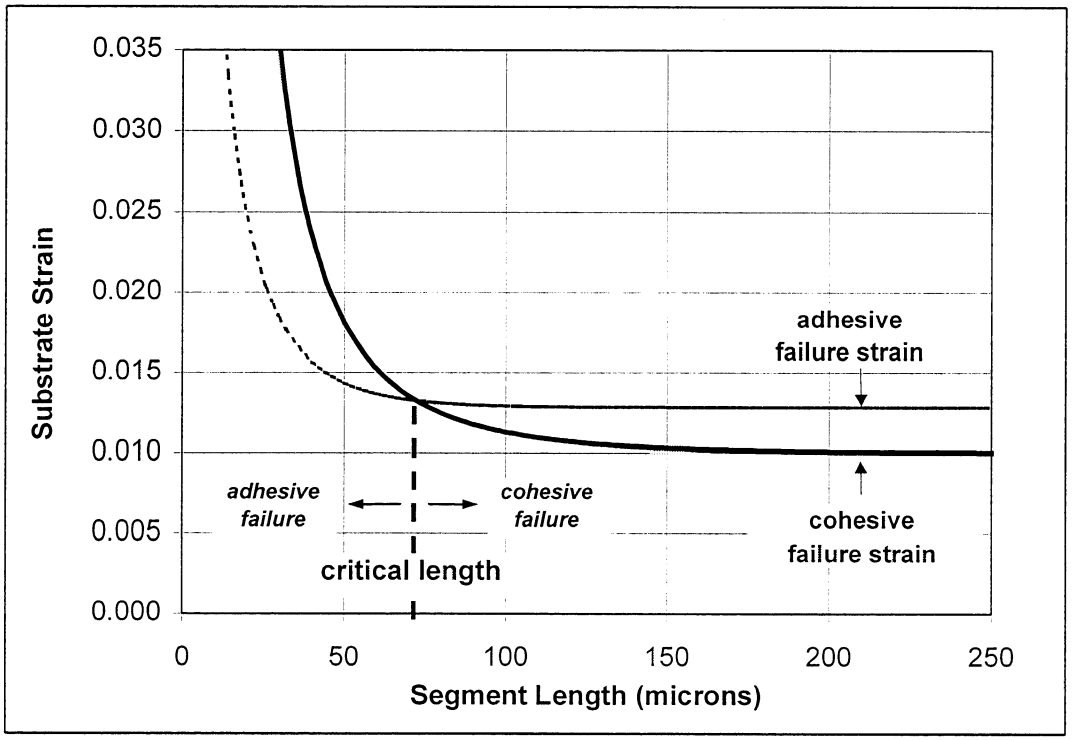

Figure 3-10: Critical substrate strains from Cox model. The composite fractures either cohesively or adhesively when the corresponding critical strain is reached.

3.3.2.2 Example of fracture mechanism

The fracture mechanism described above is shown in Fig. 3-11. This shows how segments become progressively shorter until the critical length is reached. It is assumed that the segment fractures in half when the cohesive critical strain is reached.

The original segment length is 400 microns (Fig. 3-11, point **A**). As the strain increases, the cohesive failure strain is reached (**B**) and the segment fractures in two, from 400 to 200 microns (**B** to **C**). As the substrate strain continues to increase, the segment continues to fracture in two (200→100, **C** to **D**; 100→50, **D** to **E**). At **E**, the adhesive critical strain is lower than the cohesive critical strain, and the segment begins to delaminate. There can be no additional cohesive fracture.

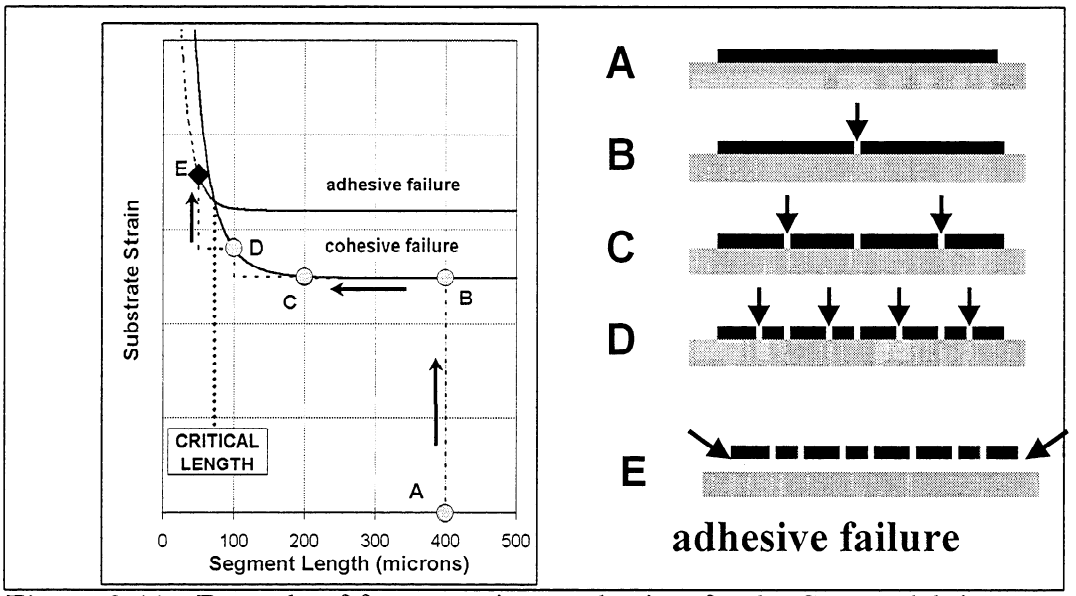

Figure 3-11: Example of fragmentation mechanism for the Cox model, in terms of strain of the substrate. With increasing strain, the line continues to fracture until adhesive fracture preferentially occurs. The limit for adhesive fracture is the critical length.

3.3.2.3 Critical length

The critical length marks the minimum segment length that can fracture before delamination occurs. Above the critical length, the cohesive failure strain is lower and the segment will cohesively fracture into smaller segments. Below the critical length, the adhesive failure strain is lower and the segment will adhesively fail and delaminate. Thus, it is the length at which the cohesive and adhesive failure strains are equal to each other ($\varepsilon_c^C = \varepsilon_c^A$). The equation for the critical length is derived by setting equations for the critical matrix strains equal to each other. Rearrangement for the length gives:

$$l_c = \frac{4}{\beta}\tanh^{-1}\left(h \cdot \beta \cdot \frac{\sigma_c}{\tau_c}\right) \tag{3-14}$$

The critical length increases nonlinearly with effective line thickness, as shown in Fig. 3-12. Above a critical thickness, only detachment will occur. Similar to the Kelly-Tyson model, fragmentation should produce segments lengths between l_c and $2l_c$. Assuming a uniform distribution, the expected length is:

$$\bar{L} = \frac{3}{2}\frac{4}{\beta}\tanh^{-1}\left(h \cdot \beta \cdot \frac{\sigma_c}{\tau_c}\right) \tag{3-15}$$

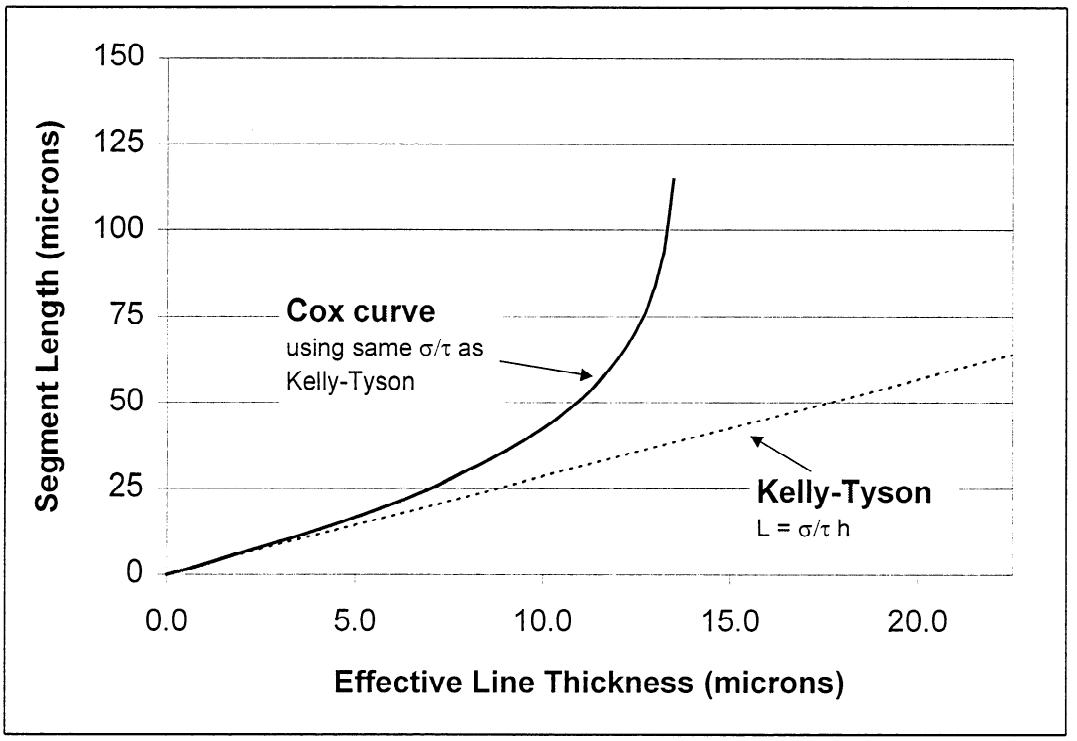

Figure 3-12: The segment length curve for the Cox model shows that the critical length increases nonlinearly with effective line thickness.

3.4 Bond-site Model

The bond-site model was developed in this thesis to take into account the discontinuous bonding between toner and paper. This model is a modification of the Kelly-Tyson model (Sec. 3.2). The Kelly-Tyson model was used as a basis rather than the Cox model because the toner-paper bonds are expected to yield plastically when wet (Sec. 3.4.1.2). The interface consists of discrete bond-sites to more realistically model the physical system. The discrete bond-site feature will be shown to be important for fragmentation in terms of a shift in the expected segment length from changes in the distance between bond-sites.

Discrete bonding has been discussed previously relative to paper. Previous work modeled the contributions by individual fibers on the gross properties of a sheet of fibers. Bond-sites are discussed in terms of the contribution of individual fibers based on the number of bonds per fiber and deformation of fiber segments between bonds (Page and Seth, 1980; Perkins, 1980; Gates and Westcott, 1996). As discussed previously, both the Kelly-Tyson and Cox models have been used for paper, but not in terms of the multiple fracture of a single component. Relative to paper, fracture is considered to occur as either a fiber break or fiber pull-out.

The bond-site will first be defined as a model of the toner-paper bond, in terms of the shear properties and physical dimensions of the toner-paper bond. The mathematical equations to describe stress transfer to the toner line will then be developed. The expected segment length resulting from fragmentation is estimated from a calculated critical bond-site number. The critical value gives the number of bonds necessary to reach the critical stress. The segment length curve from this model will be compared with those from the Kelly-Tyson and Cox models.

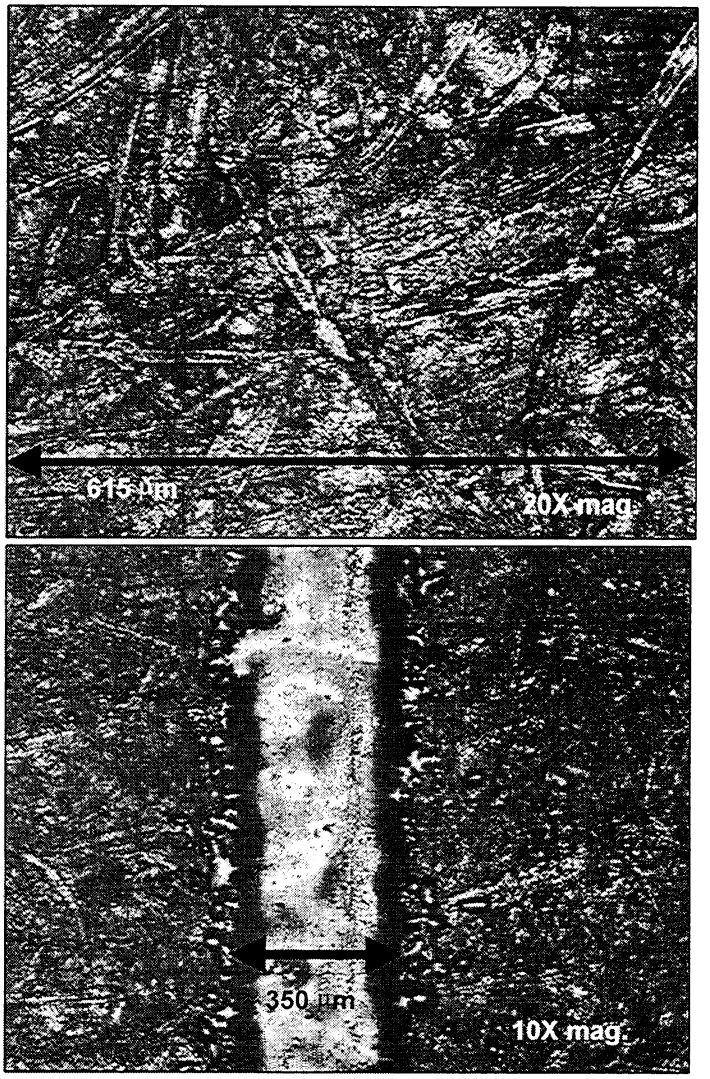

Figure 3-13: Image of paper surface (top, 20X) and toner line on a paper surface (bottom, 10X) as seen through a confocal scanning laser microscope. The paper surface consists of individual fibers.

3.4.1 Physical model

3.4.1.1 Toner on paper

As discussed in Sec. 3.1.1, toner on paper is modeled as the toner line, toner-paper bonds, and the bulk paper. Because of the roughness of the paper surface, the contact between toner and paper is not continuous. On a microscopic scale, the surface of copy paper is not flat and smooth. Rather, the surface of paper is formed by the surfaces of individual fibers (Fig. 3-13). High regions of the paper surface are the upper surface of fibers, while low regions are voids

between fibers. The difference in height between high and low regions is on the order of 10 microns and the distance between high regions is on the order of 100 microns. Even though the toner may conform to the surface during fusing, the paper surface is not continuous, thus the interface is not continuous. The discrete region of contact between the toner and paper is defined as the toner-paper bond.

In the bond-site model, the interfacial region between toner and paper is described with discrete bonding sites (Fig. 3-14). The bond-sites are idealized bonds that represent the shear deformation properties and axial dimensions of the actual toner-paper bonds. The shear deformation will be discussed as a bond strength, where the bond yields plastically. The axial dimensions will be described with bond-spacing and effective bond length, where the bond-spacing is the peak-to-peak distance between bonds and the effective length is the length over which stress is transferred per bond.

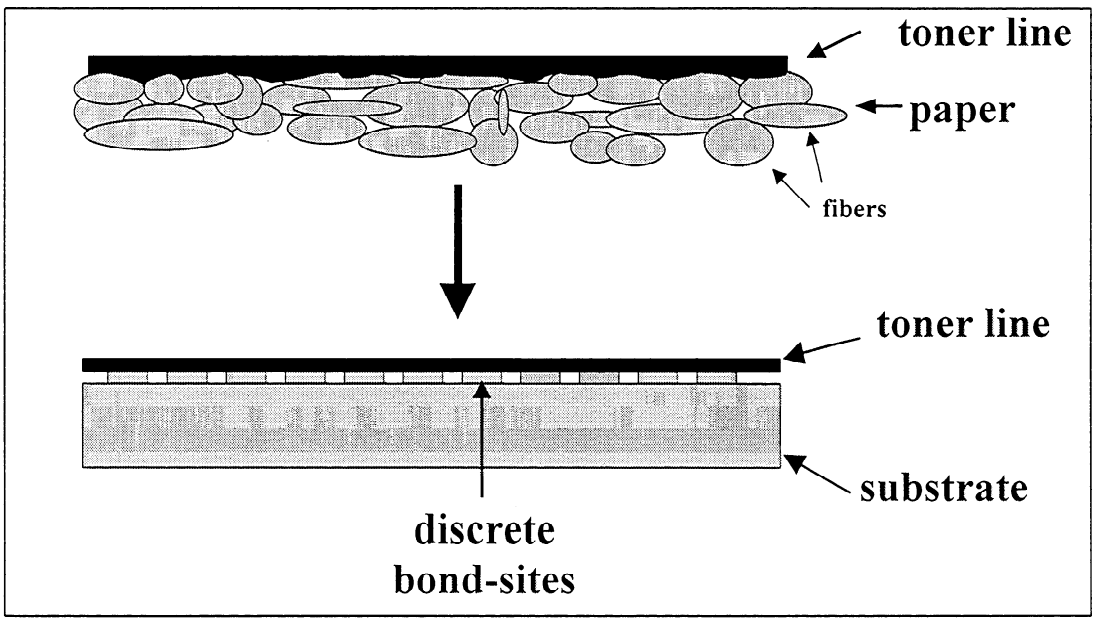

Figure 3-14: The bond-site model represents the interfacial region between toner and paper with discrete bond-sites.

3.4.1.2 Toner-paper bonds

The toner-paper bond includes the toner, the fiber, and the adjacent fiber-fiber interfaces, in addition to the precise toner-paper interface (Fig. 3-15). The bond includes all these components because they are geometrically difficult to separate, and the shear stress between toner and paper is not expected to be a function of the toner-fiber interface alone. A description of total shear deformation of toner-paper bonds must include the fiber and the adjacent fiber-fiber interface because they are expected to deform as much as the toner-fiber interface.

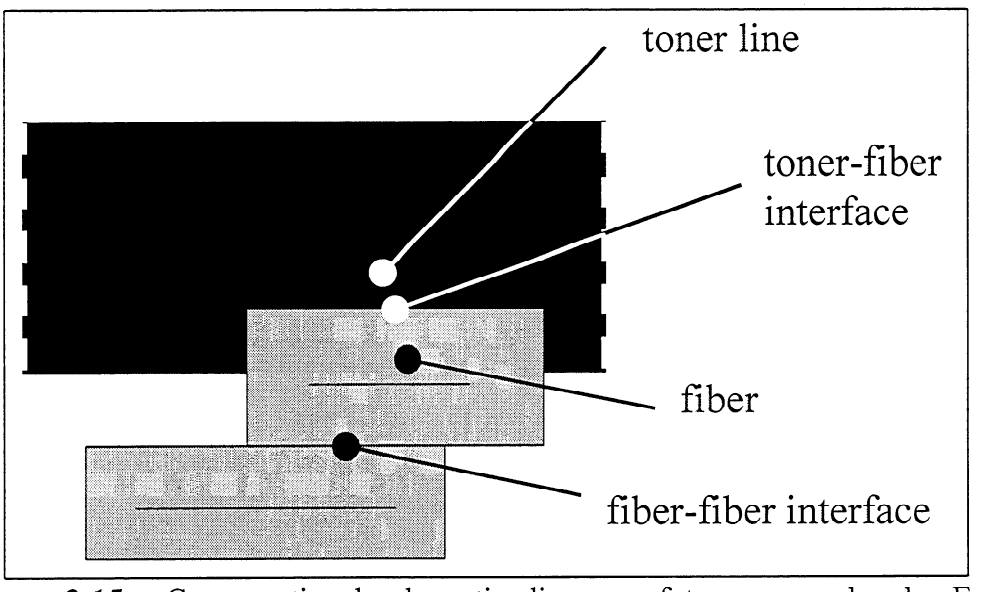

Figure 3-15: Cross-sectional schematic diagram of toner-paper bond. Each toner-paper bond is considered to be a composite consisting of the four regions shown above.

The shear properties will be described by a bond strength, τ_B, which is an empirical composite property of the bond. The geometry and forces within the bond are too complex to allow a simple calculation from the properties of the individual components. The attractive forces may include mechanical interlocking, van der Waals forces, and hydrogen-bonding. These forces will only be considered qualitatively. For example, the presence of moisture can have a strong effect on hydrogen-bonding, thus can have a strong effect on the bond strength.

It is reasonable that the majority of deformation and failure occurs within the fiber or at the adjacent fiber-fiber interfaces. The bond strength is a function of slip or failure at the interfaces or deformation of the toner or fiber. The strength of the toner-fiber interface depends on the adhesion between the two. If there is only physical contact with van der Waals forces, the adhesion will be relatively weak. If there is mechanical interlocking between the two, the adhesion will be relatively much stronger. It is unlikely that the toner-fiber interface will slip or fail if there is significant mechanical interlocking.

The bond is expected to yield in shear, but not adhesively fracture. The yield may occur as a shear deformation of a fiber or slippage at the fiber-fiber bond. Shear yield of either is reasonable, considering the properties of a sheet of paper. Niskanen (1998) described paper as a plastic material and Kubát *et al.* (1963) showed increasing yielding of a sheet of paper with increasing moisture content. Further, the Kelly-Tyson model has been used to model the pull-out of a fiber from paper (Shallhorn and Karnis, 1979; Yan and Kortsschot, 1996).

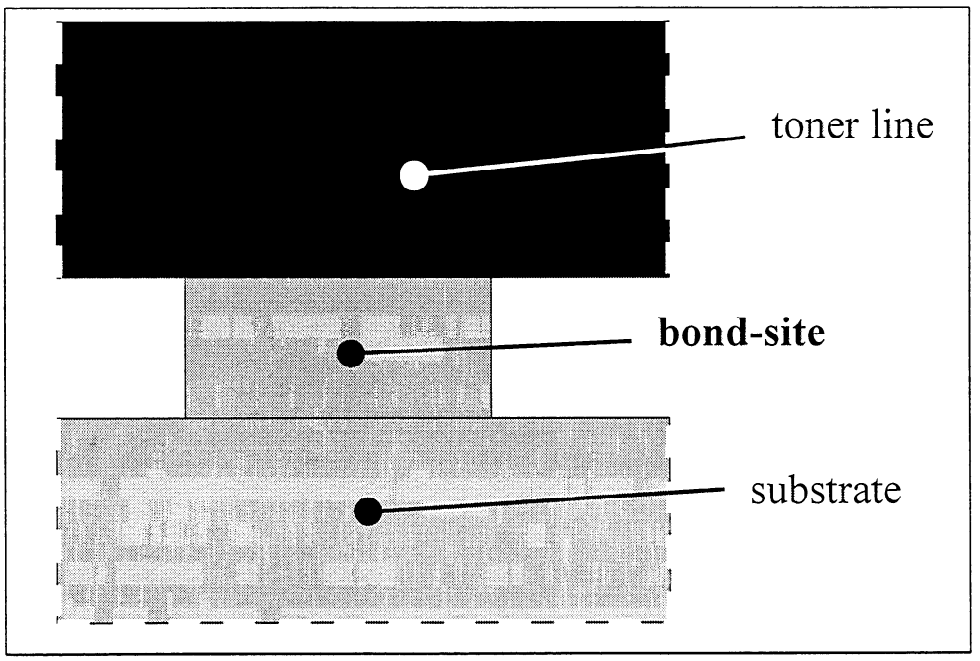

Figure 3-16: The bond-site is a model of the toner-paper bond. It represents the shear properties and axial dimensions of the actual bond.

3.4.1.3 Bond-sites

The toner-paper bond is modeled with the bond-site (Fig. 3-16). From the above discussion, the bond-site must include four important aspects:

- the line is in contact with the paper surface at discrete regions, not continuous
- there is not a clearly defined interface, rather an interphase of finite volume
- properties of the bond are a function of its components
- bond is expected to yield in shear, not fracture

The bond-site has a shear strength equal to the bond strength, τ_B. This is a plastic yield shear stress, same as for the Kelly-Tyson model. The total length of a bond-site, $\bar{l}$, consists of an effective bonded length, $\bar{e}$, and an ineffective length, $\bar{i}$ (Fig. 3-17). The fractional effective bond length is $\dot{e}$. The bond-spacing (peak-to-peak distance between bonds) is equal to the total length of a bond-site.

$$\bar{l} = \bar{e} + \bar{i} \tag{3-16}$$

$$\dot{e} = \frac{\bar{e}}{\bar{l}} \tag{3-17}$$

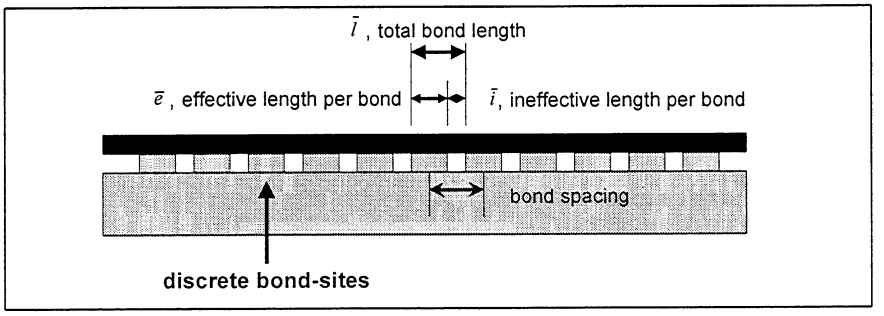

Figure 3-17: Each bond-site is comprised of an effective and ineffective length. The bond-spacing is the peak-to-peak distance between adjacent bond-sites.

These figures show an idealized cross-section of the interfacial region. The bond-sites shown in these figures are meant to be an aid in conceptualizing the toner-paper bonds and to provide a basis for a mathematical model. The idealized bond-sites relate to the actual toner-paper bond by emphasizing the discreteness of the bonds and defining the relative axial dimensions. In reality, the dimensions of the bonds are distributed and the bonds might not

extend across the entire width of the line. For the purpose of this analysis, the dimensions (effective length and bond-spacing) are assumed to be uniform and are described by an average value. By using average values, the fragmentation can be described in terms of single parameters. This allows the important parameters to be identified and the effect of a change of a parameter to be more easily described. These basic results should not change significantly due to the variability of the system.

Also, the thickness of a bond-site (distance between the toner line and the substrate) is not considered in this analysis. The bond-sites are shown in the figures with a relatively significant thickness to distinguish the bond-site as a separate region from both the toner line and the substrate. In reality, there is not a distinct gap between the toner line and the substrate.

3.4.1.4 Fragmentation

Fracture will occur between bond-sites when the paper expands and increases the axial stress above the critical stress of the line (Fig. 3-18). The paper may expand due to hygroexpansion or applied mechanical force. Fracture produces line segments that can be described by a segment number or length. The segment number, N, is the number of bonds per segment. The segment length, L, is given by the segment number multiplied by the bond length.

$$L = N \cdot \bar{l} \tag{3-18}$$

In the following sections, the model will be discussed in terms of number of bonds, rather than lengths. It is more convenient to use discrete numbers rather than lengths. The numbers can be converted to lengths by multiplying by the bond-length, $\bar{l}$.

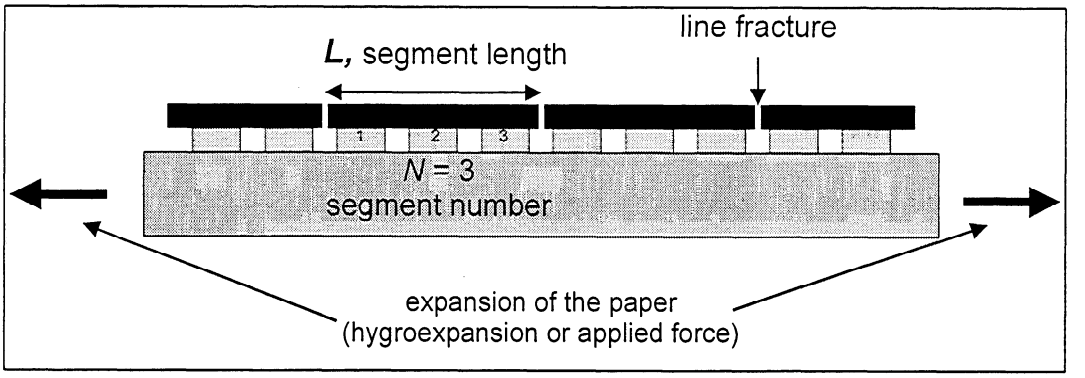

Figure 3-18: The toner line fractures into segments of length, L, when the axial stress due to expansion exceeds the critical stress of the line.

3.4.2 Mathematical model

A basic stress transfer model will give the change in axial stress per bond. This will be used to calculate the number of bonds required to reach the critical stress. The bond strength is assumed to be constant, the same as the Kelly-Tyson model. The distance to reach a given axial stress will be greater because of the noncontinuous interface.

The same differential equation that was presented for the Kelly-Tyson and Cox models is used as the basis (Eq. 3-2). Assuming that the shear stress is constant at the bond strength, τ_B, the axial load increases linearly with length (Eq. 3-19). This assumption is valid if the bond yields plastically (Sec. 3.4.1.2). To give the change in stress over a single bond-site, $\Delta\sigma_B$, the change in length is set equal to the effective bond length, $\bar{e}$ (Eq. 3-20).

$$\Delta\sigma \cdot A = \tau_B \cdot w \cdot \Delta x \tag{3-19}$$

$$\Delta\sigma_B \cdot A = \tau_B \cdot w \cdot \bar{e} \tag{3-20}$$

The axial load, $\sigma_l \cdot A$, at length, l, is the summation of the changes in load over that length (Eq. 3-21), up to the midpoint of the line segment (Fig. 3-19). This can be written in terms of the number of bonds, n, within the length and the effective bond length, $\bar{e}$.

$$\sigma_l \cdot A = \Sigma(\Delta\sigma_B \cdot A) = \Sigma(\tau_B \cdot w \cdot \bar{e}) \tag{3-21}$$

$$\sigma_l \cdot A = \tau_B \cdot w \cdot \sum \bar{e} \tag{3-22}$$

$$\sigma_l \cdot A = \tau_B \cdot w \cdot n \cdot \bar{e} \tag{3-23}$$

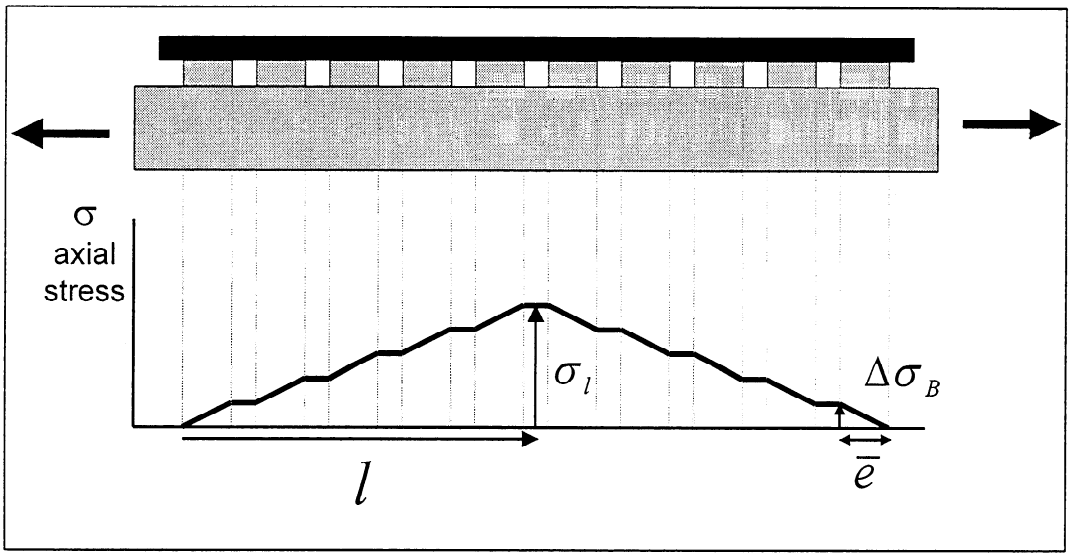

Figure 3-19: The increase in axial stress along the line. The stress increases linearly over a bond-site and remains constant over a gap. The axial stress is maximum at the midpoint of the line.

The number of bonds to reach a given stress, σ_l, is derived by rearranging Eq. 3-23. The length of line, l, equals the number of bonds times the bond length (Eq. 3-25). The line length can then be given in terms of the fractional effective bond length, $\dot{e}$, and the effective thickness, $h = A/w$ (Eq. 3-26).

$$n = \frac{\sigma_l \cdot A}{\tau_B \cdot w} \cdot \frac{1}{\bar{e}} \tag{3-24}$$

$$l = n \cdot \bar{l} = \frac{\sigma_l \cdot A}{\tau_B \cdot w} \cdot \frac{1}{\bar{e}} \cdot \bar{l} \tag{3-25}$$

$$l = \frac{\sigma_l}{\tau_B} \cdot \frac{1}{\dot{e}} \cdot h \tag{3-26}$$

Plotting the length versus the effective line thickness, h, will produce a linear curve with a zero intercept. The Kelly-Tyson model is the ideal case where the interface is continuous, $\dot{e} = 1$. Any discontinuity in the interface (decrease in $\dot{e}$) will increase the length.

3.4.3 Fragmentation mechanism

The model will be used to calculate the segment numbers (lengths) that are expected from fragmentation. A critical bond number is calculated from Eq. 3-24, from which a distribution of segment numbers is determined. The segment numbers can be converted to lengths by multiplying by the bond-spacing. An important feature from the mechanisms is that the calculated number is rounded up to the next whole number.

3.4.3.1 Critical bond-site number

The critical bond-site number, n_c, is the number of bonds necessary to reach the critical stress. The line fractures when the axial stress exceeds the critical stress of the line (Eq. 3-27 and Fig. 3-20). The critical length (Eq. 3-30) is the minimum line length for the axial stress to reach the critical stress.

$$\sigma \geq \sigma_c \tag{3-27}$$

$$\sigma = \frac{\tau_B}{h} \cdot n \cdot \bar{e} \geq \sigma_c \tag{3-28}$$

$$n_c = \frac{\sigma_c}{\tau_B \cdot \bar{e}} \cdot h \tag{3-29}$$

$$l_c = \frac{\sigma_c}{\tau_B \cdot \dot{e}} \cdot h \tag{3-30}$$

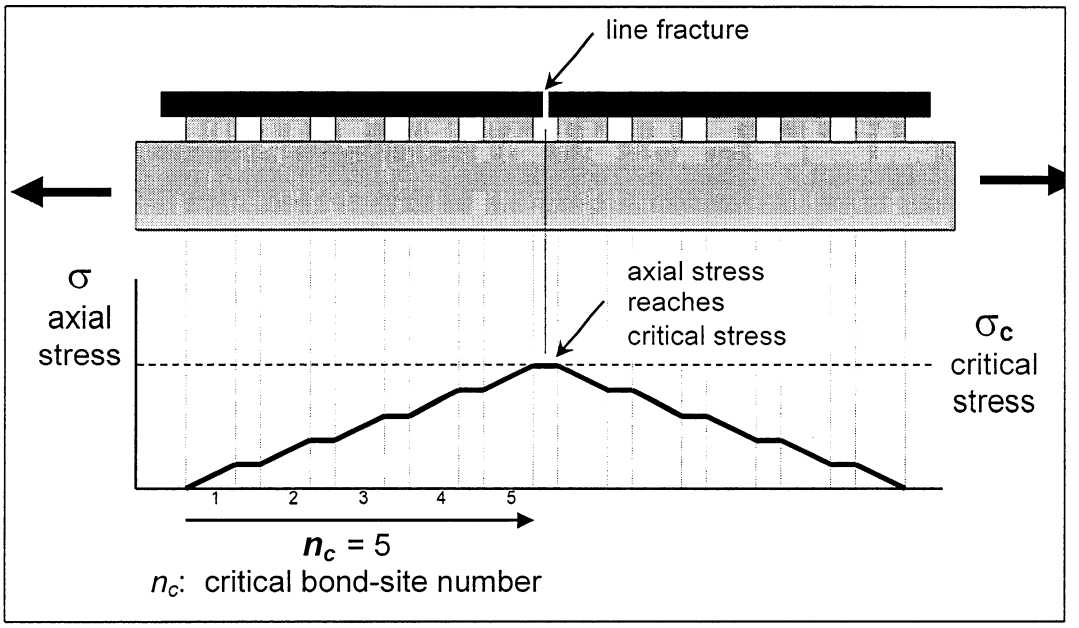

Figure 3-20: The toner line fractures when the axial stress reaches the critical stress of the line. The critical bond-site number gives the number of bond-sites necessary for the axial stress to reach the critical stress.

The expected critical bond-site number, $\bar{n}_c$, is the calculated critical number (Eq. 3-29) rounded up to the next whole number (1, 2, 3, . . .). Fracture of the line is not expected to occur within a fraction of a bond-site (Fig. 3-21). The line fractures at the point of maximum stress, which is at the midpoint of the segment and at the gaps between bond-sites. Within a bond-site, the axial stress is increasing, and has not reached the maximum stress. This is important because it results in a shift of the segment length curve (Sec. 3.4.4).

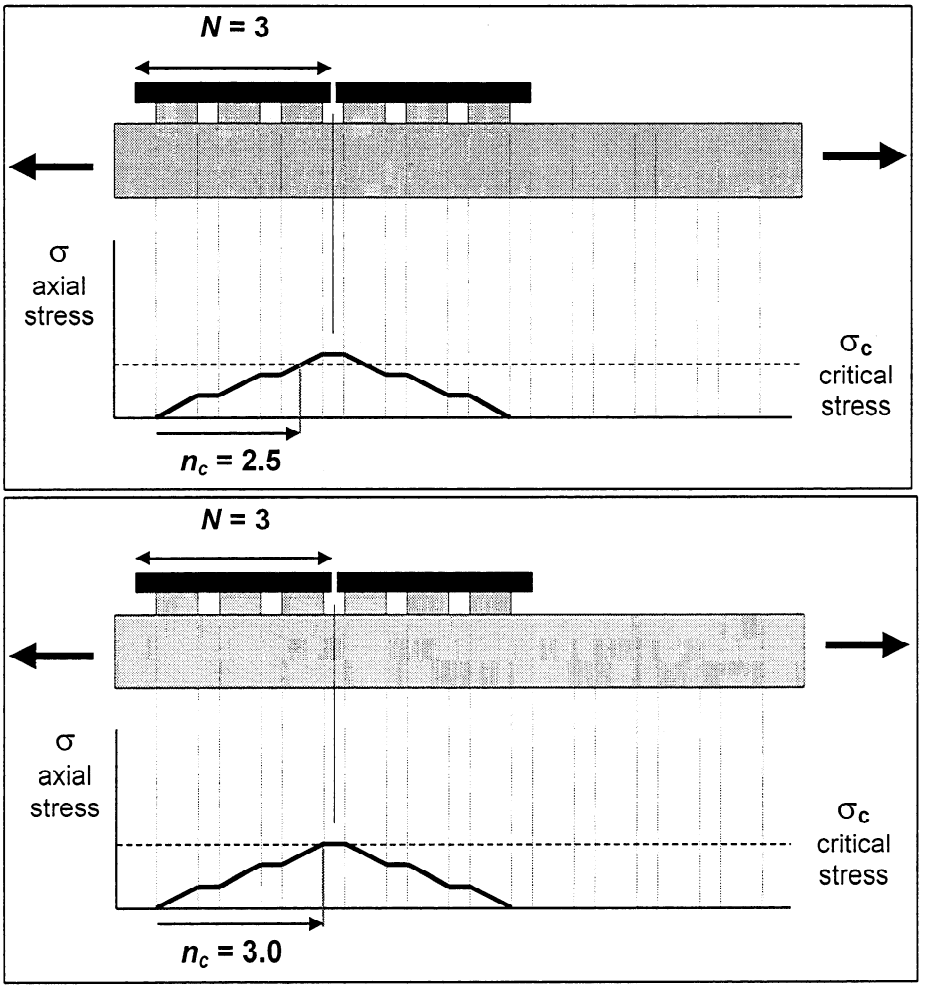

Figure 3-21: The segment number is the next whole number greater than the calculated critical number. The line fractures at the point of maximum stress, which is at the gap between bond-sites.

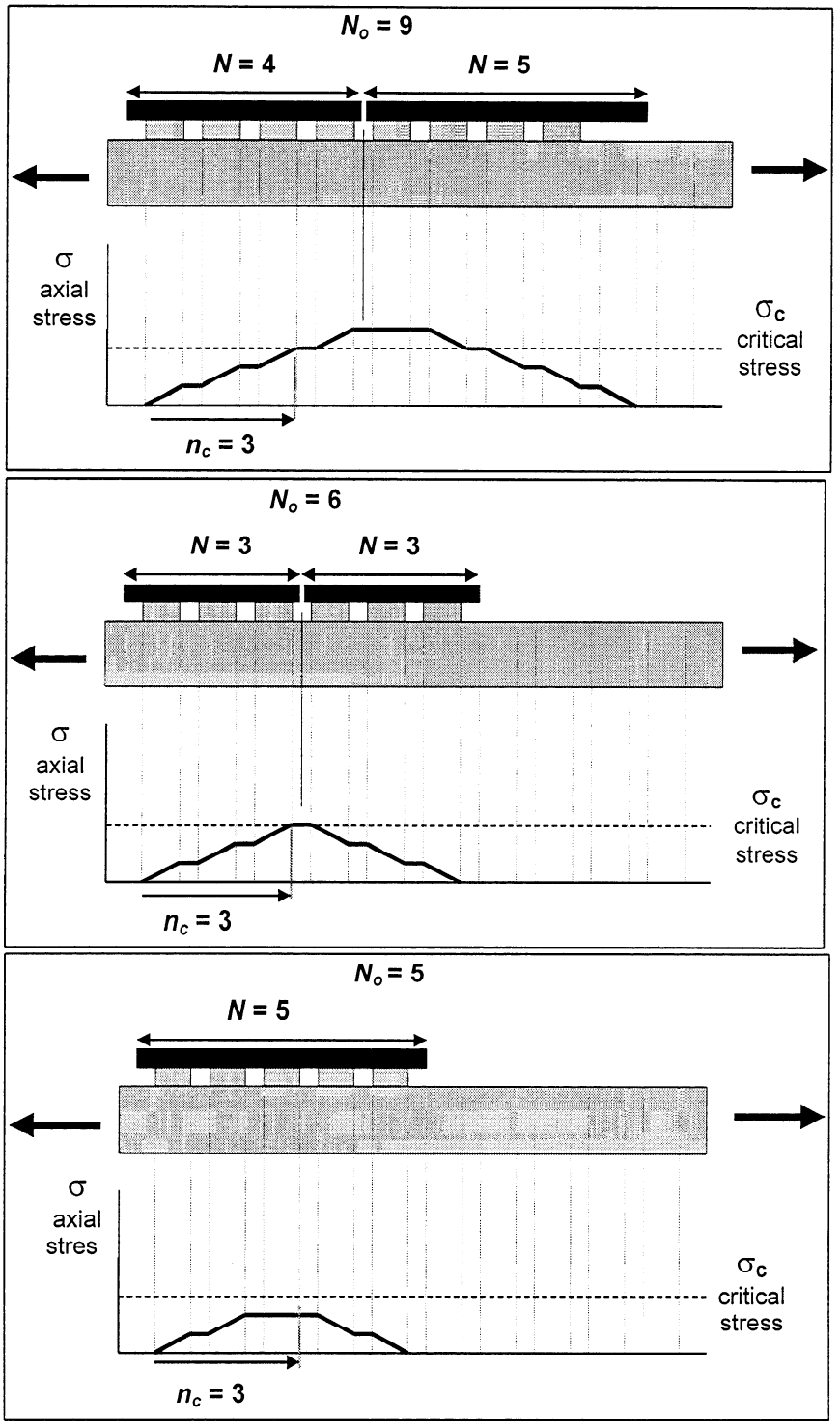

Figure 3-22: A distribution of segment lengths will be produced upon fragmentation. A line with a critical number $\overline{n}_c = 3$ will fracture into segments with numbers between $\overline{n}_c$ ($N = 3$) and $2\overline{n}_c - 1$ ($N = 5$).

3.4.3.2 Segment number resulting from fragmentation

The segment number, N, is expected to be between n_c and $(2n_c - 1)$. A segment will fracture only if its midpoint is at least $\bar{n}_c$ bonds from the ends. Below $\bar{n}_c$, there are not a sufficient number of bonds for the stress to reach the critical level. Fig. 3-22 shows an example of fragmentation for a critical number, $\bar{n}_c = 3$. A segment with an original bond number greater than or equal to $2\bar{n}_c$ ($N_o \geq 6$) will fracture because there is sufficient length for the stress to reach the critical level (Fig. 3-22 *top*, *middle*). A segment with fewer bonds than $2\bar{n}_c$ ($N_o < 6$) will not fracture, because there is insufficient distance for the stress to increase (Fig. 3-22 *bottom*). Therefore, the minimum segment number is $\bar{n}_c$ (1/2 of $2\bar{n}_c$) and the maximum is $(2\bar{n}_c - 1)$.

$$\bar{n}_c \leq N \leq (2\bar{n}_c - 1) \tag{3-31}$$

$$\bar{n}_c \cdot \bar{l} \leq L \leq (2\bar{n}_c - 1) \cdot \bar{l} \tag{3-32}$$

3.4.3.3 Segment number distribution

The distribution of the segment number will be discussed to provide an expected segment number, $\overline{N}$, based on the critical number. Discrete statistical distributions are used to describe this distribution. Uniform and triangular distributions will be discussed because they are the simplest discrete distributions that are bounded on both ends. The probability function, $p(N_i)$, gives the probability that a segment has i number of bonds. For example, $p(N_3) = 1/3$ means that 1/3 of the segments are of number 3.

3.4.3.3.1 Uniform distribution

The uniform distribution has equal probabilities at each segment number between $\overline{n}_c$ and $2\overline{n}_c - 1$. The probability is inversely proportional to the number of bond-sites within the range (Walpole and Myers, 1989). The mean of the segment number, $\overline{N}$, is centrally located.

$$p(N_i) = \frac{1}{\overline{n}_c}, \quad \overline{n}_c \le N_i \le 2\overline{n}_c - 1 \tag{3-33}$$

$$\overline{N} = \frac{3\overline{n}_c - 1}{2} \tag{3-34}$$

Fig. 3-23 shows the probabilities for each segment number for critical numbers from 1 to 4. The equation for $\overline{n}_c$ (Eq. 3-29) can be substituted into Eq. 3-34 to give the mean segment length in terms of the bond-site parameters. The use of this equation will be discussed further in the following section.

$$\overline{N} = \frac{3}{2}\frac{\sigma_c}{\tau \cdot \overline{e}} \cdot h - \frac{1}{2} \tag{3-35}$$

3.4.3.3.2 Triangular distribution

The triangular distribution is skewed to the critical bond number (Fig. 3-24). This distribution is reasonable if segments are more likely to be near the critical number. The highest probability is at $\overline{n}_c$, which decreases uniformly to zero at $\overline{n}_c$.

$$p(N_i) = \frac{2\overline{n}_c - N_i}{\frac{1}{2}\overline{n}_c(\overline{n}_c + 1)}, \quad \overline{n}_c \le N_i \le 2\overline{n}_c - 1 \tag{3-36}$$

$$\overline{N} = \frac{4\overline{n}_c - 1}{3} \tag{3-37}$$

$$\overline{N} = \frac{4}{3}\frac{\sigma_c}{\tau \cdot \overline{e}} \cdot h - \frac{1}{3} \tag{3-38}$$

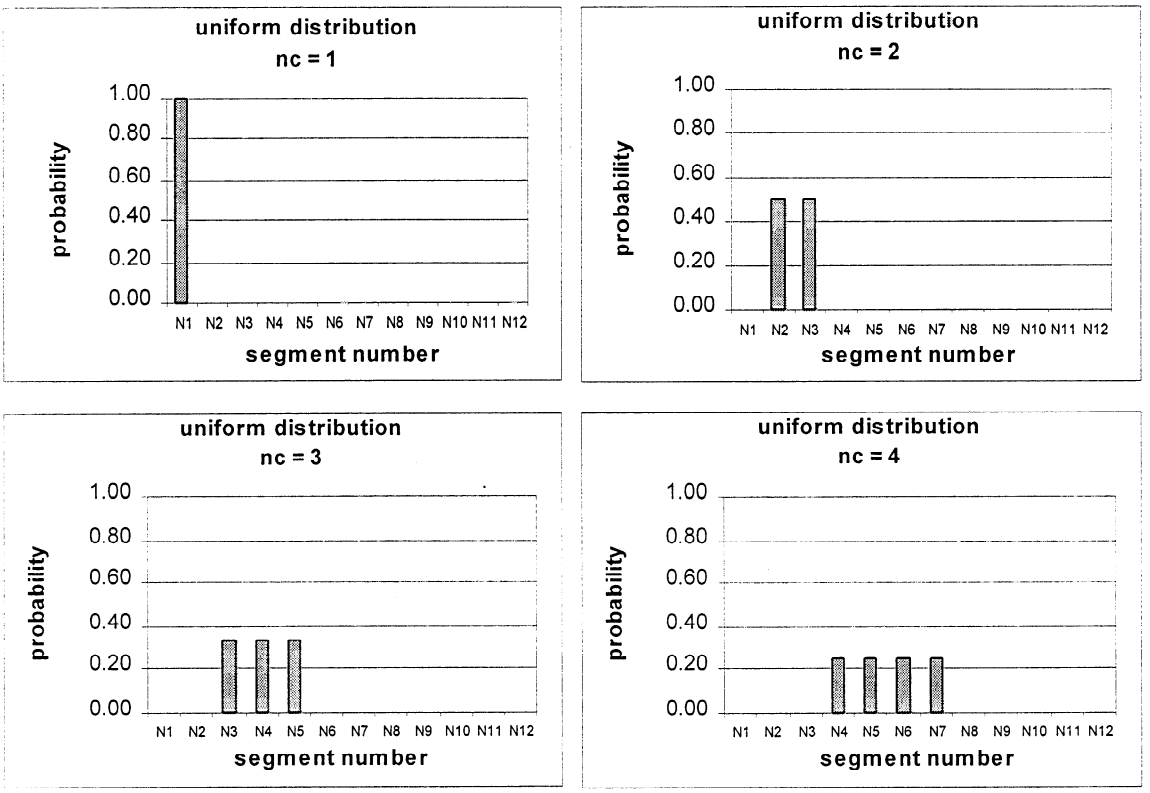

Figure 3-23: Segment number distribution assuming a discrete uniform distribution.

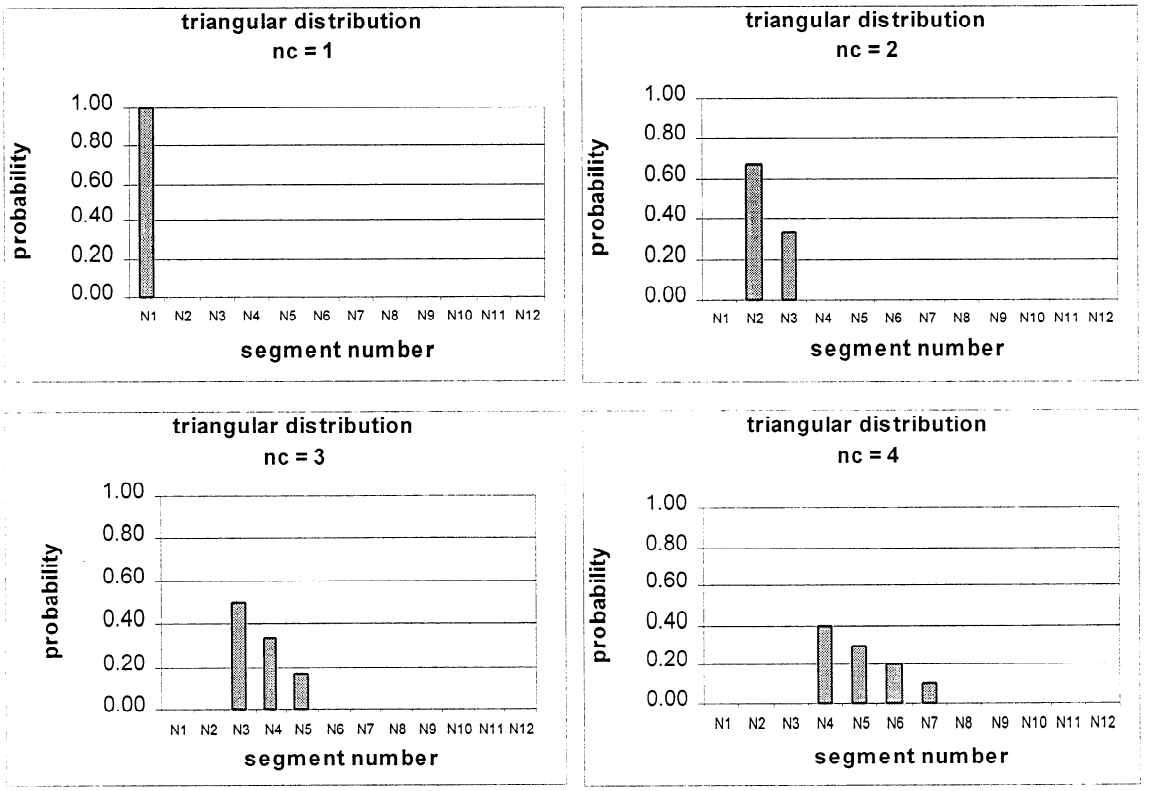

Figure 3-24: Segment number distribution assuming a discrete triangular distribution.

3.4.4 Bond-site curve

The segment-length curves are used to present the model and analyze experimental results. The critical bond-number is plotted vs. effective thickness ($h = A/w$) as shown in Fig. 3-25. The curve for the critical numbers has step changes because the critical numbers must be whole. The critical number curve is the whole number rounded up from the noncontinuous curve. Fig. 3-26 shows the expected segment number based on the critical curve. The segment number is expected to be between the critical number, n_c, and the upper limit ($2n_c - 1$). Assuming a uniform distribution, the expected value is at $\frac{1}{2}(3n_c - 1)$ as shown in this figure. This curve with the expected segment number is referred to as the bond-site curve.

Fig. 3-27 shows the bond-site curve in terms of length. The segment lengths are determined as the segment number multiplied by the bond-spacing, $L = N \cdot \bar{l}$. The segment length curve is expected to be a linear fit of the calculated lengths. Eq. 3-39 gives the linear fit for the uniform distribution.

$$\bar{L} = \frac{3}{2} \cdot \frac{\sigma_c}{\tau_B \cdot \dot{e}} \cdot h + \frac{1}{4} \cdot \bar{l} \tag{3-39}$$

The factors, 3/2 and 1/4, depend on the actual distribution of the fragmentation. The uniform distribution was used here for descriptive purposes. It is more appropriate to show the equation for the expected length in terms of general factors:

$$\bar{L} = f_1 \cdot \frac{\sigma_c}{\tau_B \cdot \dot{e}} \cdot h + f_2 \cdot \bar{l} \tag{3-40}$$

This analysis shows that it is reasonable for experimental data to have a non-zero intercept. In addition, the model predicts a shift in curves that is not expected from either the Kelly-Tyson or Cox models. Even with the same slope (same σ and τ), the curve can shift vertically due to a difference in bond-spacing, $\bar{l}$.

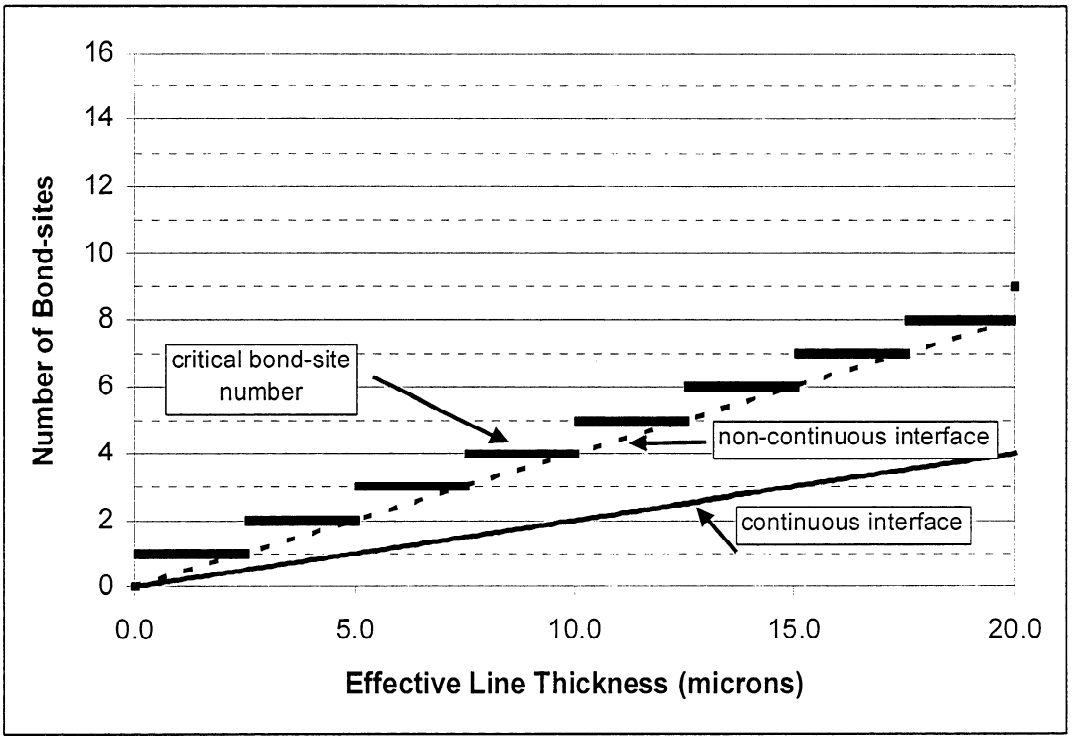

Figure 3-25: The critical bond-site number increases as steps with increasing effective line thickness.

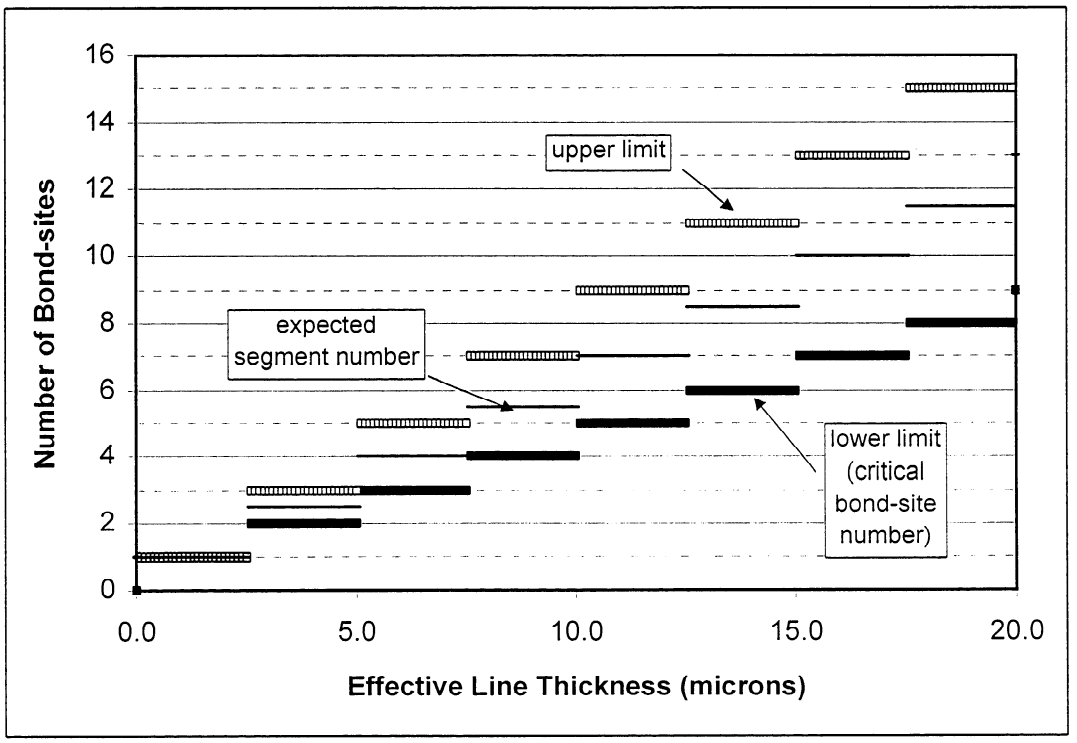

Figure 3-26: The expected segment number is at the midpoint of the limits, assuming a uniform distribution. The limits are given by $\overline{n}_c$ and $2\overline{n}_c - 1$.

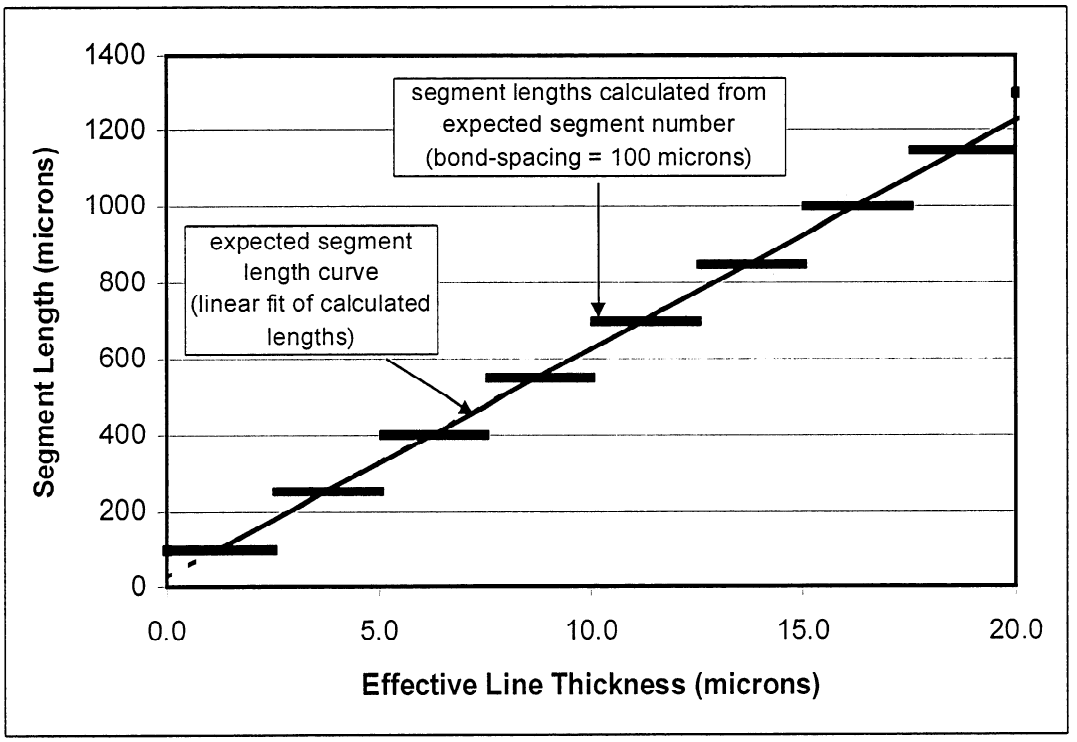

Figure 3-27: The expected segment length curve of the bond-site model for segment lengths greater than 1 bond-length (assuming uniform distribution). The linear regression yields a non-zero intercept.

It should be noted that the intercept does not have a physical meaning. The intercept is a result of the linear fit of the expected data greater than one bond-length. It is not expected that the segment lengths reach a fraction of the bond-spacing as the thickness approaches zero. Rather, at the lowest thicknesses, the segment length should equal the bond-spacing.

3.4.5 Limits of the model

The model is limited to describing relative changes in the segment length. The segment length can be estimated only as a change from a previous value based on relative changes of the parameters. This is because there is not a clear relationship between the critical length and expected length. Further, independent values of the parameters are not available for calculation of an absolute value. The model also lacks the precision to allow accurate curve fitting to extract absolute values of the parameters from experimental curves.

The model is applicable for describing the fragmentation of lines that fracture at low elongation (relative to the extension of the substrate) and lines that require more than one bond-site to fracture. The line must fracture at a strain that is less than the strain of the substrate (Sec. 3.1.2.3). Otherwise, two lines that have the same strength but different fracture strains could not be directly compared. The analysis may indicate that the fragmentation should be the same, however, the fragmentation may actually be significantly different due to a strain dependence.

The lower limit to the model is given where the expected segment length is less than the length of one bond-site ($n_c < 1$). If the expected segment length is less than one bond-site, then the segment length curve should be horizontal, equal to the bond-spacing. The model would not show the sensitivity to parameters because the segment length would remain constant over a large thickness range. Alternatively, it is feasible that a line could fracture multiple times within a bond, which would represent a shift in mechanism. The upper limit is given where the largest expected segments approach the original line length. The upper end of the segment length distribution would then be bounded.

3.4.6 Summary – bond-site model

The bond-site model was developed in this thesis to describe the fragmentation of toner on paper upon immersion in water. The model addresses the discontinuity of the bonding between toner and paper with discrete bond-sites. The bond-site describes the mechanical deformation with a bond strength and the dimensions of the bond-site with an effective length and bond-spacing. The bond-spacing is important because a change in this value can shift the segment length curve. This model overcomes shortcomings described for the fragmentation tests by predicting relative changes of the segment length based on relative changes of the parameters, rather than extracting absolute values of the parameters.

4 EXPERIMENTAL METHODS AND MATERIALS

In this section, the experimental methods and materials will be described. The major experimental techniques that were developed were the preparation of flat, dimensionally-stable cellulose acetate films, preparation of toner films for tensile tests, measurement of the hygroexpansion of paper and cellulose acetate, preparation of toner lines on paper and cellulose acetate for fragmentation tests, measurement of the thickness of the toner lines, and the fragmentation tests. Special note should be made of the toner line preparation technique (Sec. 4.3) and the immersion of the toner line sample in water for the fragmentation tests (Sec. 4.5.1). The toner lines must be aligned with the cross-direction of the paper because the orientation will affect the fragmentation. The toner line samples should be immersed in water no earlier than 48 hours after preparation to allow the samples to equilibrate. An additional experimental technique that was developed in this thesis was the bending beam test, which is described in Appendix I.

4.1 Materials

4.1.1 Cellulose acetate films

Cellulose acetate films were cast from an acetone solution. The technique described here produced flat, uniform films that remain flat when immersed in water (no residual mechanical stresses). The essential steps to this technique are to release the film from the casting surface and turning it over as soon as the film has somewhat solidified, while keeping the film in the acetone-rich atmosphere. The film is then dried completely of acetone while clamped between rings. With this technique, no additional treatments are necessary for mechanical relaxation.

Releasing the film from the casting surface and turning it over minimizes two-sidedness of the film. This step allows the acetone to evaporate from both surfaces of the film and the film to shrink more freely on both surfaces. However, the acetone cannot be completely removed

from the film while the film is unconstrained because buckling will occur. Buckling is minimized by clamping the film between metal rings in the final stages of drying.

4.1.1.1 Materials

Cellulose acetate and acetone are commercially available materials (cellulose acetate: Aldrich, 39.8% acetyl content, ca. 30,000 avg. M_n (GPC); acetone: EM Science, HPLC grade). These materials were used without further purification.

4.1.1.2 Solution preparation

Solutions of cellulose acetate in acetone (10 wt.-%) were prepared. Acetone was added to cellulose acetate powder in a flask. The solution was stirred (magnetic stirrer and stir bar) until the cellulose acetate was completely dissolved (approximately 16 hours). The solution was pressure filtered (3 micron teflon filter), then de-aerated using an ultrasonic bath.

4.1.1.3 Apparatus

The casting surface is a teflon overlay (vinyl supported, Bytac Type VF-81, Norton Performance Plastics Corp., Akron, OH) adhered to a mirror. The surface is teflon so that the cellulose acetate film releases easily. The mirror provides a uniform, flat support. The mirror rests on a leveled aluminum plate.

The casting is done inside a glove bag to control the evaporation of acetone from the solution. The film can be released, turned over, and placed in the ring while remaining in the acetone-rich atmosphere. The bag is purged with acetone-rich nitrogen (10 min) prior to casting to provide a consistent starting atmosphere for casting of the films and to reduce the evaporation rate of the acetone. Acetone-rich nitrogen is obtained by bubbling nitrogen through acetone in a gas-washing bottle. The gas-washing bottle was in a 2 L container of water to minimize the temperature drop of the acetone due to evaporation. Reducing the evaporation rate minimizes

the two-sidedness of the film and the formation of convection cell patterns in the film (due to concentration and temperature gradients) (Sakurai *et al.*, 1993).

Drying rings for standard TAPPI handsheets (Standard TAPPI T 205 om-88) are used (35 mm high x 165 mm o.d. rings, 20 x 19 mm holes around the circumference). The holes in the rings allow for even removal of acetone from both sides of the cellulose acetate film.

4.1.1.4 Casting technique

The solution was volumetrically measured (85 mL) into a glass jar. The jar was placed in the glove bag and the glove bag sealed. The solution was poured onto the casting surface. Eight hours after casting, the film was released from the casting surface and turned over. Eight hours after turning over, the film was placed between the drying rings. Eight hours after placed in the rings, the film was removed from the glove bag and placed in an oven (100°C), while still clamped between the rings. After two hours in the oven, the film is cut into strips. The film is scored and broken into strips (similar to cutting glass), rather than cutting it completely with a knife, because the material is quite brittle. The strips were then stored in a desiccator.

4.1.2 Paper

The paper used for this research was Union Camp Yorktown multipurpose paper (Union Camp, Wayne, NJ). A block of 30 adjacent sheets was selected from a single ream of paper. The paper was stored at 50% relative humidity and 23°C. Gloves were worn at all times while handling the paper.

4.1.3 Toner

Toner was used for tensile tests and toner line samples for fragmentation tests. The composition of the toners is shown in Table 4-1. The Hewlett Packard LaserJet 4 Plus toner was from a cartridge for the LaserJet printer (Hewlett Packard Co., Palo Alto, CA). The toner was transferred from the cartridge to a glass jar. The Xerox 3700 toner was in bottles directly

obtained from Xerox (Xerox Corp., Stamford, CT). Both toners were obtained as a finely divided powder. The toner was stored at ambient conditions.

Table 4-1: Composition of Toners

	Hewlett Packard LaserJet 4 Plus (HP)	**Xerox 3700 (X37)**
composition	40 to 50% styrene acrylate resin	85 to 90% bisphenol A propylene oxide fumarate polymer
	45 to 55% magnetite	10 to 15% carbon black
	1 to 5% asine dye	<5% polyolefin
	1 to 5% polypropylene	<1% amorphous silica
	1 to 2% silica	<1% zinc stearate
glass transition temperature	≈55°C	54.8°C

4.2 Material Properties

4.2.1 Tensile strength measurements

4.2.1.1 Sample preparation

Film specimens of toner were prepared from powder for tensile tests. Specimens were shaped into a "dog-bone" shape using the ASTM method for the tensile properties of plastics (Standard ASTM D 638 – 97) as a guide. The technique involved:

- fusing toner powder on a plate
- pressing the fused toner into a flat film
- cutting the film into strips
- sanding the strips into a dog-bone shape.

The toner powder first was fused on a plate to minimize voids that are initially present between the particles in the powder. The plates were aluminum [150 mm (6 in.) x 175 mm (7 in.) x 12.5 mm (0.50 in.), tooling plate] covered with a teflon overlay (aluminum-foil supported, Bytac Type AF-21, Norton Performance Plastics Corp., Akron, OH). Approximately 17 g of the toner powder was spread on the plate. The plate with the toner was placed in a vacuum oven at 50°C and vacuum was applied (≈100 kPa). After one hour, the temperature was increased to

120°C for the HP toner and 75°C for the X37 toner, while still under vacuum. After two additional hours, the vacuum was released and the temperature was increased to 185°C for the HP toner and 120°C for the X37 toner. The vacuum can be applied only while the toner is below its melting temperature, since above the melt temperature, the toner flows and bubbles may be created in the molten toner. The Xerox toner has a lower melt temperature than the HP toner.

The fused toner was pressed in a heated hydraulic press (Carver laboratory press, model C, Fred S. Carver, Inc, Menominee, WI). The pressing produced a film of uniform thickness with minimal defects on the film surface. The toner was pressed between two aluminum plates (same as above). Thickness gages [1.02 mm (0.040 in.) x 13 mm (0.50 in.) x 200 mm (8 in.)] were used to control the spacing between plates while pressing. Mold release spray was applied to the overlay surfaces to minimize the sticking of the toner to the overlay. The toner was first lightly pressed at a higher temperature than for the final pressing to align the plates on the toner (HP: 120°C, X37: 95°C). The final pressing was done at lower temperatures (HP: 95°C, X37: 70°C), because the material is stiffer at the lower temperature, creating more pressure in the film and compressing any voids. The press load was increased to approximately 22 kN (5000 lb). The load was increased incrementally, approximately 2 kN (500 lb) per minute. The load was maintained at 22 kN (5000 lb) until the thickness gages were in full contact with both plates. The heaters were then turned off and the plates were removed once the temperature was less than 60°C.

The toner film was then cut into 19 mm (0.75 in.) strips. Two methods were used to cut the films, one using a die and the other using a razor blade. The die method was used for the HP LaserJet 4 Plus toner, and the razor blade method was used for the Xerox 3700 toner. The die method could not be used for the Xerox 3700 toner. After pressing (see below), the metal blades

could not be removed from the X37 film without fracturing the film. The Xerox toner adhered too strongly to the blades.

The die method consisted of pressing heated metal blades against the film to score the film. The film could then be broken into strips along the scores. The metal blades were steel rule die stock [0.72 mm (0.0285 in.) x 23.8 mm (0.937 in.) x 152 mm (6.0 in.), beveled edge] (Kentex Industries, Inc., Decatur, GA). The die consisted of metal blades spaced by 19 mm (0.75 in.) using wood blocks [19 mm (0.75 in.) x 38 mm (1.50 in.) x 146 mm (5.75 in.)] held together with bolts. The die was heated in an oven at 185°C for 30 minutes, then placed on top of the toner film. Two aluminum plates were placed on top of the die. The film was deeply scored by the blades at the uniform widths. After at least one hour, the die was carefully removed from the film. The film was broken along the scores by bending the film. The film was supported between wood blocks during bending to prevent the remainder of the film from fracturing.

The razor blade method (for the Xerox 3700 toner) involved heating the film to 75°C, then cutting it with a razor blade. The film was supported on a plate inside of an oven at 75°C and cut while still inside of the oven. The width of the strips was not necessarily uniform after cutting, however the uniformity of cuts was not as necessary because the strips were next sanded to uniform width.

The strips were sanded to produce "dog-bone" specimens (Standard ASTM D 638 – 97) (Fig. 4-1). These specimens have narrow sections in the middle, away from the wider clamp sections, to assure that the sample would break in the narrow section, away from the clamps. The samples were shorter than suggested by the standard because the samples were limited in length from the preparation technique. The strips were sanded to the dog-bone shape using 220

grit sandpaper. The strip was sanded very slowly to prevent fracture of the specimen. A template was used to guide the sanding.

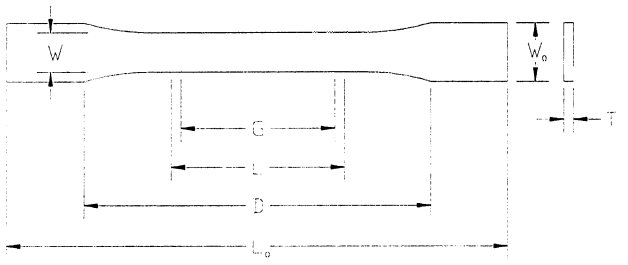

ASTM Dimensions		
T:	specimen thickness	7 mm or under (0.28 in.)
W:	width of narrow section	13 mm (0.5 in.)
L:	length of narrow section	57 mm (2.25 in.)
W_o:	width overall, min.	19 mm (0.75 in.)
L_o:	length overall, min.	165 mm (6.5 in.)
G:	gage length	50 mm (2.0 in.)
D:	distance between grips	115 mm (4.5 in.)
R:	radius of fillet	76 mm (3.0 in.)

Toner Specimens	
** denotes difference from ASTM*	
T:	0.7 to 0.9 mm (0.03 to 0.04 in.)
W:	13 mm (0.5 in.)
L:	25 mm (1.0 in.)*
W_o:	19 mm (0.75 in.)
L_o:	125 mm (5.0 in.)*

Figure 4-1: Dimensions of the "dog-bone" tensile test specimens.

4.2.1.2 Apparatus

Constant displacement tensile tests were done with an Instron Model 1122 Material Testing Instrument (Instron Corp., Canton, MA). Clamping the specimens in the grips was the most important detail, to make sure that the specimen did not fracture within the grips.

A small [25 mm (1 in.) x 38 mm (1.5 in.) surface] plate grip was used in the upper position and a larger [25 mm (1 in.) x 50 mm (2 in.) surface] plate grip was used in the lower position. The small grip was used because it was less awkward to handle, minimizing the likelihood that the specimen would fracture while handling. The large grip was used in the lower position because it gave a more uniform clamping pressure than the second small plate grip. For both styles of grips, one plate was fixed, while the other was adjusted for clamping the sample with a bolt. Liners [rubber sheeting, 1.52 mm (0.060 in.) x 25 mm (1 in.) x 38 mm (1.5 in.)] were used in the grips for the strength measurements to minimize the fracture of the specimens in the grips. The liners maximize the stress distribution, avoiding stress concentrations that may lead to premature fracture.

4.2.1.3 Technique

The specimen was first mounted in the upper grip on the countertop. The specimen was positioned in the grip so that the long axis of the specimen was aligned with the long axis of the grip. The specimen was centered in the plate and perpendicular to the edge of the plate. The rubber liners were positioned between the specimen and plates. The grip was tightened firmly to minimize the slippage, but not excessively to avoid crushing. The upper grip (with the specimen) was then positioned in the upper connector in the Instron. The spacing between the clamps was manually adjusted to get the appropriate gage length. The distance between the closest edges of the plates was measured using a ruler. The lower grips were then tightened firmly. The load was balanced and the gage length reset. Testing commenced until the specimen fractured. The gage length was 75 mm (3.0 in) and the cross-head speed was 2.54 mm/min (0.1 in./min).

4.2.1.4 Analysis

The fracture of the samples was brittle. The strength was calculated as the maximum load divided by cross-sectional area in narrow section. It should be noted that this technique did not give an accurate modulus because of slippage in the grips due to the rubber liners. Tensile tests without the rubber liners gave linear stress-strain curves, however, the modulus varied depending on the gage length (≈1500 MPa for a 25 mm gage length and ≈3000 MPa for a 50 mm gage length) and the fracture was premature due to stress concentrations in the grips. The fracture strain was estimated to be between 0.2 to 1.0%.

4.2.2 Hygroexpansion measurements

The hygroexpansion of cellulose acetate and paper were measured to determine the total expansion of each material upon immersion in water and the approximate rate at which the material expands. The technique involves clamping a strip on one end and measuring the

position of the other end to obtain the length of the film. The hygroexpansion is determined from the difference in length between wet and dry samples.

4.2.2.1 Sample preparation

The samples for the hygroexpansion measurements were 12.5 mm (0.5 in.) wide by approximately 100 mm (4 in.) long. The samples were stored in a desiccator for a minimum of 48 hours prior to testing.

4.2.2.2 Apparatus

A clamp and chamber were designed and constructed for this thesis for measurements of the hygroexpansion (Fig. 4-2). The clamp is made of aluminum, with a spring-loaded clamp on one end to hold the sample in place. A spring-loaded brass positioner forces the glass slide and Ronchi rulings against the opposite side so that the Ronchi rulings will consistently be in the same position for measurements. The chamber is acrylic with a glass top. There is silicon caulking between the acrylic and glass to provide a tight seal.

Ronchi rulings are precise, evenly spaced, parallel lines on a glass surface (Edmund Scientific, Barrington, NY). The lines are etched grooves in the glass that are filled with black opaque epoxy. The line width is equal to the space width next to it. For this research, a 300 lines per inch (LPI) ruling was used, giving a line width of 42.3 μm (1.67×10^{-3} in.). Reference lines were produced by removing the black opaque from every 20 lines.

A stereo light microscope (Wild M32 Binocular Microscope, Wild, Heerbrugg, Switzerland) was used to view the samples and acquire digital images. This microscope was used because the distance between the stage and lens (≈75 mm) was large enough to position the apparatus under the lens. A digital image was acquired with a digital camera (Sony 3CCD model DXC-750MD, Sony Corp., Tokyo, Japan) and analyzed using image analysis software

(OPTIMAS 5.2, Optimas Corp., Bothell, WA). The distances were measured with the software using manually drawn line lengths.

4.2.2.3 Technique

The dry sample was positioned in the clamp while inside of a glove bag purged with nitrogen. One end of the sample was clamped and the other end was trimmed so that the end was aligned over the Ronchi rulings. The clamp (with the sample) and chamber were stored in a desiccator for 12 hours. The chamber was sealed immediately after it was removed from the desiccator and the measurement of the dry length was made. The chamber was sealed to prevent absorption of moisture by the sample during measurements.

The sample (still in the clamp) was then submerged in water. The clamp was enclosed in the chamber to keep the film saturated with water during measurements under the microscope. A glass slide was first positioned on top of the sample to hold the sample flat against the Ronchi rulings and eliminate buckling of the sample during measurements.

The position of the free end was measured optically through a microscope using Ronchi rulings as a reference (Fig. 4-3). Using the image analysis software, lines were manually drawn from each corner of the sample to the nearest reference line. The calibrated line lengths were extracted from these drawn lines.

4.2.2.4 Analysis

The hygroexpansion was measured as the difference in length between the wet and dry states, divided by the total dry length. The difference was calculated as the difference in position relative to the Ronchi rulings.

$$\%H = \frac{l_w - l_d}{L_d} x100\% \qquad (4\text{-}1)$$

where l_w: distance of the end of the wet sample from reference line 1; l_d: distance of the end of the dry sample from reference line 1; and L_d: total length of dry sample. Measurements were made at the two corners of the sample and the calculations were averaged.

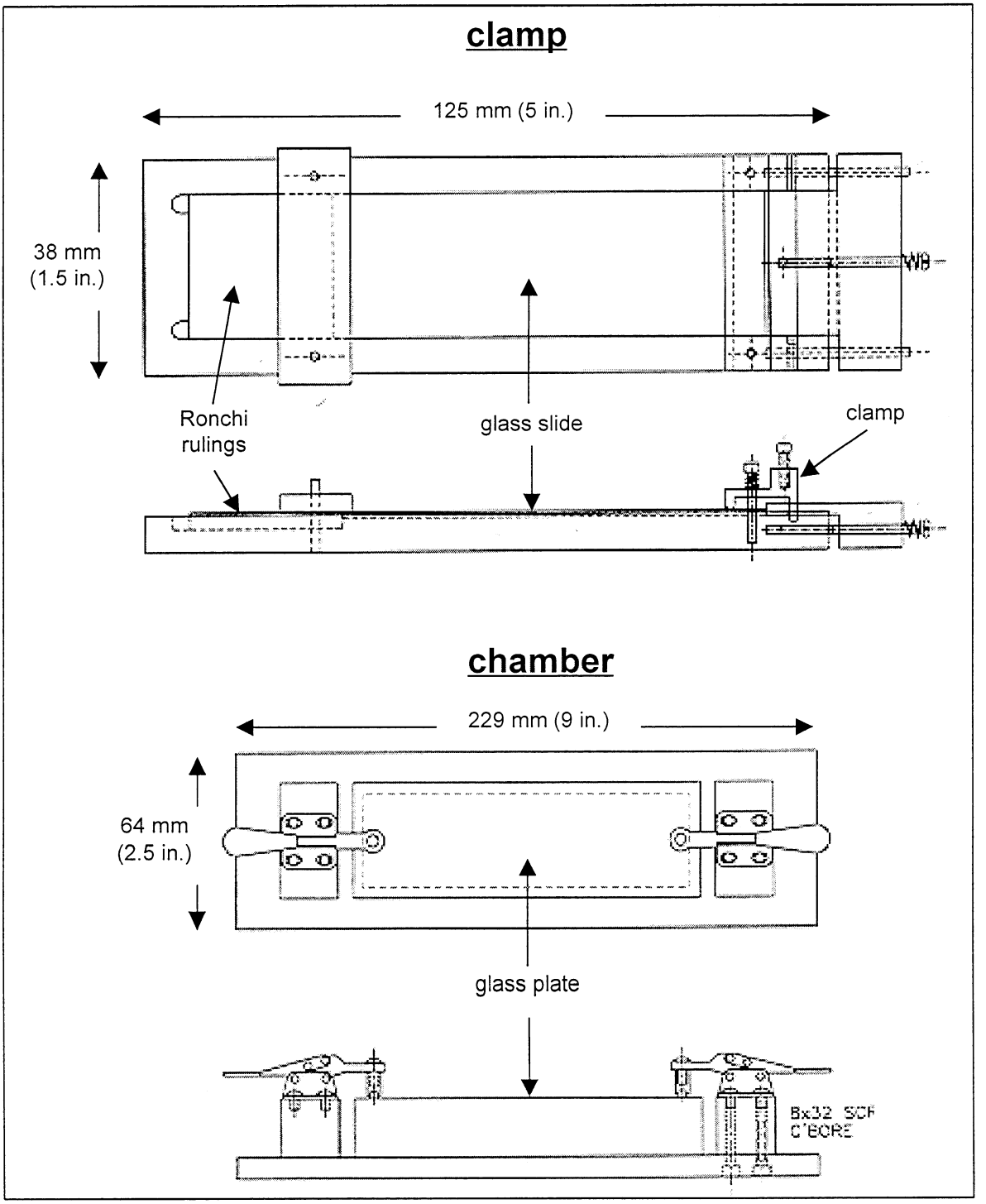

Figure 4-2: Schematic diagram of the clamp and chamber used for the hygroexpansion measurements.

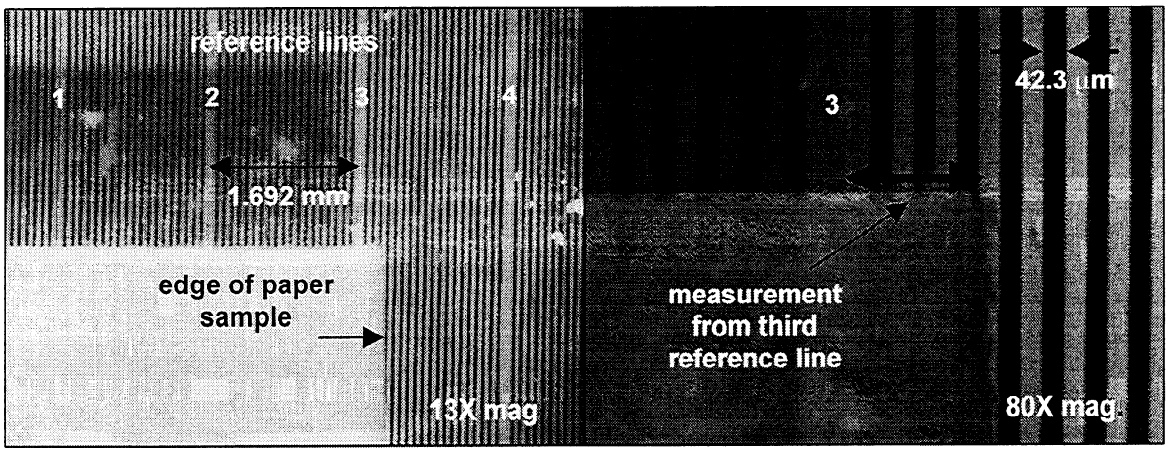

Figure 4-3: View of edge of sample for hygroexpansion measurement. The parallel lines are the Ronchi rulings.

4.3 Toner Line Sample Preparation

Toner lines were prepared on both paper and cellulose acetate by both a manual deposition/fusing of toner powder (model samples) and by printing.

4.3.1 Model samples

Model samples were prepared by depositing a line of toner powder on paper or cellulose acetate and fusing the powder. A stencil (thin section of metal with a slit in the center) was used to control the height and width of the deposited toner powder. The fused toner lines were of approximately the same width and thickness as printed toner lines. The thickness of the model toner lines was varied by using stencils of different thicknesses.

4.3.1.1 Materials

Either Hewlett Packard Laser Jet 4 Plus or Xerox 3700 toner powder (Sec. 4.1.3) was deposited on sections of copy paper. The paper sections [12 mm (0.5 in) x 50 mm (2.0 in)] were cut from a standard sheet of paper. The long dimension of the sections (50 mm) was aligned with the short dimension of the sheet [216 mm (8.5 in)]. The short dimension of the sheet is assumed to be the cross-direction of the paper. Vander Wielen et al. (1999) previously showed

that the orientation of the line on the paper is important for fragmentation. Upon immersion in water, cracks in the line appear primarily perpendicular to the cross-direction of the paper.

4.3.1.2 Apparatus

The stencils were specially fabricated for this work (Microphoto Inc., Roseville, MI). They have a slit of precise width in a thin section of metal (Fig. 4-4). The thickness of the stencil controlled the height of the toner powder and the width of the slit in the stencil controlled the width of the line.

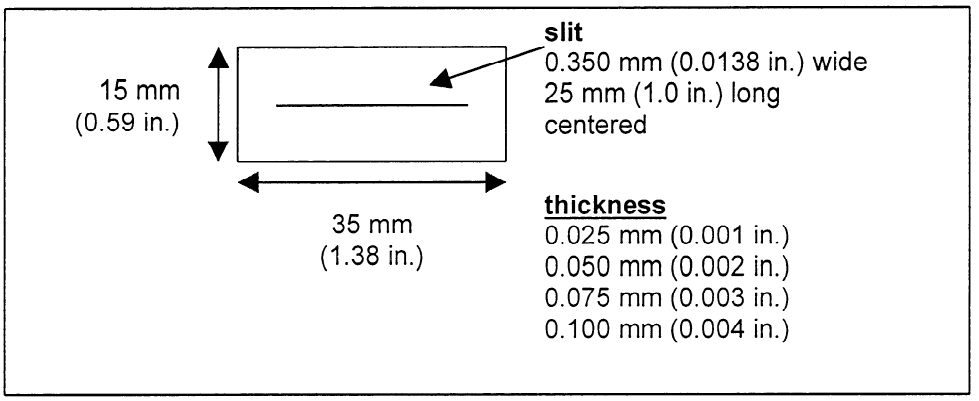

Figure 4-4: Schematic diagram of the stencils used for preparing model toner lines on paper.

The clamp for holding the stencil and substrate in place was the same clamp used for the hygroexpansion measurements. The stencil and substrate were clamped on one end. A glass slide was positioned under the sample for support.

4.3.1.3 Toner powder application

The substrate was positioned on the clamp and the stencil was centered on the substrate. Both were positioned with their narrow ends under the clamping bar, with approximately 3 mm of the stencil under the bar. The screws for the bar were tightened, which firmly clamped the stencil and substrate. With a spatula, a small amount of toner powder was deposited on the stencil at the clamped end, away from the slit. With the edge of a glass slide, the toner powder was scraped across the slit in the stencil. Downward pressure on the glass slide forced the stencil

flush against the substrate, preventing the powder from scattering. After scraping, the toner powder in the slit was visually observed for uniformity. If the powder appeared nonuniform, the scraping was repeated up to three times. The stencil was then carefully removed. A razor blade was inserted under the free end of the stencil to raise it above the height of the powder. The clamp was then loosened and the stencil removed. It should be noted that not all the stencils were initially flat against the substrate. The thinner stencils were curled, but were flattened by the glass slide during scraping.

4.3.1.4 Toner fusing conditions

After depositing the powder, the toner line was heat fused in an oven. Samples made with the Hewlett Packard LaserJet 4 Plus toner were fused at 165°C for 120 minutes. Samples from the Xerox 3700 toner were fused at 100°C for 30 minutes. The fusing conditions were determined qualitatively using visual observations (maximize the sintering of the toner line while minimizing the penetration of the toner into the paper). The HP toner was fused at a higher temperature for a longer time to allow the toner particles to fuse together more completely. The samples were placed on a "non-stick" pan for heating. After fusing, the samples were stored in a desiccator.

4.3.2 Printed samples

Printed samples were prepared in a Hewlett Packard LaserJet 4 Plus printer. Lines were printed across the width of the paper sheet. The paper was handled with gloves. After printing, the paper was cut into sections (12.5 mm x 30 mm). After cutting, these samples were stored in a desiccator. The same cartridge was used for printing as for the model samples.

4.4 Toner Line Thickness Measurements

The dimensions of the toner line were measured with a confocal scanning laser microscope. The dimensions were determined as the difference between the height at points across the line and the height of the surface on either side of the line. A cross-sectional area and width were calculated and used to determine an effective line thickness.

4.4.1 Confocal scanning laser microscope

4.4.1.1 Microscope

The confocal scanning laser microscope was a Lasertec Laser Microscope 1LM21 (Lasertec USA Inc., San Jose, CA). The principles of confocal microscopy are described by Béland and Mangin (1995). The microscope produces a 3-D topographical map, which gives the relative height of the surface.

4.4.1.2 IPST-SVAS software

The IPST-SVAS software (IPST, Atlanta, GA) was used to analyze the roughness of surfaces. The software reads the three-dimensional topographical map from the microscope and allows the dimensions to be analyzed. The software can give the profile of lines drawn across the map.

4.4.2 Acquisition and analysis of data

Samples were mounted on glass slides with double-stick tape for holding the sample flat. The sample was positioned on the microscope stage under the lens. The stage was adjusted to allow scans of the sample along every 2 mm of the toner line. A magnification of 20X was used for the thickness measurements. Raw data of the profiles were obtained from the IPST-SVAS software and analyzed with an Excel spreadsheet program. No filters were used in the IPST-SVAS software. Profiles were drawn across the width of the line to include the paper surface on either side of the line. The profile gave the relative height of the line at increments.

A spreadsheet was developed for this thesis to analyze the profiles. The spreadsheet derived the cross-sectional area and width of the line from the profile data. The baseline for the substrate surface was subtracted to give the height of the line (Fig. 4-5). End-lines were manually set at the edges of the line. The baseline was set by a linear regression of the points outside of the end-lines. A filter was also included in the spreadsheet program to eliminate sharp peaks in the profile. The sharp peaks are artifacts of the scanning at sharp edges (Nanko, 1998). The program "saturates" the location because no surface is detected. The filter removes points above a threshold, plus 10 points to either side of the critical point.

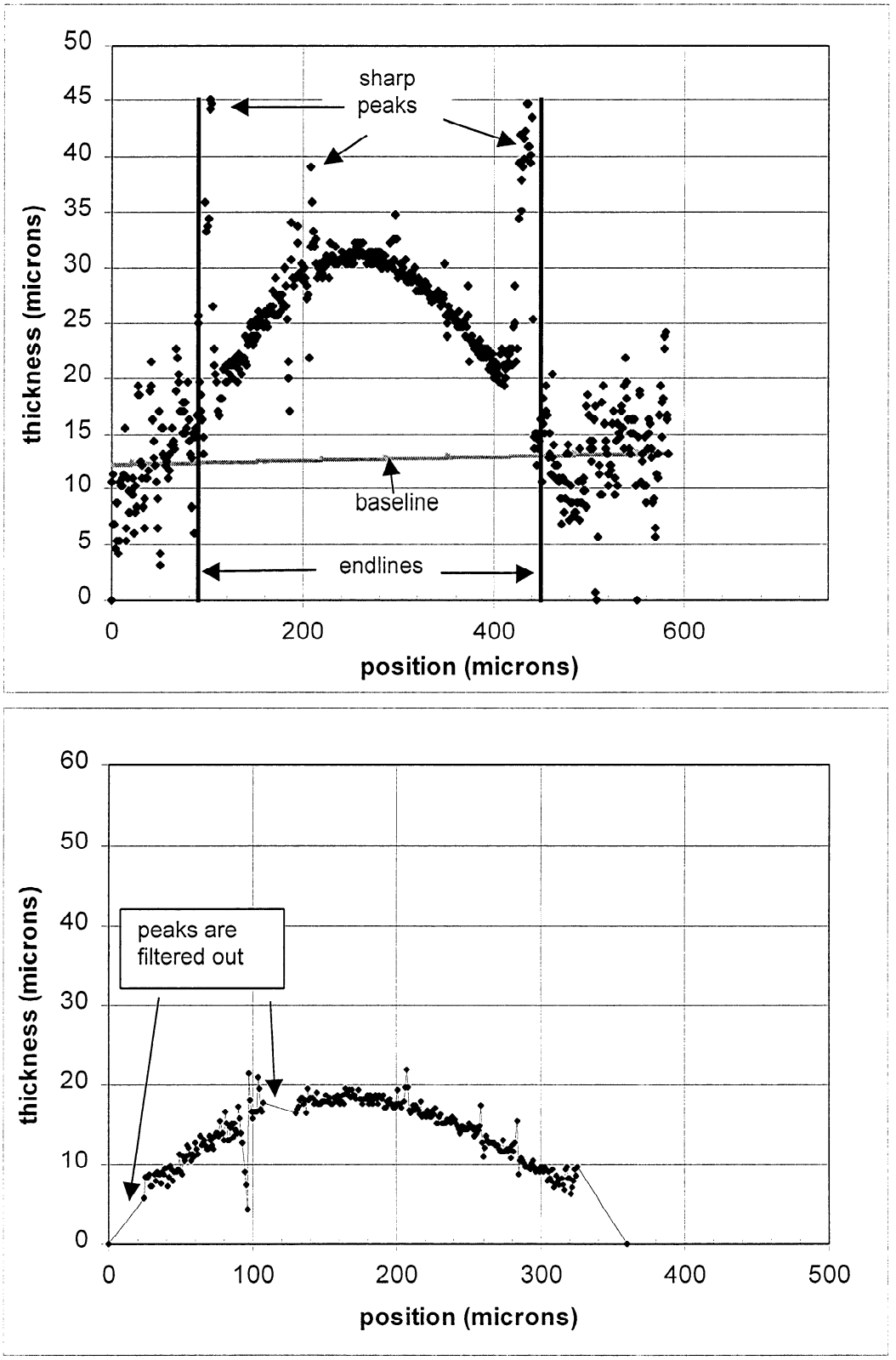

Figure 4-5: Thickness measurements of the toner lines were made by subtracting a baseline from the profile of the surface (top) to give the profile of the line (bottom). The peaks were filtered using a threshold value, in this case, 35. The data were obtained using a confocal scanning laser microscope.

4.5 Fragmentation Tests

The fragmentation tests involved immersing the samples in water or applying a tensile load on the samples, then measuring the distance between cracks (segment length) in the samples. The average segment length for a sample set was combined with the average thickness of the line to produce segment length curves (average segment length versus effective line thickness).

4.5.1 Wet and dry tests

4.5.1.1 Wet test

The wet test involved immersing the toner line samples (toner on paper, toner on cellulose acetate) in water (nanopure, deionized water). All samples were stored in a desiccator for 48 hours after preparation. It was critical that the samples were not tested immediately. The conditioning period allowed the samples to reach equilibrium after preparation and produced more consistent results. The samples were immersed in water one at a time, using tweezers to make sure that they were fully submerged. It was important to immerse the samples individually to allow the samples to expand freely. After two hours of immersion, the segment lengths were measured.

4.5.1.2 Dry test

The dry test involved applying a mechanical tension to the samples along the axis of the line. Toner lines were prepared on 12.5 mm (0.5 in.) x 150 mm (6 in.) sections of paper, using the same preparation techniques described above. Each sample was mounted in an Instron Model 1122 Material Testing Instrument (Instron Corp., Canton, MA). The distance between clamps was set to 125 mm (5 in.). The load was applied [crosshead speed of 12.5 mm/min (0.50 in./min)] until the paper broke. The samples were then immersed in water to make the cracks more apparent. This immersion in water after the test is not believed to create any additional

cracks. This is reasonable because samples from this dry test had many more cracks than samples that were immersed in water only.

4.5.2 Segment length measurement

The sample was mounted between glass slides and viewed under a microscope (ZEISS Axioskop, Carl Zeiss, Inc., Thornwood, NY) using transmitted light. The magnification varied from 25X to 100X. Both the magnification and lighting were adjusted to optimize the appearance of cracks in the line. The sample was viewed with a digital camera (Sony 3CCD model DXC-750MD, Sony Corp., Tokyo, Japan). A digital image was acquired and analyzed using image analysis software (OPTIMAS 5.2, Optimas Corp., Bothell, WA). The distance between cracks was measured using manually drawn line lengths. Using the software, lines were drawn along mid-axis of the toner line with endpoints at the distinct cracks in the toner line. The calibrated line lengths were extracted from these drawn lines.

5 RESULTS AND DISCUSSION: TONER ON PAPER

5.1 Introduction

The fragmentation of toner on paper upon immersion in water was studied to simulate the initial fragmentation of toner in a repulping process. A theoretical model was specifically developed to describe this fragmentation (Sec. 3.4). In this chapter, the bond-site model will be shown to provide a basis for interpreting experimental fragmentation results and for predicting the changes in segment length based on relative changes in parameters. The experimental method involved measuring the distance between cracks (segment length) on samples of toner lines on paper. The experiments included wet and dry tests, tests on two toners, and printed toner line. Results are presented and discussed as segment length curves (mean segment length v. effective thickness). The significance of these results and their relation to deinking will be discussed.

5.1.1 Theory: summary of Kelly-Tyson and bond-site models

The effect of the different fragmentation tests will be discussed in terms of the slope and intercept of the segment length curves. Both the Kelly-Tyson and bond-site models were reduced to linear equations for the segment length curves (mean segment length, $\bar{L}$, versus effective line thickness, h) (Sec. 3.4.4):

$$\bar{L} = f \cdot \frac{\sigma_c}{\tau_B} \cdot h \tag{3-6}$$

$$\bar{L} = f_1 \cdot \frac{\sigma_c}{\tau_B} \frac{1}{\dot{e}} \cdot h + f_2 \cdot \bar{l} \tag{3-40}$$

According to these models, the slope is determined by the critical stress of the line, σ_c, the bond strength, τ_B, and the effective bond length, $\dot{e}$ (bond-site model only). The factors, f_i, are used to estimate the expected segment length from the theoretical critical length. Only the

bond-site model predicts a positive intercept. Both of these models assume a plastic yield of the interface. The Cox model will not be discussed because it predicts a nonlinear segment length curve.

5.2 Experimental – Toner on Paper

Fragmentation was quantified as the distance between cracks (segment length) on a line of toner on paper. The data is presented as a segment length curve. The thickness of the line was varied for all sets. The wet and dry tests were the primary tests on the samples. Two toners were compared (Table 5-1) and the model samples were compared with printed samples.

Table 5-1: Strength and Water Absorption of Toners used in this Study*

	Hewlett Packard LaserJet 4 Plus (HP)	**Xerox 3700 (X37)**
tensile strength**	13.5 MPa	5.5 MPa
water absorption	0.11%	0.56%

** composition of these toners is given in Table 4-1*
***average of two measurements on "dog-bone" samples (Sec. 4.2.1)*

5.2.1 Toner on paper samples

5.2.1.1 Model samples

Model toner line samples were prepared as described in Sec. 4.3. Fig. 5-1 shows images of the toner lines on paper. The lines for both toners appeared continuous for all thicknesses. The thickness of the lines was varied by using stencils of different thickness. A label of "001 stencil" means that a 0.025 mm (0.001 in.) stencil was used to prepare the sample [002 → 0.050 mm (0.002 in.), *etc.*]. The lines were 25 mm in length. The segment lengths and effective thickness were not measured within 3 mm of either end of the line. Prior to preparation, the paper was stored at 50% relative humidity and 23°C. After preparation, the samples were stored in a desiccator.

The alignment of the lines on the paper was important, because paper is an oriented structure. The lines were consistent in alignment, along the narrow dimension [216 mm (8.5

in.)] of the paper sheets. The narrow dimension was assumed to be the cross-direction of the machine-made paper. Using similar samples and technique, Vander Wielen (1997) previously showed that cracks form primarily along the machine direction of the paper, perpendicular to the cross-direction. Aligning the samples along the cross-direction simplifies the quantification of the segment length.

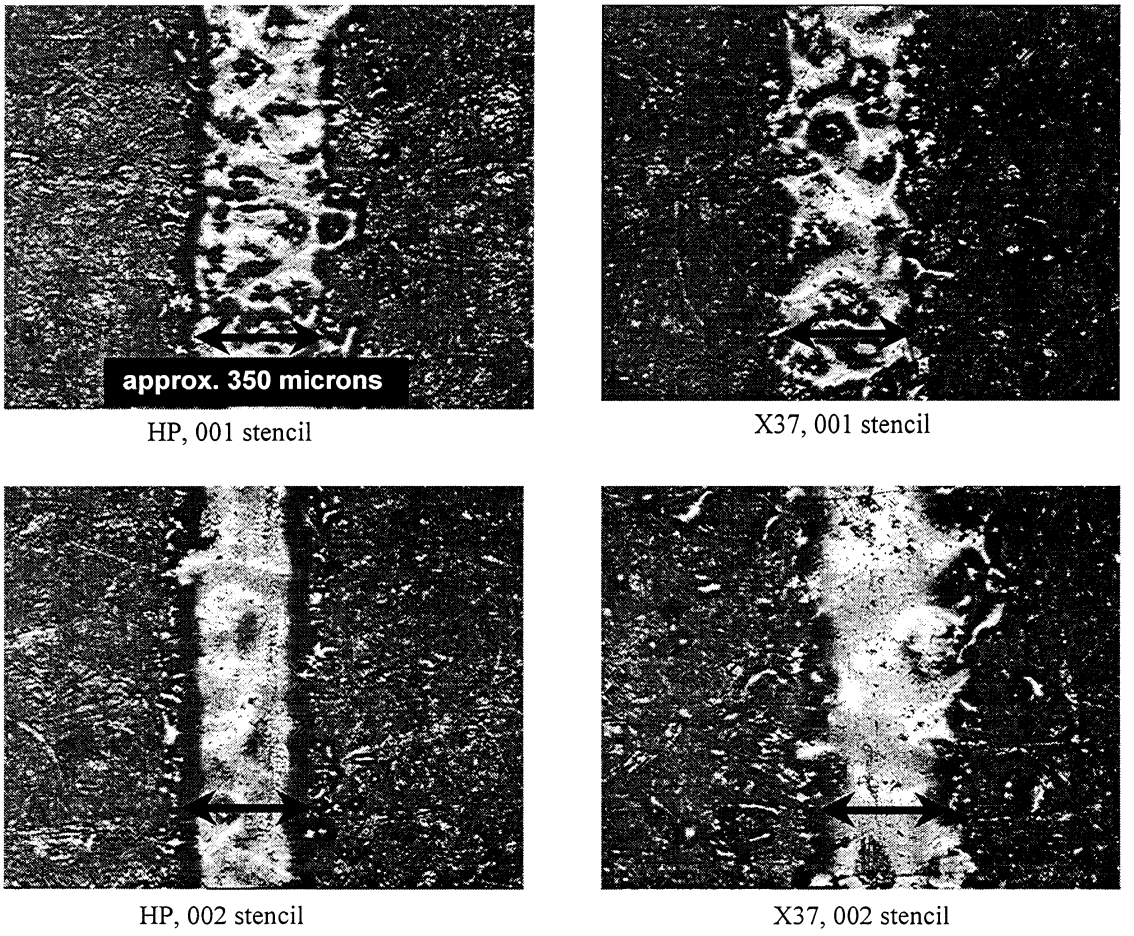

Figure 5-1: Images of toner lines on paper taken with confocal scanning laser microscope (10X). The arrow in each figure is approximately 350 microns in length. (HP: Hewlett Packard LaserJet 4 Plus; X37: Xerox 3700)

5.2.1.2 Printed samples

The lines were printed with a Hewlett Packard LaserJet 4 Plus laser printer. The cartridge used for printing was the same as that used for the model samples. The paper was from the same set of sheets as used for the model samples. Lines were oriented across the narrow dimension of the sheet (cross-direction), as was done with the model samples. The line width

was set to 0.75 points to give lines of approximately the same width as the model samples. Paper was stored at standard TAPPI conditions (23°C, 50%rh) prior to printing. The samples were stored in a desiccator for 48 hours after printing.

The printed and manual toner lines have different structures (Fig. 5-2). The model toner lines appear to be more completely fused. This is reasonable because of the longer fusing time of the model samples. This difference in structure may make the critical stress of the lines different.

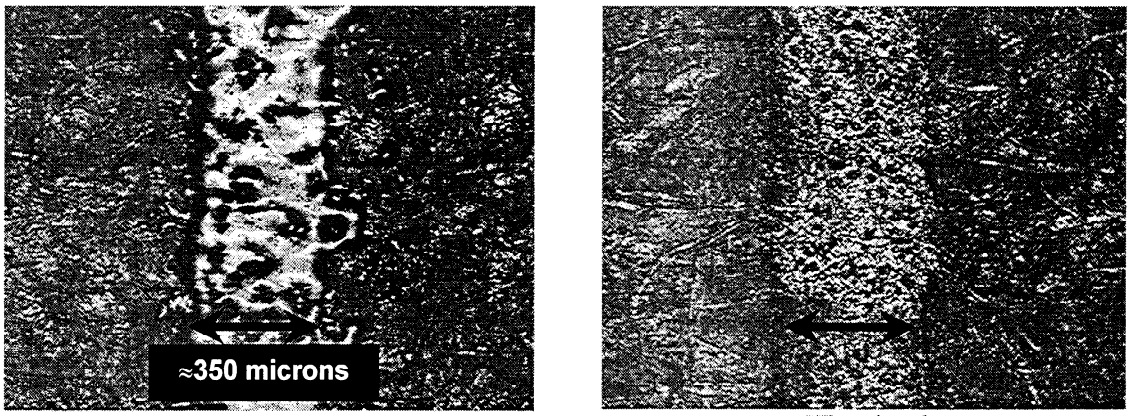

Figure 5-2: Image of a printed toner line on paper compared with a model line (confocal scanning laser microscope, 10X).

5.2.1.3 Effective thickness

The effective thickness for each point is the average cross-sectional area divided by the average width for samples from a given stencil thickness. The cross-sectional area and width were measured at nine locations on each sample (approximately every 2 mm over 19 mm of line). The effective thickness was used to normalize the dimensions of the line based on the one-dimensional force balance used in the stress transfer models (Sec. 3.1.2.1).

It should be noted that the major error in measurement of the effective line thickness is expected to be systematic. The thickness measurement assumes that the average height of the paper surface adjacent to the line is at the same level as the actual bottom side of the toner line. This is complicated because the paper surface is rough, and it is not known whether they are

actually at the same level. However, if they were not the same, the error in measurement would be inclusive at all points. This systematic error would shift all the curves, but not have a significant effect on the curves' relative positions. Thus, the conclusions drawn from the relative positions of the curves should be free of this error.

5.2.2 Fragmentation tests

5.2.2.1 Wet test

The wet test is the standard test to simulate the fragmentation. Samples were individually immersed in water (nanopure deionized water, 23°C). Samples were immersed 48 hours after preparation. For consistent results, it is important that the samples are not immediately immersed in water. The segment lengths were measured at least two hours after immersion.

5.2.2.2 Dry test

The purpose of the dry test was to determine whether a sample with a higher toner-paper bond strength would have a lower segment length. Mechanical tension was applied to a dry sample to produce axial tension in the toner line (Sec. 4.5.2.2). The premise was that a dry sample would have a higher bond-strength and the mechanical force would simulate the hygroexpansion of paper. A difference in the toner-paper bond strength is expected because of the difference in moisture content. The toner's mechanical properties are not expected to be affected by moisture within the time scale of the experiments because the samples are initially dry and each toner absorbs less than 0.6% water (Table 5-1).

5.2.2.3 Type of toner

Hewlett Packard LaserJet 4 Plus (HP) and Xerox 3700 (X37) toners were studied (Table 5-1). The toner was varied to determine whether a toner with a lower tensile strength would produce a shorter segment length, as predicted from the model. Wet and dry tests were done on both toners. This experiment was complicated because the two toners have different melting properties and the samples were prepared using different fusing conditions (HP: fused at 165°C

for 2 hours; X37: fused at 100°C for ½ hour). These differences may affect the bonding or the paper properties. Table 5-2 shows that there was only a slight difference in properties between standard paper and heat-treated paper.

Table 5-2: Effect of Heating on Paper Properties

	reference paper	**heat treated paper** (165°C for 2 hours)
tensile strength* (N/mm)	1.80 ± 0.04	1.91 ± 0.01
tensile modulus** (N/mm)	208 ± 2	214 ± 7
hygroexpansion (%)	2.10	2.03

** maximum load/width*
*** initial slope x gage length/width*

5.2.2.4 Segment length measurements

Figure 5-3 shows a fragmented line after immersion in water. The segment length is measured as the distance between cracks along the mid-axis of the line. Because the cracks are not all parallel with one another, the measured distance may vary by 5 to 10 microns, depending on the location along the crack. However, this variation within a segment is insignificant relative to the variation between segment lengths (standard deviation, 57 to 267 microns). Length measurements are made on images acquired from a microscope using OPTIMAS image analysis software.

The segment length value for each data point is the length-weighted mean for samples from a given stencil thickness. The length-weighted mean was used instead of a number-weighted mean because the theory is length-based, and the length-weighted mean is expected to be less sensitive to variation of the system. A variation that shifts the segment size to a shorter length would produce a disproportionate number of shorter segments than the same shift to a larger length. This is because there are more shorter segments than long segments per length of

line. The distribution would then become skewed to a shorter length. The length-weighted mean is given by (Herdan and Smith, 1953):

$$\bar{L} = \frac{\sum L_i^2 \cdot n_i}{\sum L_i \cdot n_i} \tag{5-1}$$

5.2.3 Segment length curves

The segment length curves were produced from the segment length and effective thickness data. Each point represents the average of the means from samples for a given stencil thickness. The data were pooled because measurements of both the crack spacing and thickness could not be made on the same individual sample. From the pooled data, the sample means and standard error of the mean were calculated. The standard error was calculated for a 95% confidence interval ($\alpha = 0.05$) using the number of samples, n, the standard deviation of the means, s, and the t-value (Appendix II). The t-value was used because the variance of the population was unknown.

5.3 Results and Discussion – Segment Length Curves

5.3.1 Fracture of toner lines

Cracks were clearly apparent in all the samples observed (Fig. 5-3). The line segments do not detach from the surface of the paper. They remain attached in both the wet and dry states, even under mechanical prodding with tweezers.

5.3.2 Effective line thickness

In all the tests, it was clearly shown that the segment length increased proportionally with thickness (Figs. 5-4 to 5-6). The linearity of the data allows the other tests to be discussed in terms of the slope and intercept from a linear regression. The intercept from the linear regression was positive in all the tests. A non-zero intercept is an expected result from the bond-site model,

but not the Kelly-Tyson model. Fig. 5-7 shows that poorer fits are obtained when the data are forced through the origin.

According to the bond-site model, the intercept from the segment length curves is a factor of the bond-spacing (Eq. 3-37). The bond-spacing that was derived from the experimental measurements was on the same order as surface roughness parameters for paper. Bond-spacing is defined in the model as the peak-to-peak (midpoint-to-midpoint) distance between bonds. Surface roughness parameters that may relate to the bond-spacing include wavelength of the profile (measured values: 50 to 100 microns), mean spacing of profile irregularities (10 to 50 microns), and mean spacing of local peaks of the profile ((Standard ISO 4287/1-1984). The surface roughness measurements were made with the confocal scanning laser microscope (Sec. 4.4.1) and were sensitive to threshold settings and location, leading to a range of values.

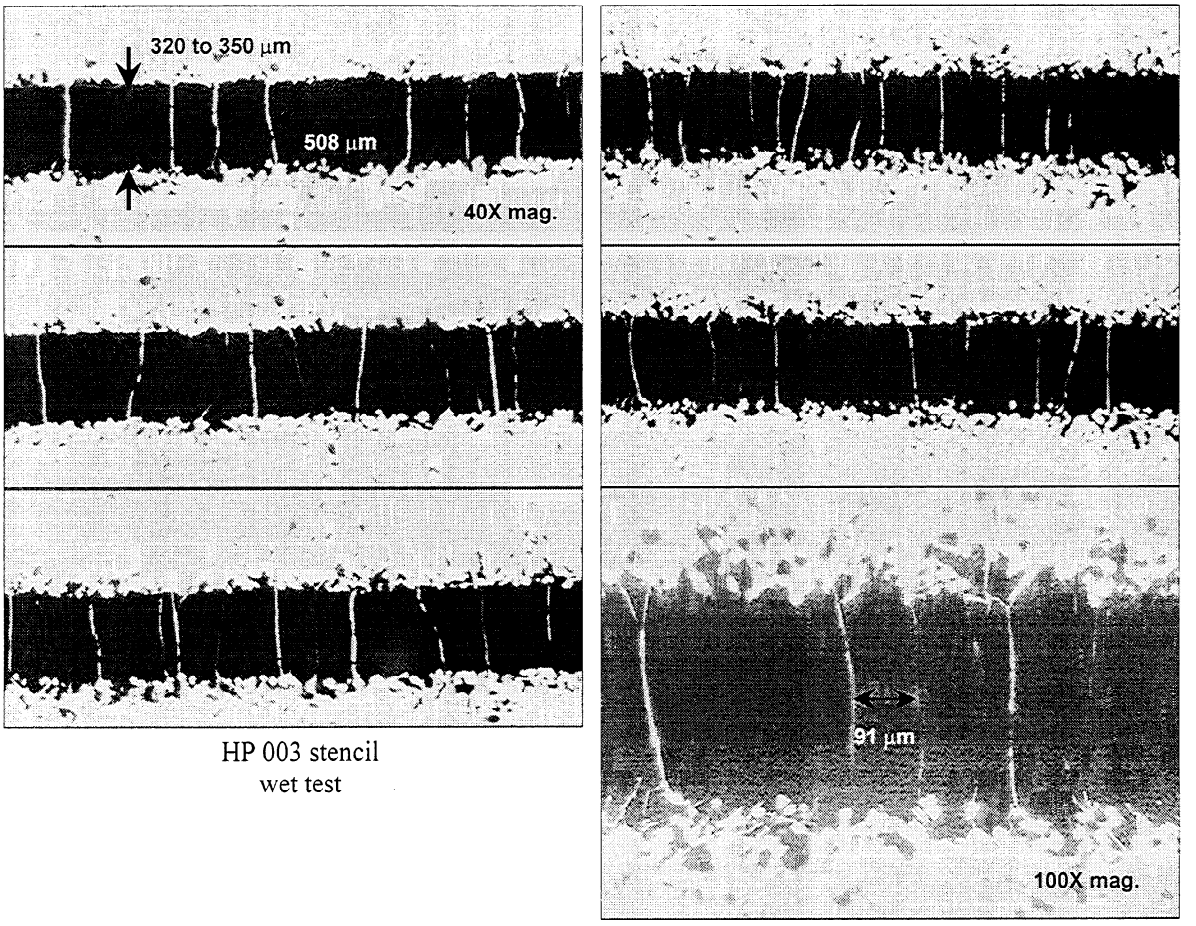

HP 003 stencil
wet test

HP 002 stencil
dry test

Figure 5-3: Images of model toner lines on paper after immersion in water (light microscope, 40 and 100X).

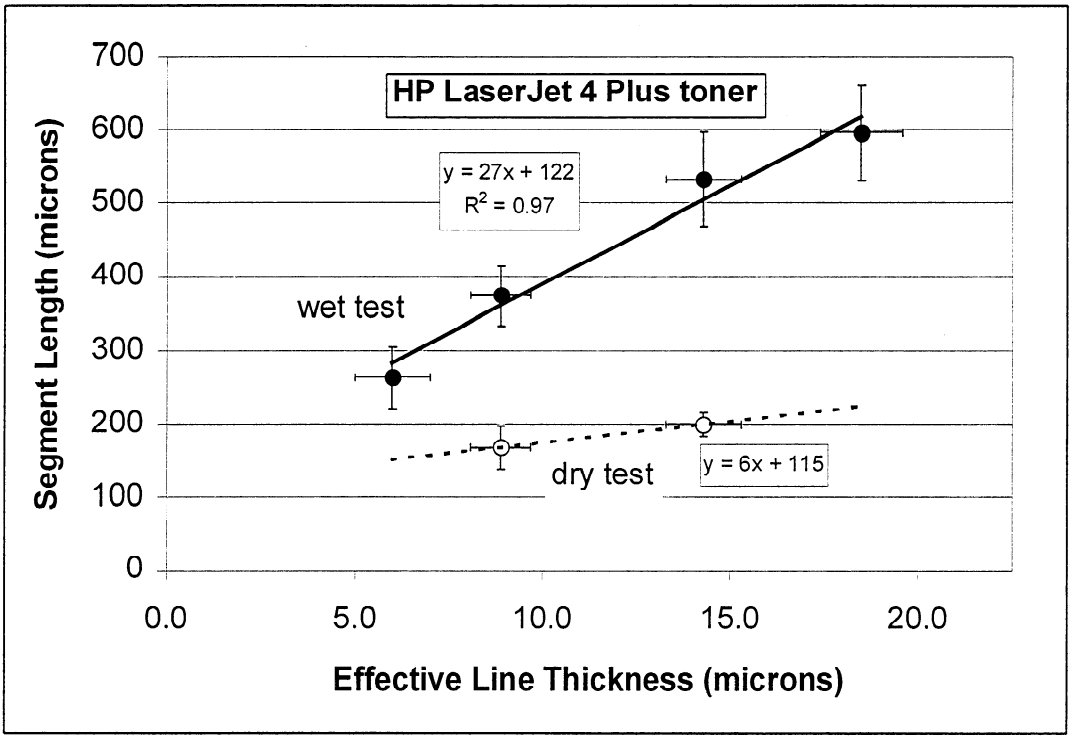

Figure 5-4: The dry test produced a significant decrease in segment length from the wet test for the HP toner.

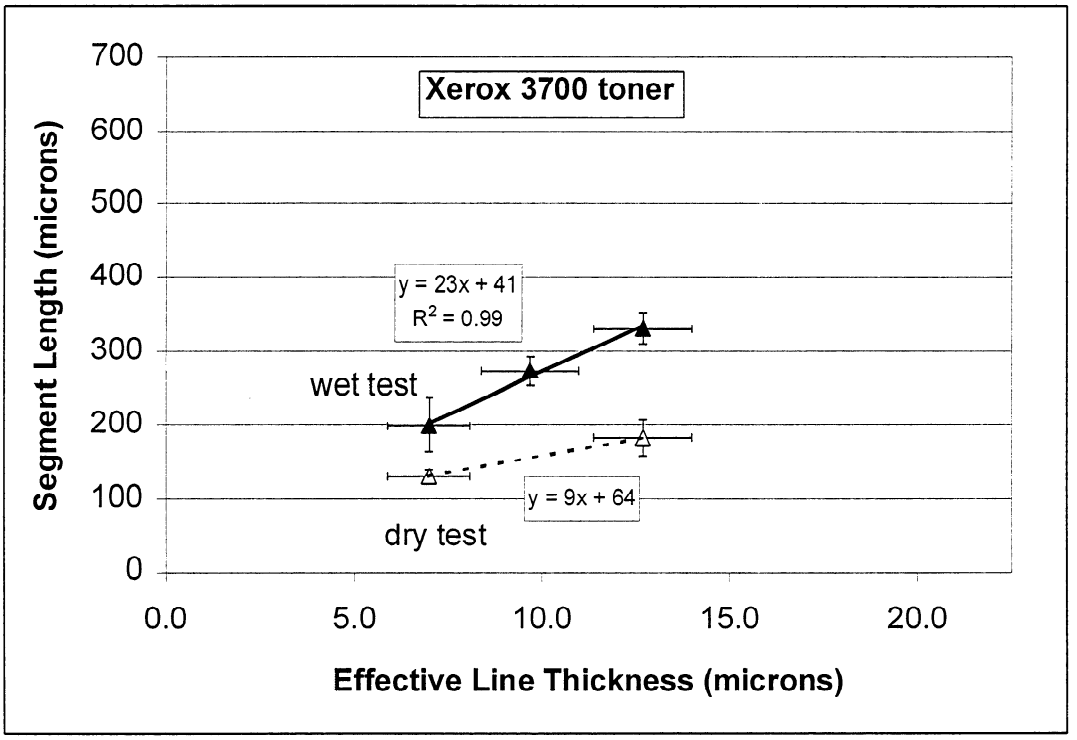

Figure 5-5: The dry test produced a significant decrease in segment length from the wet test for the Xerox toner.

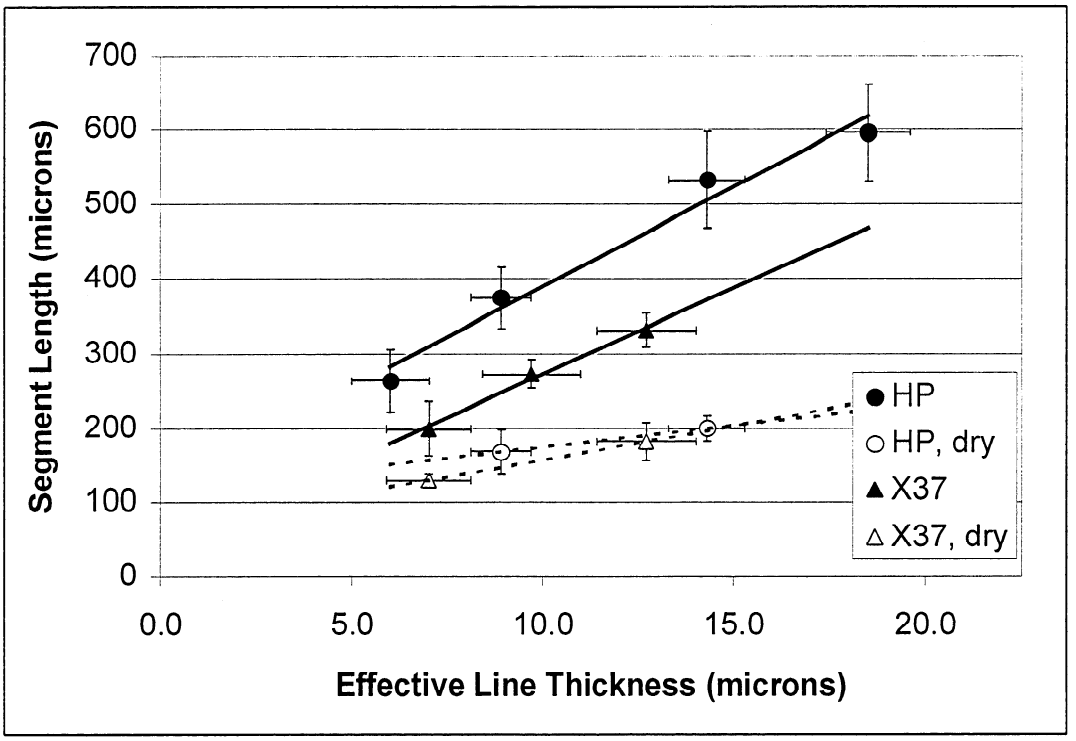

Figure 5-6: The HP toner had a higher segment length than the X37 toner for the wet test. There was not a significant difference between the dry tests.

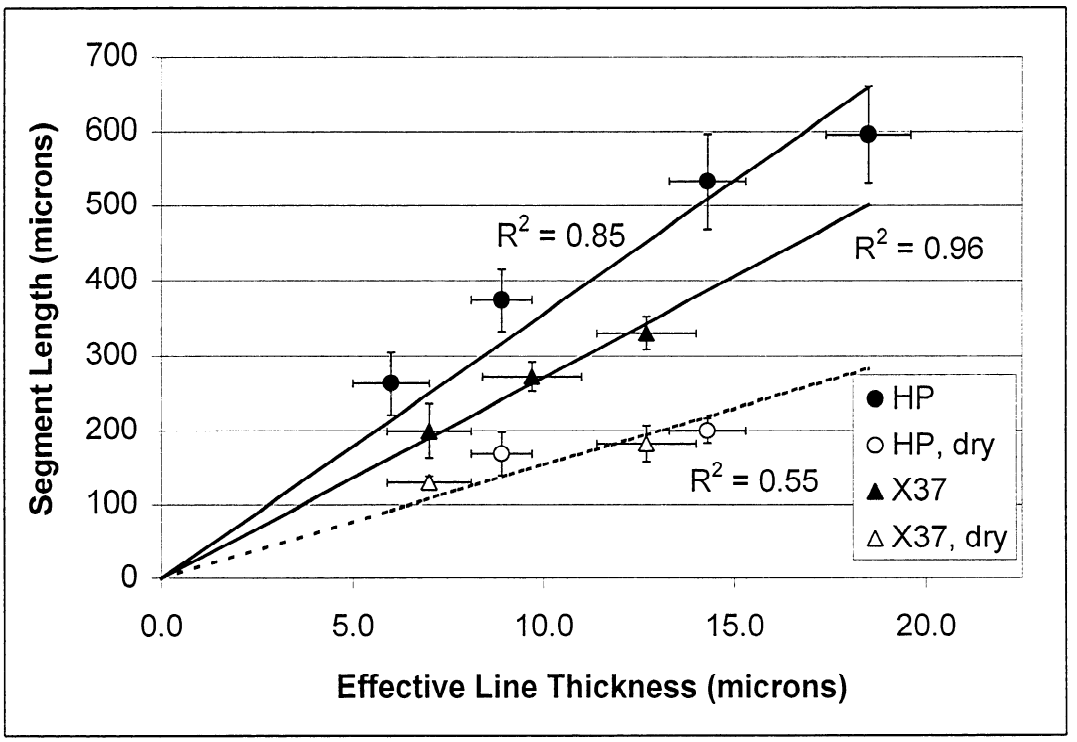

Figure 5-7: Comparison of segment length data with the Kelly-Tyson model. The linear regression for each set was forced through the origin.

5.3.3 Dry tests

For both toners, the curve for the wet test had a greater slope than that of the dry test (Figs. 5-4, 5-5). In terms of the bond-site model, the increase in slope is interpreted as a decrease in the bond-strength. The intercepts were similar for each type of toner, indicating that the bond-spacing is the same.

The dry test is expected to have toner-paper bonds with a greater average strength than the wet test. Bond strength was defined as a composite property of the toner-paper bond, which includes the toner-fiber interface, fiber, and adjacent fiber-fiber interfaces (Sec. 3.4.1.2). A change in properties of any of these components could change the toner-paper bond strength. In the dry test, the bonds remain dry throughout the test. In the wet test, the bonds are dry initially, then absorb water with time. The difference in bond-strength can be indicated by the difference in fiber modulus and fiber-fiber bonds. Dry cellulosic fibers have a higher modulus than wet fibers (Kolseth and Ehrnrooth, 1986). Dry fiber-fiber bonds are clearly stronger than rewetted bond, as shown by the relative ease to disintegrate wet paper into individual fibers.

The change in bond strength between the wet and dry test can be estimated using the bond-site model. Assuming that the other parameters remained constant, the ratio of bond strengths is given by the ratio of the slopes from the segment length curves for the wet and dry tests.

$$\frac{\text{slope (wet)}}{\text{slope (dry)}} = \frac{\frac{3}{2}\frac{\sigma_c}{\tau_B^w \cdot \dot{e}}}{\frac{3}{2}\frac{\sigma_c}{\tau_B^d \cdot \dot{e}}} = \frac{\tau_B^d}{\tau_B^w} \qquad (5\text{-}2)$$

The HP toner gave a ratio of 4.5 (dry:wet) and the X37 toner gave a ratio of 2.6. (The reason for the difference between the HP and X37 toners will be discussed further in Sec. 5.3.4.) These ratios are in the same range as the dry-to-wet ratio of the elastic modulus of fibers, 1.8, 2.9, 4.8, and the relative rigidity (torsion pendulum) of dry-to-wet bleached kraft fibers, 5.6

(Kolseth and Ehrnrooth, 1986). This provides solid support that the difference between the wet and dry tests was primarily a difference in the bond strength.

It is reasonable that the dry test has reached the limit of fragmentation. The curves are fairly flat, indicating that the segment lengths may be on the order of one to two bond-sites. The theoretical critical length may be less than the length of one bond-site, which is not physically obtainable. As discussed in Sec. 3.4.4.2, the segment length is expected to be horizontal if the expected segment length is less than the length of one bond-site. This indicates that the dry test may provide a minimum limit to the segment length.

5.3.4 Type of toner

The wet test showed a significant difference between the two toners, while there was not a significant difference between points for the dry test (Fig. 5-6). The curves for the wet test from the two toners had similar slopes and different intercepts. The expected difference in slope due to a difference in tensile strength was not apparent. According to the bond-site model, the difference in intercept indicates a difference in bond-spacing.

A difference in bond-spacing is reasonable, because the two toners had different flow properties. The toner line may have penetrated further and come into contact or mechanically interlocked with additional bond-sites (Fig. 5-8). Prime (1983) and Forgo *et al.* (1993) showed a strong effect of the viscoelastic properties and the fusing conditions on the degree of fixing of toner to paper. The X37 toner may have been less viscous and penetrated into the paper surface further. There was not a direct measurement of the bonding, however this is reasonable because the HP toner required a higher time and temperature to sinter during fusing for the sample preparation

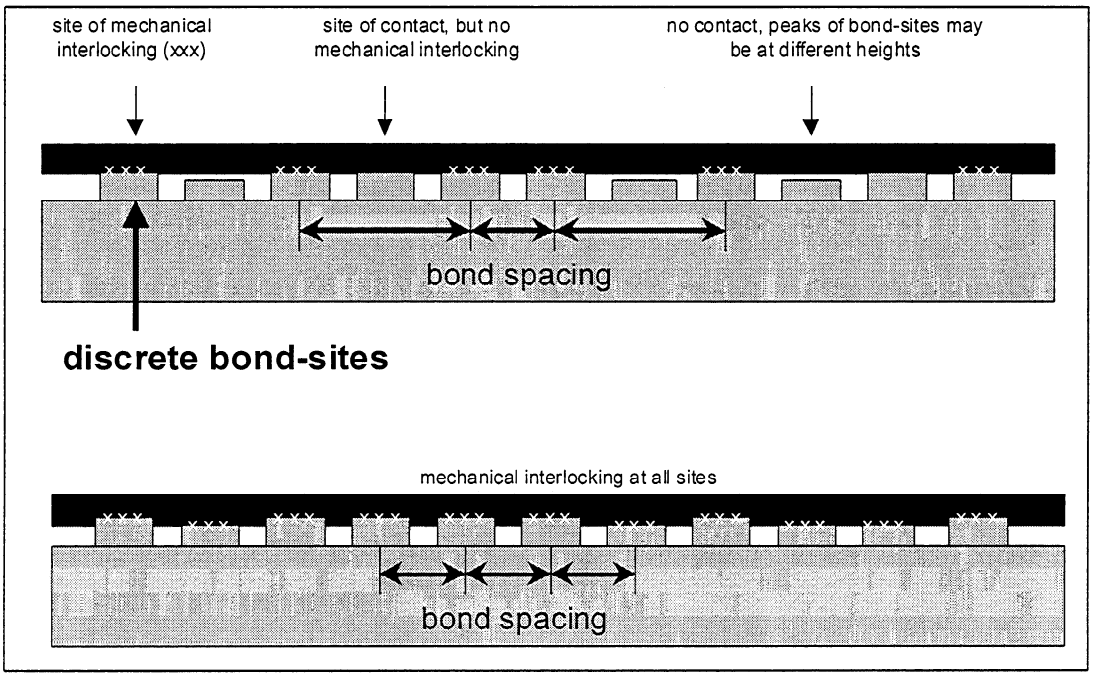

Figure 5-8: On the same paper surface, the bond-spacing may be different if the toner penetrates into the paper differently.

The dry tests did not show a significant difference in segment lengths between the two toners. As discussed above, this may be a result of the dry tests approaching the limit of the fragmentation model. The segment size appears to be approximately the same length as one bond-site. This may reduce the sensitivity of the segment length to changes in parameters.

An effect of a difference in critical stress was not apparent from the data. The critical stress may have actually been similar between the two lines, or any effect from a difference in critical stress may have been masked by a difference in bonding. The critical stress of the toner line was expected to be significantly different between the two toners, based on bulk tensile strength measurements. However, the measurement of bulk tensile strength may not provide an accurate estimate of the critical stress of the lines. The fracture energy of the toner may be a better estimator; however, a fracture mechanics analysis requires the knowledge of size and frequency of microscopic flaws in the toner line (Gibson, 1994).

Alternatively, a decrease in critical stress may have been opposed by an increase in effective bond length. According to the model, both parameters affect the slope of the segment

length curve. It is reasonable that the fractional effective bond length, $\dot{e}$, increased due to greater penetration of the X37 toner, as discussed above. These results clearly show that it is not simple to isolate the effect of a single parameter.

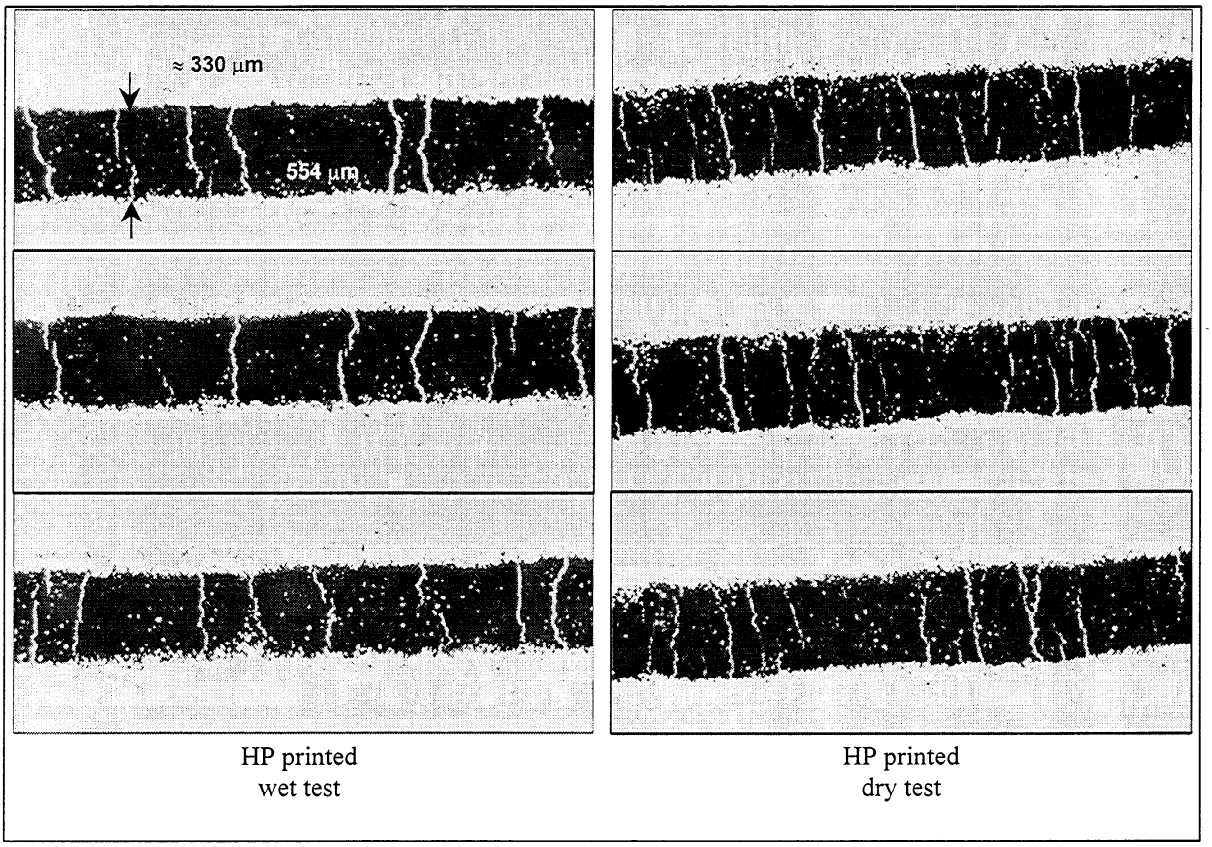

Figure 5-9: Images of printed toner on paper after immersion in water (light microscope, 40X).

5.3.5 Printed toner

Figure 5-9 shows the fragmentation of printed toner on paper after immersion in water. The segment length was compared with the wet and dry tests from model HP toner samples. The single points are shown in a segment length curve (Fig. 5-10). The point from the wet test was significantly greater, while the dry test segment length was slightly greater.

The increase in segment length for printed samples is likely due to a decrease in effective length per bond or the bond-spacing. The primary difference between the two sets of samples is the sample preparation. The difference in the fusing conditions could affect either the effective

length per bond or the bond-spacing. The printed toner is molten for a much shorter time; therefore, it is reasonable that it has less penetration into the paper. The appearance of the printed line indicates that there was less flow of the printed toner.

The appearance of the printed line indicated that the printed line has a lower critical stress. The printed line is fused less completely and the structure should fracture at a lower critical stress due to more stress concentrations. If the critical stress were lower (everything else constant), the segment length would also be expected to be lower. However, the opposite effect was found. This is likely because of a stronger effect of the difference in bonded area (effective length per bond and bond-spacing).

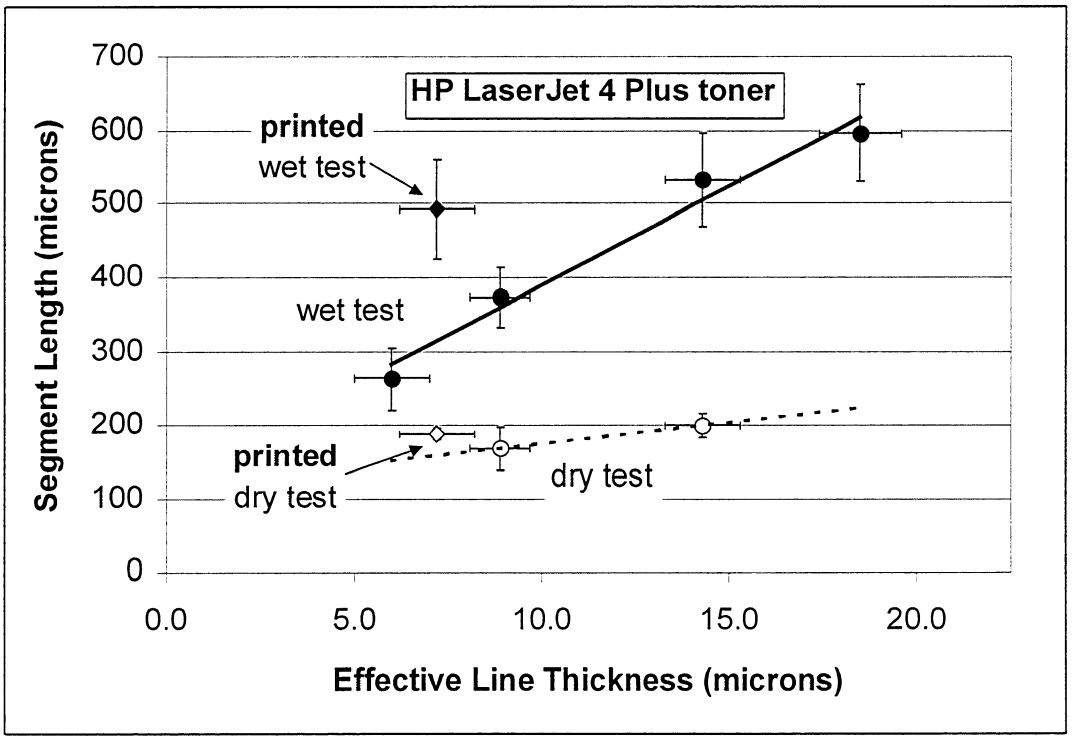

Figure 5-10: The printed samples had greater segment lengths than the model samples for both the wet and dry tests.

5.4 Discussion – Segment Length Distribution

5.4.1 Standard deviation

Table 5-3 shows the number-weighted mean and standard deviation from the pooled data. The coefficient of variation (Eq. 5-3) was fairly constant for the different sample sets. This shows that it is reasonable to estimate the standard deviation, s, from the mean segment length (number-weighted), $\tilde{L}$, using a coefficient of variation (CV) of 54%.

$$CV = \frac{\tilde{L}}{s} \tag{5-3}$$

Table 5-3: Coefficient of Variation for Segment Lengths of Two Different Toners

	mean (microns)	standard deviation	coefficient of variation
HP LaserJet 4 Plus			
printed	367	215	59%
printed – dry test	153	73	48%
001*	218	100	46%
002	288	158	55%
002 dry test	135	67	50%
003	380	242	64%
003 dry test	162	79	49%
004	413	255	62%
Xerox 3700			
001	157	82	52%
001 dry test	109	57	52%
002	206	114	55%
003	249	143	57%
003 dry test	138	79	57%
		average	54 ± 6 %

** the number refers to the stencil thickness used to prepare the sample, e.g., 001: 0.025 mm (0.001in.) stencil*

The constant coefficient of variation shows that the standard deviation increased as the mean segment length increased. This is expected from the fragmentation models. The bounds of the expected segment length increase with increasing segment length. Theoretically, the

fragmentation mechanism gives a coefficient of variation around 20%, assuming a uniform distribution. The additional variation of the segment length is due to variation of the experimental system such as thickness, bond-strength, and line strength.

5.4.2 Probability distribution curves

Figure 5-11 shows histograms for some of the data sets. All the histograms are bounded by zero and skewed toward zero. This is reasonable because the segment lengths cannot be less than zero and the shorter segments give a relatively higher count per length (*i.e.*, there is a higher number of shorter segments than long segments for the same length).

Figure 5-11 shows that gamma distribution gives a reasonable fit over a range of experimental distributions. The experimental data are better fit with a gamma distribution than the log-normal distribution. The gamma and log-normal functions were investigated because they are functions that are bounded by zero, are skewed toward zero, and their parameters can be easily calculated from experimental data (Appendix III). A theoretical justification is not known at this time. However, it must be noted that it is significant that the gamma parameters can be calculated from the experimental data, rather than by simple curve fitting. The gamma curve thus gives a meaningful description of the data.

The shape and width of the segment length distribution is influenced by distributions of the parameters that affect the segment length (*i.e.*, tensile strength of the line, thickness of the line, shear strength of the interface, effective length per bond, distance between bonds). The distribution of each of the parameters will have its own shape and width, which will contribute to the segment length distribution. The segment length distribution is therefore a complex function of a number of distributions. This does not allow a simple interpretation of the segment length distribution from the distribution of any one of the parameters.

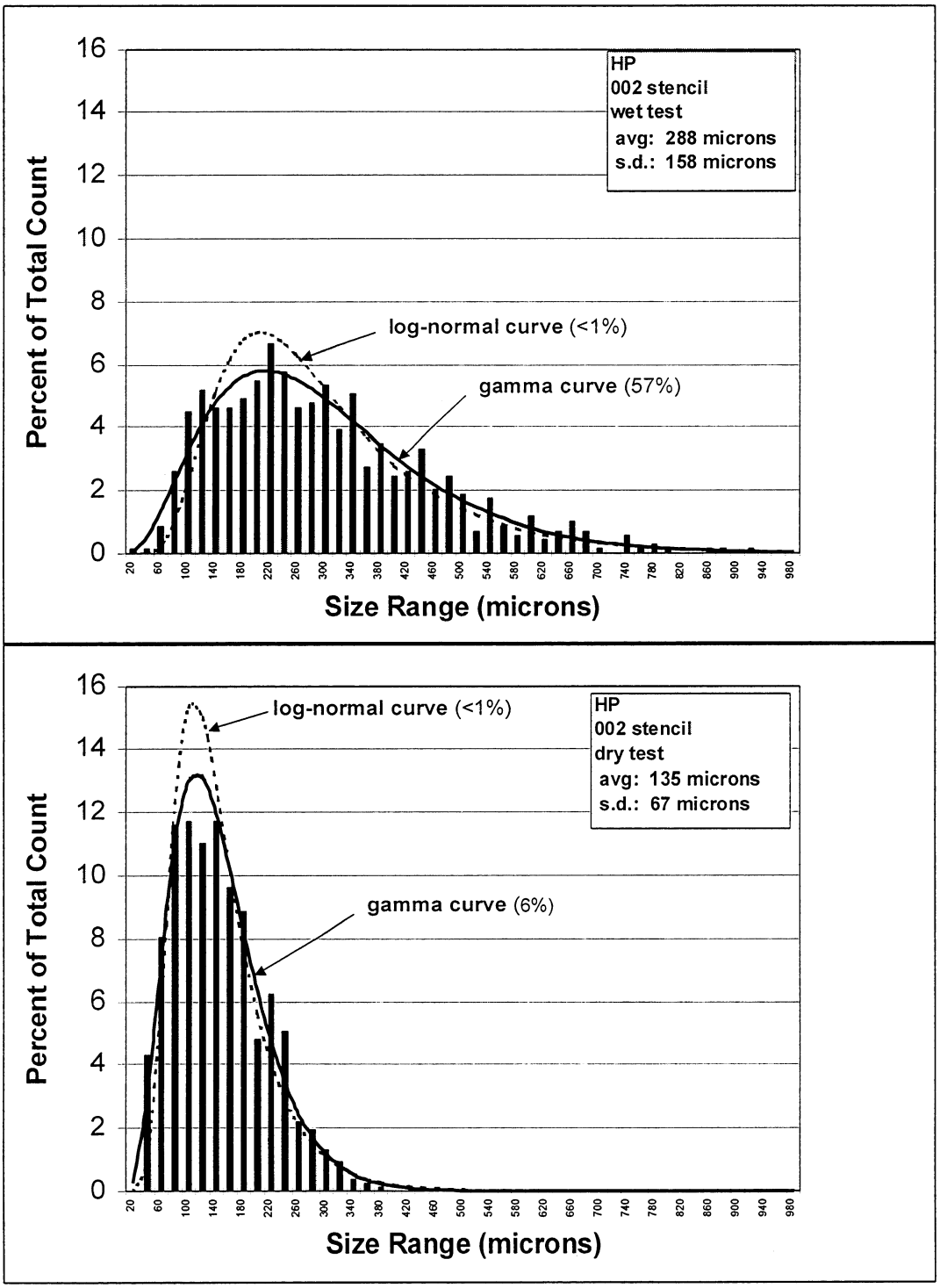

Figure 5-11: The segment length distribution can be fit with a gamma curve, using parameters calculated from the mean and standard deviation of the data. The values in parenthesis are goodness-of-fit probabilities using the chi-squared test (100% is a perfect fit).

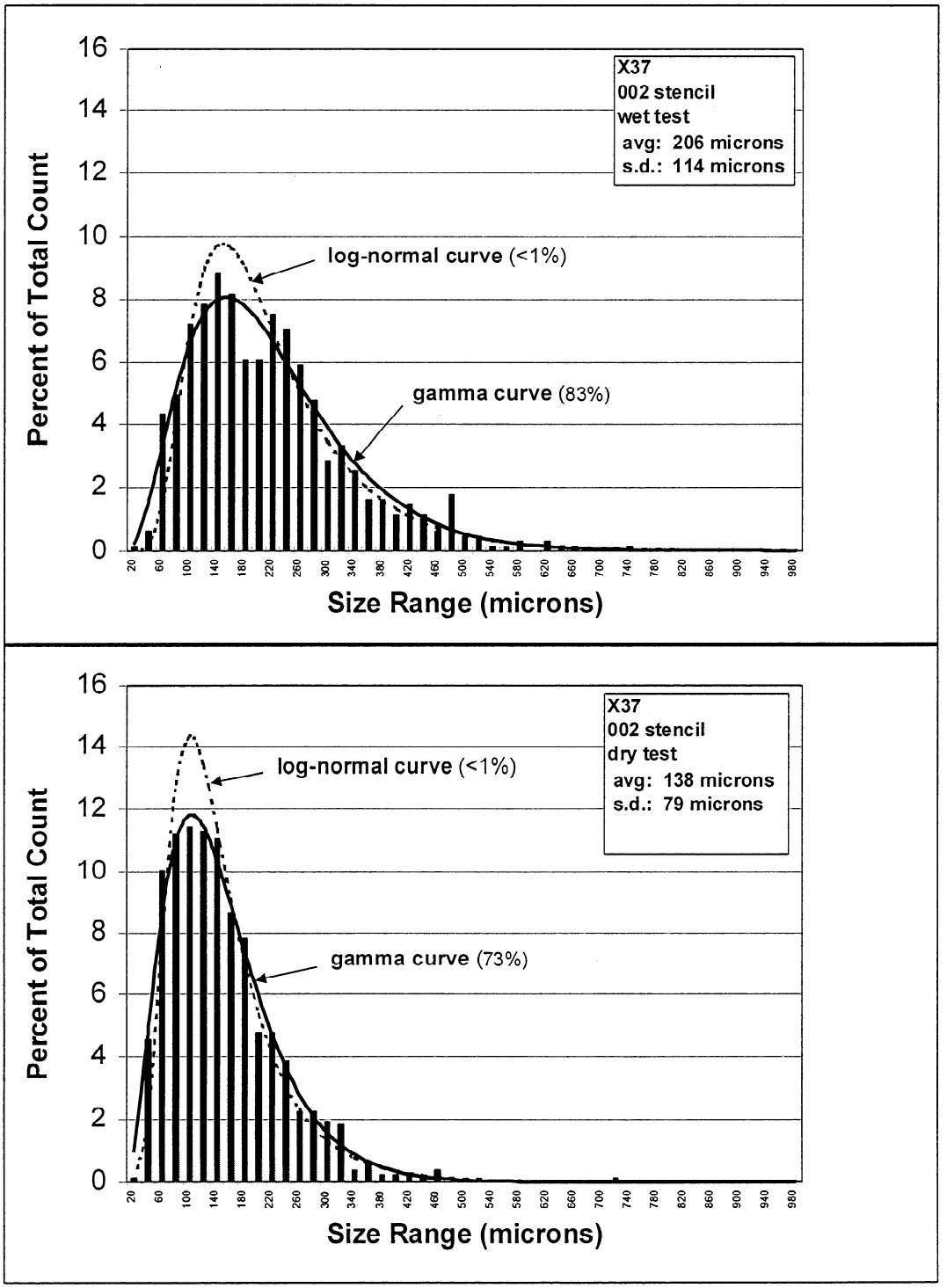

Figure 5-11 (continued): Segment length distributions for two samples prepared from Xerox 3700 toner.

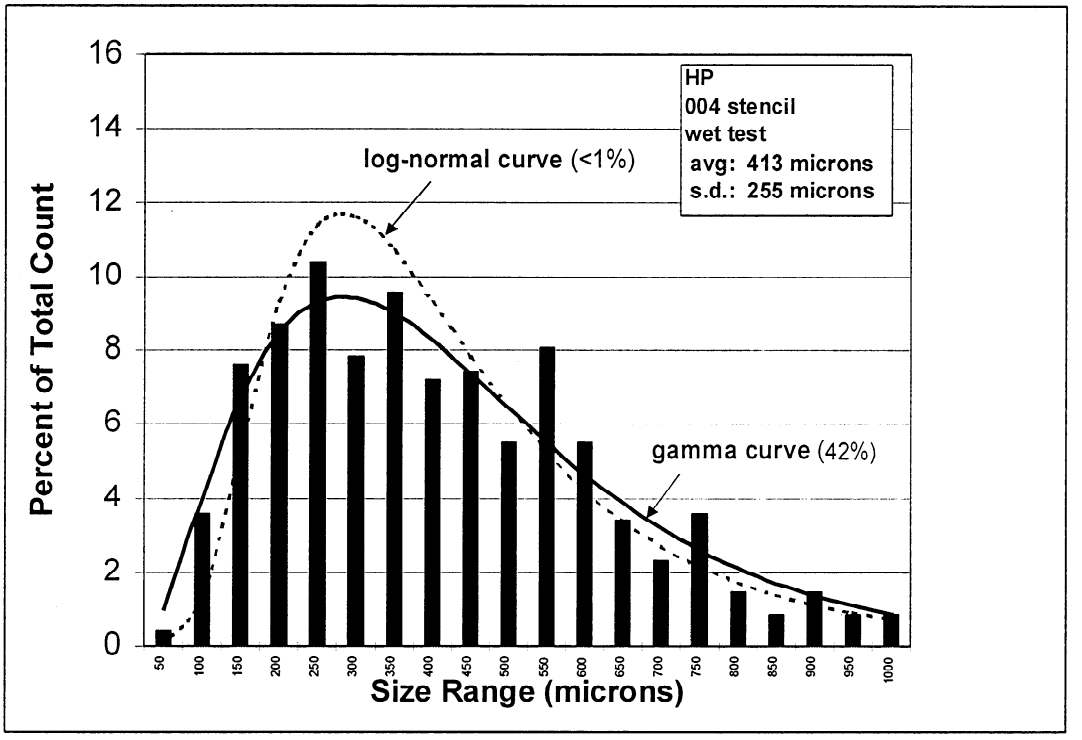

Figure 5-11 (continued): Segment length distribution for the HP toner samples prepared with the thickest stencil.

5.5 Discussion – Bond-site Model

The purpose of this research was to produce a model for describing the fragmentation of toner on paper upon immersion in water. The bond-site model was developed theoretically to model the fragmentation. In this section, the bond-site model will be supported by evidence from analysis of the segment length data, from physical observations of the fragmentation, and a theoretical justification.

5.5.1 Segment length data

Plotting the segment lengths versus effective thickness gave insights into features of fragmentation that are not obvious from comparison of single measurements. Analysis of the segment length data gave the following results:

- segment length is proportional with effective thickness
- segment length curve has a non-zero intercept
- segment length decreases with an increase in bond-strength
- variance increases with increasing mean segment length

The linear increase in mean segment length with effective thickness supports both the Kelly-Tyson and bond-site models. The bond-site model is further supported by the non-zero intercept of the curves. This shift in the curve is an outcome of the segments fracturing at discrete locations along the line (Sec. 3.4.4), a feature not included with the Kelly-Tyson model. According to the bond-site model, the intercepts should be a fraction (1/4) of the bond-spacing. The bond-spacing derived from the intercept was on the same order as the roughness of the paper surface. The bond-spacing is expected to be a function of the roughness of the paper surface and bonding of toner to the paper surface. The bonding may change due to use of a different toner or fusing conditions (printed toner) (Secs. 5.3.4, 5.3.5).

The decrease in segment length due to an increase in toner-paper bond strength was shown by the dry test. The dry test is believed to simulate hygroexpansion, changing only the

bond-strength while expanding the paper. Based on the experimental change in segment length, the bond strength increased by 2.6 to 4.5 times, in the same range as a ratio of dry-to-wet fiber modulus.

The increase in standard deviation with the increase in mean length is expected from all of the fragmentation models. Theoretically, the segment length should vary from l_c to $(2l_c - 1)$, regardless of the model. The variation was greater than that predicted by the model because of variation of the physical system.

An attempt to isolate the effect of critical stress of the toner line was not successful. The experiment was complicated by a difference in fusing between the two toners studied. Regardless, there were no discrepancies between the model and experimental data and all the data can be reasonably explained.

5.5.2 Physical observations

In addition to the segment length data, observations of the physical system provided additional support to the bond-site model:

- hygroexpansion of paper
- no detachment of toner segments from the paper
- no major pre-existing cracks in the toner lines

The hygroexpansion of paper was measured at 2.0%, which is at least a ten-fold difference from the estimated hygroexpansion of toner at equilibrium. A measurement of the hygroexpansion of toner was not made. Based on the equilibrium moisture content of the toners and assuming isotropic expansion, the uniaxial expansion at saturation was estimated to be 0.03% for the HP toner and 0.2% for the X37 toner. A significant difference in hygroexpansion between the paper and toner is necessary for the use of the model to describe fragmentation upon immersion in water. The stresses develop because of a difference in expansion. Also, the expansion of the paper was greater than the estimated fracture strain of the toners (0.2 to 1.0%).

Using similar samples and technique, Vander Wielen *et al.* (1999) showed that there were not significant pre-existing cracks in the toner lines prior to immersion in water. The cracks were formed due to hygroexpansion of the paper from stress transfer to the toner line. This shows that the difference in hygroexpansion between the toner and paper produces enough stress to fracture the line.

The lack of detachment of toner segments from the surface showed that there was no clean fracture of the toner-paper bond. This indicates that the stress transfer to the toner line was limited by yield of the interface, as expected by the Kelly-Tyson or bond-site model. The yield may occur as slippage at the fiber-fiber bonds or shear deformation of a single fiber.

5.5.3 Theoretical justification

The bond-site model is a modification to a commonly used existing model (Kelly-Tyson model). The modifications were made specifically for the toner on paper system to account for the discontinuity of the interface. The model is believed to be sufficient for comparing relative changes in segment length. Errors that arise from the approximations are minimized because the approximations are inclusive for all samples, thus should cancel out when comparing relative differences.

5.6 Discussion – Significance to Deinking

This work simplifies the fragmentation of toner to a few key parameters, which allows fragmentation to be discussed in terms of the relative magnitude of the parameters and the effect of process conditions (*e.g.*, temperature, pH) on the parameters. This may be used to more clearly interpret experimental deinking results and predict the effect of changes in the system. Further, the dry test gives a baseline for the minimum segment length and variance expected from this mechanism.

It is noted that these results only show the fragmentation due to hygroexpansion of the paper. To fully describe the fragmentation during deinking, it is still necessary to determine effect of mechanical forces. These results are still meaningful because it gives an upper limit for the initial segment sizes. The particles will only become smaller, not become larger, unless agglomeration conditions are used. Also, the fragmentation test described here may be useful for investigating relative differences. A difference shown by this test may be apparent even after intense mechanical forces during repulping. Vander Wielen *et al.* (1999) previously showed that the effect of temperature (either below the toner's glass transition temperature or above) on the particle size was analogous for both an immersion test and repulping at 11% consistency for 10 minutes.

5.7 Conclusions – Toner on Paper

The fragmentation of a toner line on paper can be described by the bond-site model. The model can be used to interpret and predict differences in segment length, but not absolute values. The complexity of the experimental system does not allow simple independent measurements of the model's parameters or allow isolated changes of the parameters. Regardless, the experimental results were consistent with the model.

The segment length was experimentally determined using toner lines fused to the paper surface. The toner line samples were immersed in water and the distance between cracks (segment length) was measured. The experimental results clearly showed an increase in segment length with increasing effective line thickness. Linear curve fits of the results showed a non-zero intercept, which is an expected result from the model. Further, there was strong experimental evidence that the segment length decreased due to an increase in toner-paper bond strength. Experiments to isolate a change in the critical stress of the toner line by using a different toner were not successful. While the segment length was greater for a toner with a higher tensile

strength, the difference in segment length appeared to be more likely the result of a difference in bonded area between the toner line and paper, rather than a difference in the critical stress. Even though the effect of critical stress could not be isolated, the net effect of using a different toner could be reasonably explained by the model.

The validity of the bond-site model is supported by a theoretical justification for the toner on paper system and the experimental results. Assuming the model to be correct, the expected segment length increases with:

- an increase in bond-spacing (distance between toner-paper bonds)
- an increase in effective thickness of the toner line
- an increase in the critical stress of the toner line
- a decrease in toner-paper bond strength
- a decrease in effective length per bond

The mean segment length varied from 100 to 400 microns. The lower limit to the segment length was given by the dry tests. The coefficient of variation (CV) was relatively constant around 54% for all the sets. This high variation is expected due to inherent variation of the fragmentation mechanism and variation of the physical system. The consistency of the CV shows that it can be used to estimate the variation of the segment length based on the mean alone.

The frequency distribution of the segment length can be fitted by a gamma curve. The distribution is skewed to shorter lengths and is bounded by zero. The gamma parameters are calculated from the mean and variance of the experimental data, rather than from simple curve fitting. This further validates that a gamma curve is a meaningful description of the data.

Printed toner was shown to have a greater segment length than model toner lines for the same effective thickness. The difference in segment length is believed to be due to the effective area per bond and the distance between bonds (bond-spacing). These differences in bonding are a result of differences in the fusing conditions to prepare the samples.

6 RESULTS AND DISCUSSION: TONER ON CELLULOSE ACETATE

6.1 Introduction

Toner on cellulose acetate was studied to provide a model system for the fragmentation of toner on paper. In this chapter, the Cox model will be shown to provide a basis for interpreting and predicting the fragmentation of toner lines on cellulose acetate when immersed in water.

A uniform polymer film was used as a substrate to simplify the analysis of fragmentation. Use of the film eliminates the roughness and structure of paper. Cellulose acetate was selected because it is cellulose and hygroscopic. A film casting technique was developed for this thesis to obtain pure cellulose acetate films with minimal residual stresses. Commercial films may contain additives and often lack dimensional stability. Cellulosic polymer films have been used to simulate paper in a number of previous studies. Both Janes (1968) and Button (1979) studied fiber-to-fiber bond strength using commercial cellophane film as a model fiber. Berger (1988) studied the effect of temperature and moisture on the ultrasonic modulus of commercial cellophane to clarify the effects of temperature and moisture on paper. In this work, the cellulose acetate is expected to simulate the hygroexpansion of paper and the resulting fragmentation of toner.

6.1.1 Theory – summary of Cox model

The fragmentation of toner on cellulose acetate will be discussed in terms of the Cox model (Sec. 3.3). This model predicts a nonlinear segment length curve.

$$L_c = \frac{4}{\beta}\tanh^{-1}\left(\beta \cdot \frac{\sigma_c}{\tau_c} \cdot h\right) \tag{3-14}$$

For this model, either adhesive or cohesive fracture may occur. The segment length is limited at the length at which adhesive fracture preferentially occurs over cohesive fracture.

6.2 Experimental – Fragmentation Tests

6.2.1 Toner on Cellulose Acetate Samples

The toner line samples were prepared the same as the toner on paper samples (Fig. 6-1). The Hewlett Packard LaserJet 4 Plus toner was used. Cellulose acetate films were cast from a solution of cellulose acetate in acetone (Sec. 4.1.1). The technique was developed for this thesis to minimize residual stress in the films. After casting, the cellulose acetate films were stored in desiccator at room temperature. The toner powder was deposited and fused on the films using the same technique as the toner on paper samples.

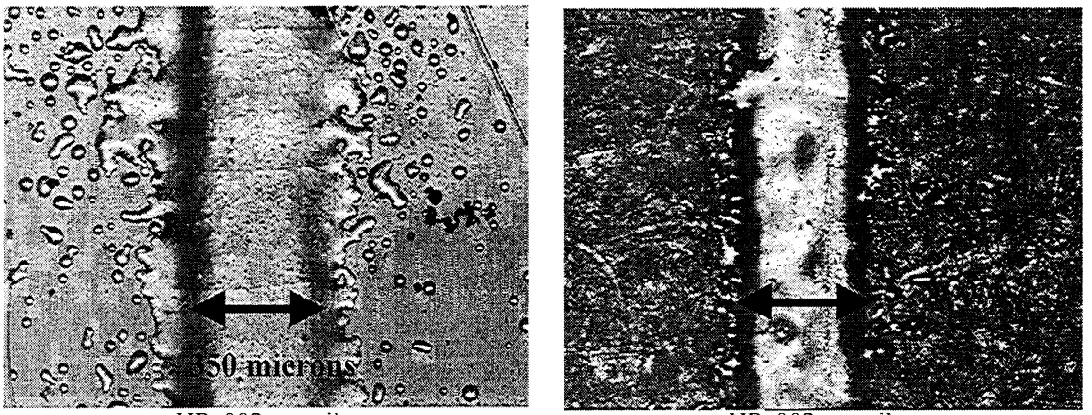

HP, 002 stencil
cellulose acetate

HP, 002 stencil
paper

Figure 6-1: Images of toner lines on cellulose acetate and paper (confocal scanning laser microscope, 10X).

6.1.1.1 Effective line thickness

The effective line thickness was calculated using the same method that was used for toner on paper (cross-sectional area divided by the width). The cellulose acetate surface was smooth and more defined than a paper surface, therefore the measurements are expected to be more accurate than for toner on paper.

6.2.2 Fragmentation Tests

The wet test is the standard test to simulate the fragmentation. Samples were individually immersed in water (nanopure deionized water, 23°C). Samples were tested 48 hours after

preparation. The segment length was measured using an identical method as that used for toner on paper. In addition, detachment was quantified by measuring the length of the line that was missing segments.

6.3 Results and Discussion – Toner on Cellulose Acetate

6.3.1 Fracture of toner lines

Fragmentation tests of toner on cellulose acetate showed both cohesive fracture of the line and adhesive fracture of the interface (Fig. 6-2). Detachment of segments from the surface shows that fracture occurs at the interface, rather than yield. Cracks form both across the width and along the length. This is expected because the cellulose acetate expands biaxially and the width of the line is greater than the critical length.

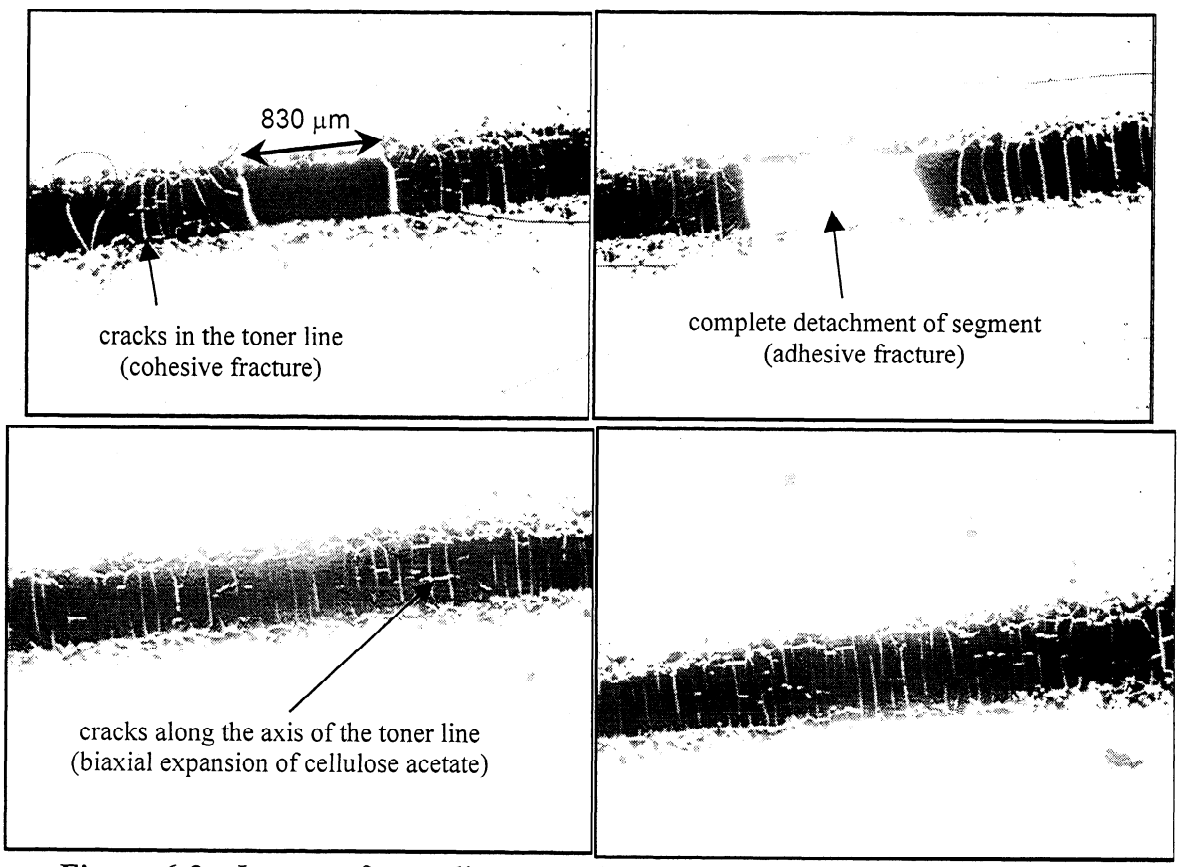

Figure 6-2: Images of toner lines on cellulose acetate after immersion in water (light microscope, 25X). The line may both cohesively and adhesively fracture. Some segments completely detached due to significant adhesive fracture.

6.3.2 Segment length curves

The results are shown with two curves, the segment length curve (Fig. 6-3) and a detachment curve (Fig. 6-4). It should be noted that on the segment length curve, the averages of the two upper points do not include the lengths of segments that completely detached. The detachment curve shows the fraction of the line that completely detached from the surface. It should be noted that this is not the total debonded length, and that other segments may be partially debonded.

The fragmentation is clearly nonlinear with thickness (Figs. 6-3, 6-4). The loss of data from the complete detachment of segments prohibits an accurate analysis of the segment length curve, however the remaining data still provide sufficient clues for interpretation. Points A and B have similar means and both have zero detachment. There is a significant jump from B to C, shown by a greater average segment length, a much greater variation, and more detachment. The differences between B and C are much more significant than between A and B, even though the change in thickness is less. Sample D further shows much greater detachment than C.

A plausible explanation is given by the Cox model. The Cox model shows three regions according to thickness (Fig. 6-5). In the middle region, the segment length is expected to follow the Cox curve. The Cox curve shows that the expected segment length is nonlinear and becomes increasingly sensitive to thickness as it approaches a critical thickness. Above the critical detachment thickness, segments detach from the substrate (see below). On the other extreme of the curve, a minimum segment size is predicted (see below). Samples within this lower range become insensitive to thickness.

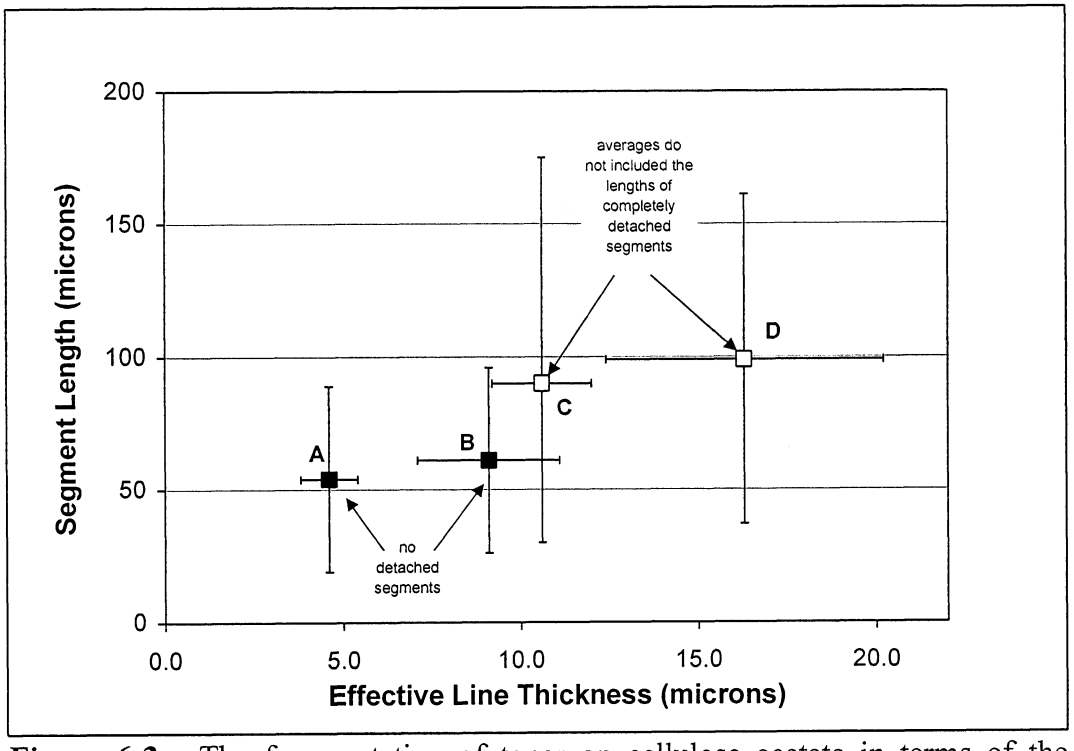

Figure 6-3: The fragmentation of toner on cellulose acetate in terms of the average segment length of segments remaining attached to the cellulose acetate. Both sample sets C and D had detachment of segments.

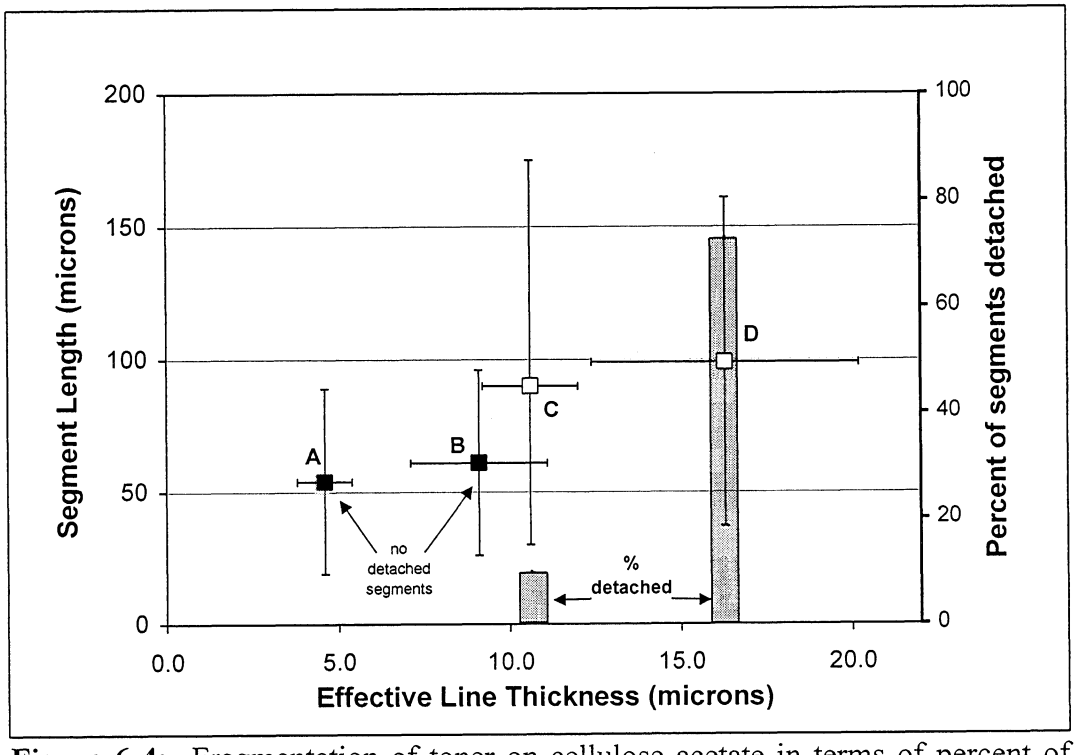

Figure 6-4: Fragmentation of toner on cellulose acetate in terms of percent of detached segments.

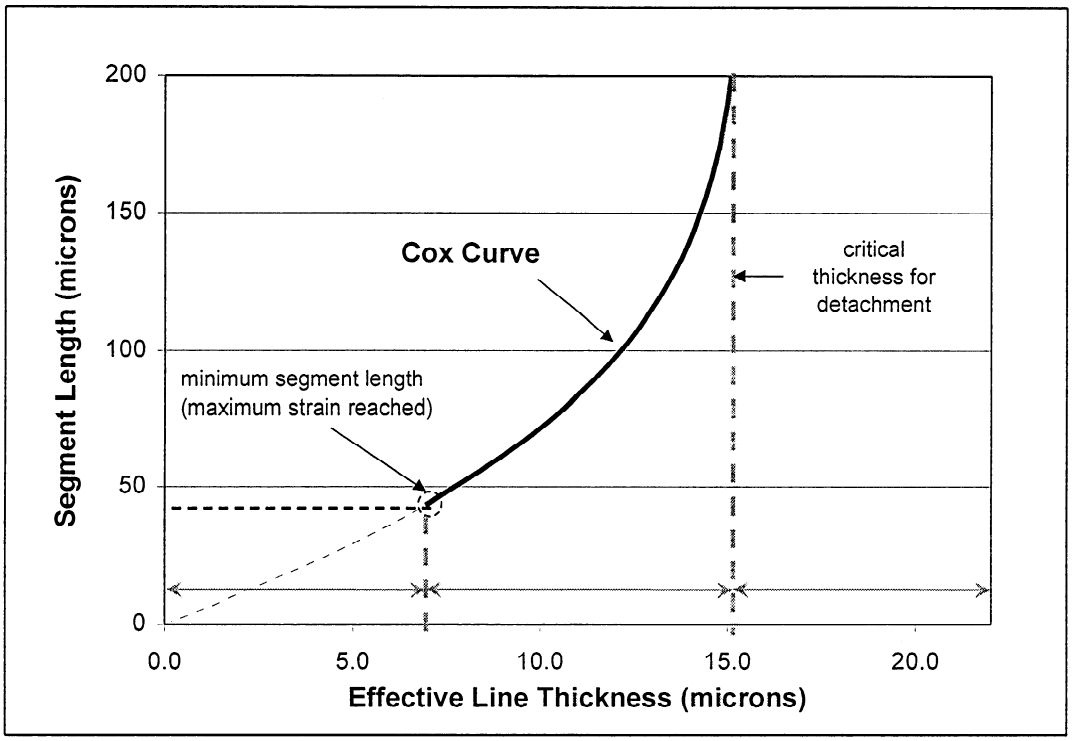

Figure 6-5: The segment length curve from the Cox model can be separated into three regions: below the minimum segment length, the actual curve, and above the critical detachment thickness.

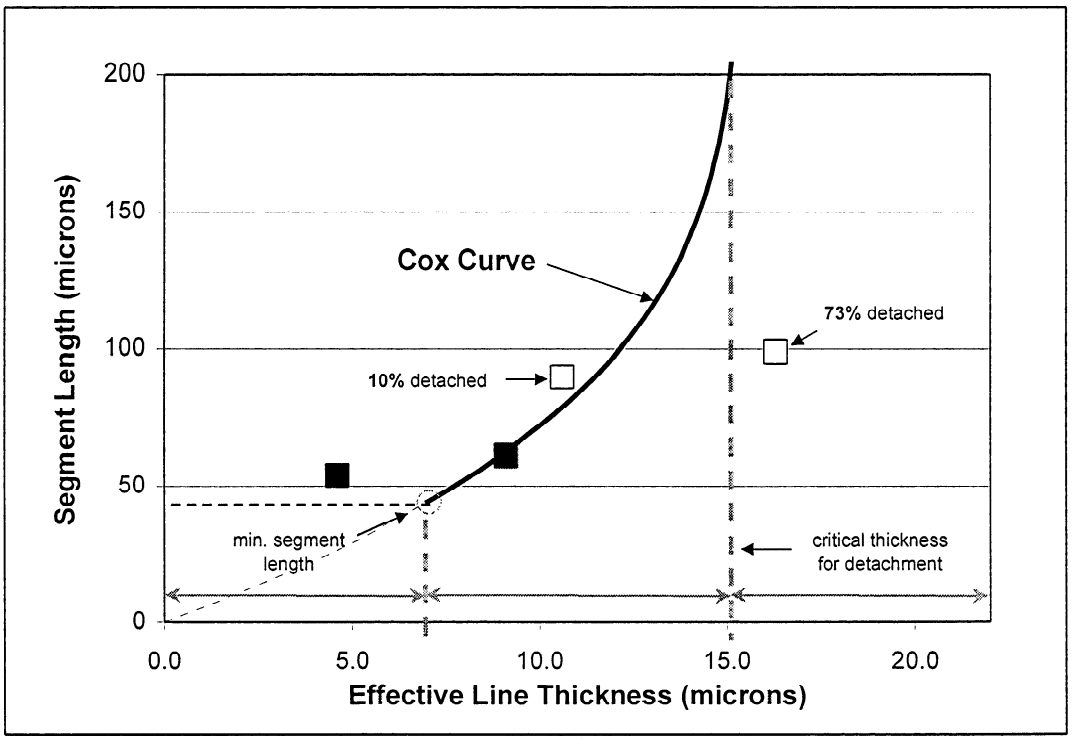

Figure 6-6: A reasonable explanation of the fragmentation data is given by the Cox model. The data points can be associated with the different regions of the curve.

Fig. 6-6 shows a reasonable fit of the data with the model. This is a qualitative fit, intended to explain the relative differences between the points. It is reasonable that points A and B are near the minimum segment length. This would explain why there is relatively small difference between these points. Point B also falls along the actual curve with point C. Point D falls outside of the Cox curve, explaining the significant detachment of segments. The entire line does not detach due to variation in thickness

6.3.3 Critical detachment thickness

Detachment of the line occurs when the line has a thickness greater than a critical thickness. Above the critical thickness, the line will adhesively fracture at all substrate strains, with no cohesive fracture. Due to variation of line thickness, lines will have sections that detach and sections that crack (Fig. 6-7). It is likely that points C and D on the segment length curve had a progressively higher fraction of the line that was above the critical thickness, hence the increase in detachment.

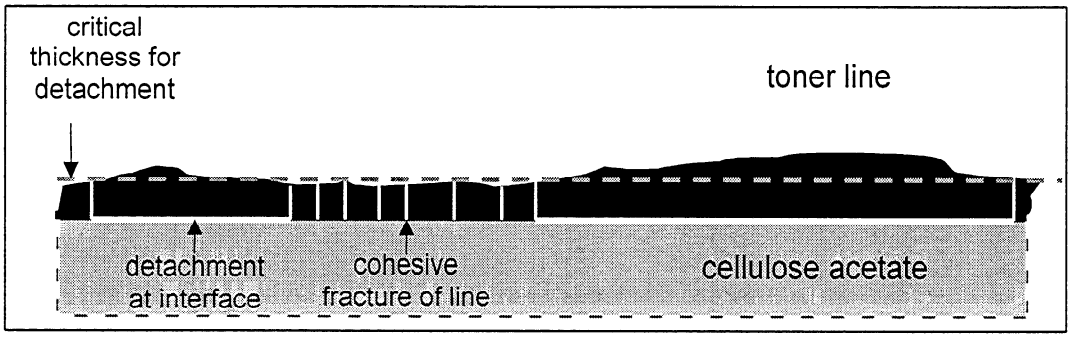

Figure 6-7: Sections of the toner line with a thickness greater than the critical thickness will preferentially detach from the substrate.

6.3.4 Minimum segment length

The minimum segment length is limited by either the critical length or the maximum strain of the substrate (Fig. 6-8). It is unlikely that the segment length will approach zero for any system because the strain to reach the critical length increases sharply as the thickness decreases. The maximum hygroexpansion of cellulose acetate likely limits the segment length of the lowest point.

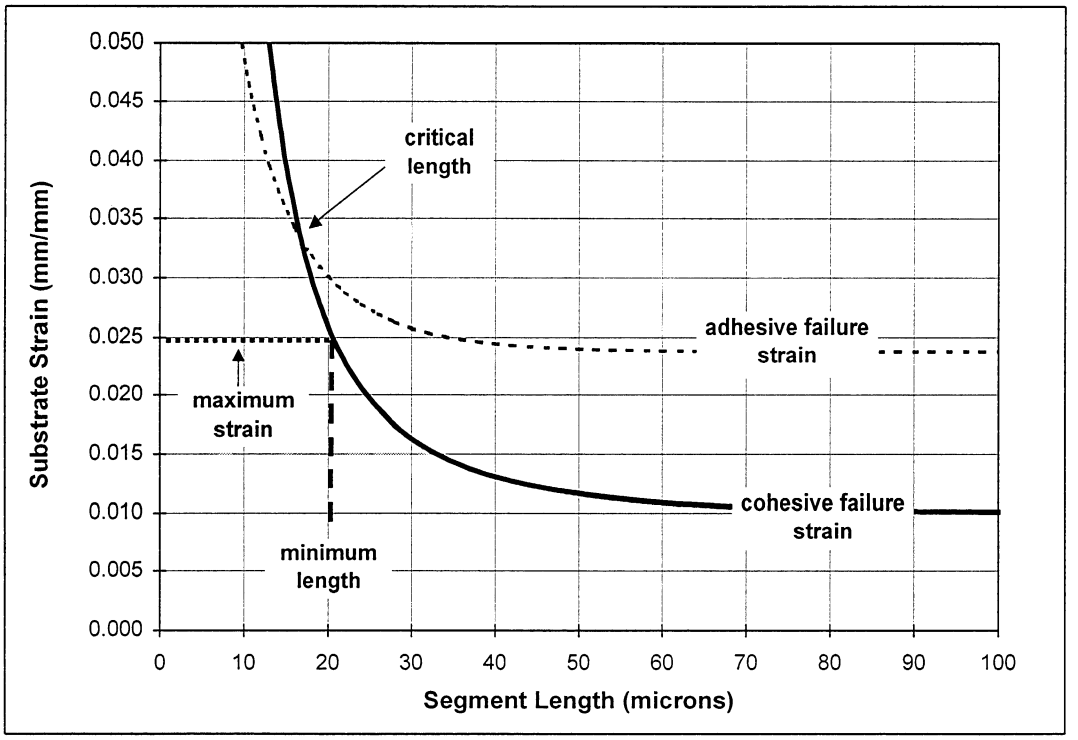

Figure 6-8: The minimum segment length may be limited by the maximum strain of the substrate, rather than the critical length.

6.4 Discussion – Comparison with Toner on Paper

The results show that cellulose acetate is not a good model substrate for simulating toner on paper. The fragmentation mechanisms are different and are controlled by significantly different properties of the substrate and interface. The fragmentation of toner on cellulose acetate is limited by interfacial fracture. The fragmentation of toner on paper is limited by yielding of the toner-paper bonds and the spacing between these bonds. These differences do not allow results to be directly transferred between the systems.

6.5 Conclusions

Toner on cellulose acetate showed fragmentation behavior that is expected for elastic materials with an interface that fractures rather than yields. This results in segment lengths that can vary greatly over small changes in thickness. The fragmentation mechanism differs from that of toner on paper, prohibiting direct transfer of results between the two systems. Thus, cellulose acetate is not a suitable model substrate for simulating the fragmentation of toner on paper.

7 CONCLUSIONS

The fragmentation of toner on paper upon immersion in water was studied to better understand the factors that influence toner particle size during deinking. An experimental technique was developed in this thesis to quantify the fragmentation. Lines of toner on paper and cellulose acetate were manually prepared to simulate printed toner on paper. These samples were immersed in water and cracks formed in the toner line due to hygroexpansion of the paper. The distance between cracks (segment length) and the effective thickness of the line were measured microscopically. The segment length curve (average segment length v. effective line thickness) was used to analyze the data. This approach allows the fragmentation to be studied in terms of the relative effects of parameters. The relative effects can be isolated from the slope and intercept of the curve.

The fragmentation of a toner line on paper can be described by the bond-site model, which was developed in this thesis. The bond-site model is a modified Kelly-Tyson stress transfer model. It includes discrete bond-sites to take into account the noncontinuous toner-paper interface. A bond-site is an idealized representation of a toner-paper bond (toner-fiber interface, fiber, adjacent fiber-fiber interfaces) in terms of the bond's mechanical shear properties and dimensions. The segment length that is expected from fragmentation is determined by a critical length. This is the length of line that is necessary for the axial stress in the line to increase to the critical stress of the line. This model can be used to interpret and predict relative changes in segment length. The expected segment length increases with:

- increasing effective thickness of the toner line
- increasing critical stress of the toner line
- increasing distance between bonds
- decreasing effective bond length
- decreasing shear strength of the bond

The average segment length of toner varied from 100 to 400 microns. The data had a coefficient of variation of around 54%. The distribution of the data could be described by a gamma curve using parameters calculated from the mean and variance of the data.

The fragmentation of a toner line on cellulose acetate can be described by the Cox model. The experimental segment length curve was nonlinear and showed increasing detachment of segments with increasing thickness. The segment length is limited by the length at which adhesive fracture preferentially occurs. In addition to being nonlinear, the expected segment length curve consists of three regions (minimum segment length, theoretical curve, and detachment thickness), making analysis of data more difficult. Cellulose acetate cannot be used as a model substrate for studying toner on paper because of the different fragmentation mechanism.

8 SUGGESTIONS FOR FUTURE WORK

Future work is proposed in two areas: toner-paper bonding and the repulping of printed lines. Work on toner-paper bonding would show whether there are opportunities to control segment size and minimize fiber attachment by manipulating the bond-strength. Work on repulping would clarify the additional fragmentation mechanisms that are occurring during repulping.

The results of this thesis showed that the segment length can vary significantly depending on the moisture content of the toner-paper bonds during expansion of the paper. This is due to a difference in the wet and dry strengths of the toner-paper bonds. However, it is unclear how much the bond-strength varies under normal deinking conditions. Ideally, the segment lengths would be closer to those produced by the dry test. This would give the best control on segment size by minimizing the average size and variance of the segments. The research would address the sensitivity of the bond-strength to process conditions:

- chemicals (*e.g.*, pH, surfactants, enzymes)
- moisture content of the paper prior to immersion in water
- physical handling of the paper

This thesis addressed the initial repulping step of immersion of the furnish in water. Additional work would investigate the effect of the other repulping mechanisms on the particle size. This thesis provides a good basis for studying the remaining mechanisms because the starting point has been defined. The research would isolate the different mechanisms that are expected such as fiber-fiber hydraulic shear forces and attrition. In conjunction, the mechanisms of disintegration of the paper sheet would be studied. The results would be used to optimize repulper design and chemical addition. Experiments would include comparing the segment length distributions of toner lines printed on paper for samples immersed in water and samples repulped at different levels of intensity.

9 ACKNOWLEDGMENTS

I would like to thank my advisor, Peter Pfromm, for his guidance and support on this project. During this time, he has helped me become a better writer, presenter, and researcher. I would also like to thank my committee members, Doug Coffin and Ted Heindel, and all the other faculty who have assisted me during my studies. Special thanks are given to Hiroki Nanko and Ted Jackson for their assistance with the laser microscope, Bob Noland for his help with design and anything else I needed, and Tom Miller for AV support. Finally, I would like to thank my family for being behind me all the way.

10 LITERATURE CITED

Agrawal, D.C. and Raj, R. (1989), "Measurement of the Ultimate Shear Strength of a Metal-Ceramic Interface" *Acta Metall.* 37(4):1265.

Bhateja, S.K. and Gilbert, J.R. (1985a), "Pressure-Fusing Behaviour of Monocomponent Toners" *J. Imaging Tech.* 11:267.

Bhateja, S.K. and Gilbert, J.R. (1985b), "Pressure-Fusing Behaviour of Monocomponent Toners at High Speeds" *J. Imaging Tech.* 11:273.

Béland, M.-C. and Mangin, P.J. (1995), "Three Dimensional Evaluation of Paper Surfaces Using Confocal Microscopy" in Surface Analysis of Paper, Conners, T.E., Banerjee, S. (Eds.), CRC Press, New York.

Bennington, C.P.J., Sui, O.S., Smith, J.D. (1998), "The Effect of Mechanical Action on Waste Paper Defibering and Ink Removal in Repulping Operations" *J. Pulp Paper Sci.* 24(11):341.

Berg, S.R., Johnson, D.A., Thompson, E.V. (1997), "Toner Detachment During Repulping of Laser-Printed Office Copy Paper" *Tappi J.* 80(4):171.

Berger, B.J. (1988), *The Influence of Temperature, Test Frequency, and Moisture Sorption on the Viscoelastic Moduli of Cellulose* Ph.D. Dissertation, Institute of Paper Chemistry.

Borch, J. (1992), "Effect of Paper Chemistry in Electrophotography" in Colloids and Surfaces in Reprographic Technology, ACS Symposium Series 200, Hair, M., Croucher, M.D. (Eds.), American Chemical Society, Washington, D.C.

Borchardt, J.K. and Rask, J.H. (1993), "Macro- and Microscopic Deinking Studies of Electrostatic-Ink Containing Furnishes" *Proc. TAPPI 1993 Pulping Conf.*, Atlanta, GA, p. 839.

Borchardt, J.K., Matalamaki, D.W., Lott, V.G., Rask, J.H. (1994), "Deinking Toner Ink Containing Furnishes. Part 2. Deinking with Mechanical Cleaners" *Prog. Paper Recycling* 4(1):44.

Button, A.F. (1979), *Fiber-Fiber Bond Strength: A Study of a Linear Elastic Model Structure* Ph.D. Dissertation, Institute of Paper Chemistry.

Cathie, K. and Burdett, S. (1992), "Understanding Why Laser Printed Papers Deink Differently" *Proc. TAPPI 1992 Pulping Conf.*, Boston, MA, p. 619.

Cathie, K. and Mallouris, M. (1993), "Use of Surface Energy Measurements and other Parameters to Predict the Deinkability of Laser Printed Papers" *CPPA 2nd Research Forum on Recycling*, Ste. Adele, Quebec, p.179.

Cleveland, F.C. (1993), "Pulping of Secondary Fiber" in Secondary Fiber Recycling, Spangenberg, R.J. (Ed.), TAPPI Press, Atlanta, GA.

Cox, H.L. (1952), "The Elasticity and Strength of Paper and Other Fibrous Materials" *British J. Applied Physics* 3:72.

Daoust, T., Vu-Khanh, T., Ahlstrom, C., Gérard, J.F. (1993), "A Finite Element Model of the Fragmentation Test for the Case of a Coated Fiber" *Comp. Sci. Tech.*, 48:143.

Dorris, G.M. and Sayegh, N.N. (1997), "The Role of Print Layer Thickness and Cohesiveness on Deinking of Toner-Printed Papers" *Tappi J.* 80(4):181.

Epstein, B. (1947), "The Mathematical Description of Certain Breakage Mechanisms Leading to the Logarithmico-Normal Distribution" *J. Franklin Inst.* 244:471.

Fallows, J.D. (1992), "Pulper & Pulper Screens" *TAPPI 1992 Deinking Seminar Notes*, TAPPI Press, Atlanta, session 2-1.

Feillard, P., Désarmot, G., Favre, J.P. (1994), "Theoretical Aspects of the Fragmentation Test" *Comp. Sci. Tech.* 50:265.

Forgo, G., Ragnetti, M., Stübbe, A. (1993), "Styrene-Acrylate Copolymers as Toner Resins: Correlations Between Molecular Structure, Viscoelastic Behavior, and Fusing Properties" *J. Imaging Sci. Tech.* 37(2):176.

Fu, T.Z., Durning, C.J., Tong, H.M. (1991), "Simple Model for Swelling-Induced Stresses in a Supported Polymer Thin Film" *J. Appl. Polym. Sci.* 43:709.

Gates, D.J. and Westcott, M. (1996), "A Stochastic Line Model for Paper Stiffness" *Appita*, 49(3):189.

Gibson, R.F. (1994), Principles of Composite Material Mechanics, McGraw-Hill, Inc., New York.

Gruber, R.J. and Julien, P.C (1991), "Dry Toner Technology" in Handbook of Imaging Materials, Diamond, A.S. (Ed.), Marcel Dekker, Inc., New York.

Hahn, G.J. and Shapiro, S.S. (1967), Statistical Models in Engineering, John Wiley & Sons, Inc., New York.

Herdan, G. and Smith, M.L. (1953), Small Particle Statistics, Elsevier Publishing Co. Ltd., New York.

Holister, G.S. and Thomas, C. (1966), Fiber Reinforced Materials, Elsevier Publishing Co. Ltd., New York.

Hu, M.S. and Evans, A.G. (1989), "The Cracking and Decohesion of Thin Films on Ductile Substrates" *Acta Metall.* 37(3):917.

Janes, R.L. (1968), *A Study of Adhesion in the Cellulose-Starch-Cellulose System* Ph.D. Dissertation, Institute of Paper Chemistry.

Johnson, D.A. and Thompson, E.V. (1994), "Fiber/Toner Detachment Studies: Repulping and Flotation of Laser Printed Paper. Part 1" *Proc. TAPPI 1994 Pulping Conf.*, San Diego, CA, p. 1291.

Jou, J.-H., Hsu, L., Huang, P.-T., Huang, R., Shen, W.-P. (1991), "Bending Beam Measurement of Moisture Diffusion in Polyimide Films on Silicon Substrate" *Polymer J.* 23(9):1123.

Jou, J.-H. and Hsu, L. (1992), "Bending-Beam Measurement of Solvent Diffusion in Polyimides: Theoretical and Experimental" *J. Appl. Polym. Sci.* 44:191.

Jou, J.-H., Yang, A.-K., Chang, Y.-L., Jou, J.-M. (1995), "General Formula for Bending Beam Determination of Case II Diffusion in Polymer-Containing Bilayer Structures" *J. Appl. Polym. Sci.* 55:1517.

Kakogiannos, A., Johnson, D.A., Thompson, E.V. (1997), "Laboratory High Consistency Dispersion Studies of Laser Printed Office Copy Paper. Part II" *Proc. TAPPI 1997 Recycling Symp.*, Chicago, IL, p. 53.

Kelly, A. and Tyson, W.R. (1965a), "Fiber-Strengthened Materials" in High Strength Materials, Zackay, V.F. (Ed.), Wiley, New York, pp. 578-602.

Kelly, A. and Tyson, W.R. (1965b), "Tensile Properties of Fibre-Reinforced Metals: Copper/Tungsten and Copper/Molybdenum" *J. Mech. Phys. Solids* 13:329.

Kelly, A. (1973), Strong Solids, 2nd ed., Clarendon Press, Oxford.

Kim, J.-K., Zhou, L., Mai, Y.-W. (1993), "Stress Transfer in the Fiber Fragmentation Test. Part 1. An Improved Analysis Based on a Shear Strength Criterion" *J. Mat. Sci.* 28:6233.

Kolseth, P. and Ehrnrooth, E.M.L. (1986), "Mechanical Softening of Single Wood Pulp Fibers" in Paper Structure and Properties, Bristow, J.A., Kolseth, P. (Eds.), Marcel Dekker, Inc., New York.

Kubát, J., Nyborg, L., Steenberg, B. (1963), "Response of Paper to Low Frequency Sinusoidal Strain" *Svensk Papperstidning* 66(19):754.

Lee, L.-H. (1975), "Thermal Fixing of Electrophotographic Images" in Adhesion Science and Technology, Polymer Science and Technology volume 9B, Lee, L.-H. (Ed.), p. 831.

Ling, S. and Wagner, H.D. (1993), "Relationship Between Fiber Flaw Spectra and the Fragmentation Process: A Computer Simulation Investigation" *Composites Sci. Tech.* 48:35.

Melantis, N., Galiotis, C., Tetlow, P.L., Davies, C.K.L. (1992), "Interfacial Shear Stress Distribution in Model Composites Part 2: Fragmentation Studies on Carbon Fibre/Epoxy Systems" *J. Comp. Mat.* 26(4):574.

Miwa, M., Ohsawa, T., Tahara, K. (1980), "Effects of Fiber Length on the Tensile Strength of Epoxy/Glass Fiber and Polyester/Glass Fiber Composites" *J. Appl. Polym. Sci.* 25:795.

Morsink, J.B.W. and Daane, G.J.R. (1992), "Surfactant-Aided Detachment of Ink from Impact- and Non-Impact-Printed Paper" *Proc. TAPPI 1992 Pulping Conf.*, Boston, MA, p. 963.

Mort, J. (1989), The Anatomy of Xerography, Its Invention and Evolution, McFarland & Co., Inc. Publishers, Jefferson, NC.

Nanko, H. (1998), personal communication.

Narkis, M., Chen, E.J.H., Pipes, R.B. (1988), "Review of Methods for Characterization of Interfacial Fiber-Matrix Interactions" *Polymer Composites* 9(4):245.

Niskanen, K. (1998), "Rheology and Moisture Effects" in Paper Physics, Book 16 of the Papermaking Science and Technology series, Niskanen, K. (Ed.), Fapet Oy, Helsinki, Finland.

Ohsawa, T., Nakayama, A., Miwa, M., Hasegawa, A. (1978), "Temperature Dependence of Critical Fiber Length for Glass Fiber-Reinforced Thermosetting Resins" *J. Appl. Polym. Sci.* 22:3203.

Page, D.H. and Seth, R.S. (1980), "The Elastic Modulus of Paper II. The Importance of Fiber Modulus, Bonding, and Fiber Length" *Tappi J.* 63(6):113.

Perkins, R.W. (1980), "Mechanical Behavior of Paper in Relation to its Structure" *Proc. Conf. Paper Science and Technology: The Cutting Edge*, Institute of Paper Chemistry, Appleton, WI, p. 89.

Piggott, M.R. (1980), Load-Bearing Fibre Composites, Pergamon Press, New York.

Piggott, M.R. (1994), "Short Fibre Polymer Composites: a Fracture-Based Theory of Fibre Reinforcement" *J. Comp. Mat.* 28(7):588.

Prime, R.B. (1983), "Relationships Between Toner Properties, Fuser Parameters, and Fixing of Electrophotographic Images" *Photographic Sci. Eng.* 27:19.

Rosen, B.W. (1965), "Mechanics of Composite Strengthening" in Fiber Composite Materials, American Society for Metals, Metals Park, Ohio, pp. 37-75.

Sakurai, S., Tanaka, K., Nomura, S. (1993), "Two-Dimensional Undulation Pattern on Free Surface of Polymer Film Cast from Solution" *Polymer* 34(5):1089.

Shallhorn, P.M. and Karnis, A. (1979), The Tear and Tensile Strength of Mechanical Pulps" *Proc. CPPA and TAPPI 1979 International Mechanical Pulping Conf.*, Toronto, Ont., p.25.

Snyder, B.A. and Berg, J.C. (1994), "Effect of Particle Size and Density in Flotation Deinking of Electrostatic Papers" *Tappi J.* 77(7):157.

Standard ASTM D 638 – 97. *Standard test method for tensile properties of plastics.*

Standard ISO 4287/1-1984. *Surface roughness – terminology – Part 1: Surface and its parameters.*

Standard TAPPI T 205 om-88. *Forming handsheets for physical tests of pulp.*

Tripathi, D. and Jones, F.R. (1998), "Single Fibre Fragmentation Test for Assessing Adhesion in Fibre Reinforced Composites" *J. Material Sci.* 33:1.

Vander Wielen, L.C. (1997), *Effect of Temperature and pH on Toner Fracture Due to Paper Swelling*, A190 Independent Study Project, Institute of Paper Science and Technology.

Vander Wielen, L.C., Panek, J.C., Pfromm, P.H. (1999), "Fracture of Toner Due to Paper Swelling" *Tappi J.*, accepted for publication.

Vidotti, R.M., Johnson, D.A., Thompson, E.V. (1994), "Repulping and Flotation Studies of Photocopied and Laser-Printed Office Paper. Part I. Repulping and Image Analysis" *Prog. Paper Recycling* 2(4):39.

Vidotti, R.M., Johnson, D.A., Thompson, E.V. (1994), "Repulping and Flotation Studies of Photocopied and Laser-Printed Office Paper. Part II. Flotation" *Prog. Paper Recycling* 3(3):39.

Walpole, R.E. and Myers, R.H. (1989), Probability and Statistics for Engineers and Scientists, 4th ed., Macmillan Publishing Co., New York.

Wojciechowski, P.H. and Mendolia, M.S. (1989), "On the Multiple Fracture of Low-Elongation Thin Films Deposited on High-Elongation Substrates" *J. Vac. Sci. Technol. A* 7(3):1282.

Yan, N. and Kortsschot, M. (1996), "Modelling of Out-of-Plane Tear Energy Absorption of Paper" *Appita* 49(3):176.

APPENDIX I: Bending Beam Tests

I.1 Introduction

This section discusses the work that was done to model and experimentally measure the deflection of a bi-layer laminate. The purpose of the work was to determine the stresses that develop in a toner-cellulose acetate laminate due to swelling of the cellulose acetate during immersion in water. The work with toner-cellulose acetate laminates was not completed due to difficulties in preparing samples. Only the results with steel-cellulose acetate laminates will be presented here. A model for describing the deflection and the experimental apparatus for measuring the deflection will be presented.

I.2 Background and Theory

A theoretical model to describe the bending of the cellulose acetate / steel laminate upon immersion in water will be presented. The model identifies the important material properties and determines the distribution of stresses and strains through the materials. The stresses and strains may be used to quantify fracture. The model consists of a combination of solid mechanics and mass transfer. Mechanics determine the degree of deflection of the laminate that results from hygroexpansion. The degree of hygroexpansion depends on the moisture concentration in the laminate at a given time, which is determined by mass transfer. Important parameters are the stiffnesses of the materials, dimensions, coefficient of hygroexpansion, diffusion coefficient, and initial and equilibrium moisture contents.

I.2.1 Literature review

Review of the literature shows that models of the deflection of a polymer/substrate strip as a function of time have been previously presented. In these models, the deflection is the result of swelling of the polymer due to the diffusion of a penetrant into the polymer. Jou *et al.* (1991)

modeled the deflection under normal Fickian diffusion, while Fu *et al.* (1991), Jou and Hsu (1992), and Jou *et al.* (1995) modeled deflection under case II diffusion.

Jou *et al.* (1991) took a very similar approach to that described here. The polymer film is divided into a number of sublayers (N); each sublayer swells according to concentration of penetrant. The concentration in each layer is determined by the Fickian diffusion model and the degree of swelling is assumed to be a linear function of concentration. The deflection of the laminate is determined by a force balance in each of the N layers, a strain balance at the interface between the layers, and a moment balance. This produces a relationship between bending curvature at time *t* and thicknesses, moduli, swelling coefficient, and concentrations at time *t*. Jou *et al.* further defined a dimensionless bending curvature ratio, Ω, in order to include Fickian diffusion model.

$$\Omega = \frac{1/\rho_t - 1/\rho_0}{1/\rho_\infty - 1/\rho_0} \tag{AI–1}$$

where: ρ_t: radius of curvature at time t [mm]
ρ_0: initial radius of curvature [mm]
ρ_∞: final radius of curvature [mm]

Manipulation of equations and simplifying assumptions produce a relationship that is dependent on thickness and diffusion coefficient only.

$$\Omega = 2\left(1+\frac{K}{2}\right)\left(\frac{Dt}{d_f^2}\right)^{1/2}\left(\pi^{-1/2}\right) \tag{AI-2}$$

$$K = \frac{2}{\left(1+\frac{d_f}{d_1}\right)}\left(1+\frac{d_f}{d_1}\frac{E_1^*}{E_f^*}\right) \tag{AI-3}$$

$$K \approx \frac{2d_1}{(d_1+d_f)} \quad \text{for } d_f < d_1$$

where D: diffusion coefficient [cm^2/s]
t: time [sec.]
d_f: film thickness [cm]
d_l: substrate thickness [cm]
E^*_f: film biaxial modulus [GPa]
E^*_l: substrate biaxial modulus [GPa]

This model is characterized by a linear plot of Ω v. $t^{1/2}$ in the initial diffusion stage. The diffusion coefficient can be calculated from the slope of this plot. Jou *et al.* (1991) produced linear plots of experimental bending data, from which they obtained diffusion coefficients. However, these diffusion coefficients were not compared with independently determined coefficients (such as by a gravimetric technique). Thus, they did not show the validity of the diffusion coefficients determined from this approach. The model was shown to fit the data with an adjustable parameter; it was not shown that the model can fit the data using a Fickian diffusion coefficient.

The other bending beam models consist of deflection under case II diffusion (Fu *et al.* (1991), Jou and Hsu (1992), and Jou *et al.* (1995)). In case II, diffusion of penetrant into the polymer is characterized by a sharp penetration front, instead of a more gradual change in concentration. The front moves through at constant velocity and rather distinctly divides the polymer into two regions: low penetrant concentration and high penetrant concentration. The high concentration region is swollen with penetrant.

In the case of a polymer laminated to an inert substrate, penetrant will diffuse in from one side only, producing a "trilayer" beam: swollen polymer, unswollen polymer, and the substrate. The thickness of the swollen layer increases linearly with time, while the thickness of the unswollen layer correspondingly decreases. The rate of diffusion, thus the change in thicknesses, is characterized by a penetration velocity, v. The deflection of the beam is determined by force and moment balances based on the degree of swelling of the swollen layer and the thicknesses of

the layers at time t. This model is characterized by a linear plot of Ω v time; deflection is linear with time.

I.2.2 Classic Lamination Model

This model developed for this work is based on the classical lamination model conventionally used for laminated composites (*e.g.,* Gibson, 1994) and is similar to the model by Jou *et al.* (1991). This model assumes a state of plane stress in each layer and neglects interlaminar stresses. In this case, the polymer film is hypothetically divided through the thickness into layers of finite thickness as shown in Fig. AI-1. Thus, this system becomes a multi-layered laminate. Based on the stiffnesses and hygroexpansion of each layer, the stresses and strains in each layer and the curvature of the laminate can be determined.

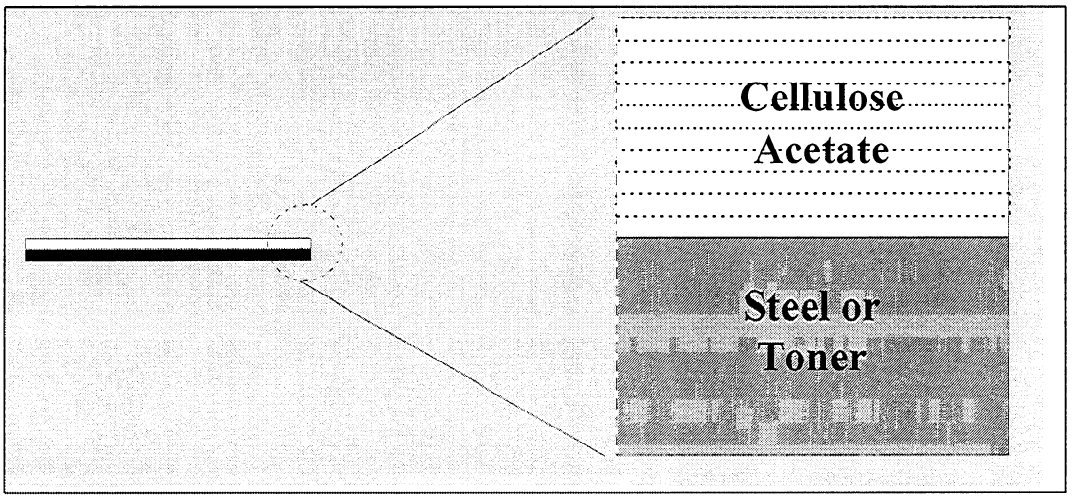

Figure AI-1: Schematic diagram of toner (or steel)/cellulose acetate laminate. For modeling, the cellulose acetate is hypothetically divided into layers.

The equations to be used for this model are as follows:

- stress and strain in layer *k*:

$$\{\sigma\}_k = [\overline{Q}]_k \left(\{\varepsilon\}_k - \{\beta\}_k c_k \right) \tag{AI-4}$$

$$\{\varepsilon\}_k = \{\varepsilon^\circ\} + z\{\kappa\} \tag{AI-5}$$

$$\{\sigma\}_k = [\overline{Q}]_k \left(\{\varepsilon^\circ\} + z\{\kappa\} - \{\beta\}_k c_k \right) \tag{AI-6}$$

where:

$$\{\sigma\}_k \equiv \begin{Bmatrix} \sigma_x \\ \sigma_y \\ \tau_{xy} \end{Bmatrix}, \quad \{\varepsilon\}_k \equiv \begin{Bmatrix} \varepsilon_x \\ \varepsilon_y \\ \gamma_{xy} \end{Bmatrix}, \quad \{\beta\}_k \equiv \begin{Bmatrix} \beta_x \\ \beta_y \\ 0 \end{Bmatrix}, \quad \{\kappa\}_k \equiv \begin{Bmatrix} \kappa_x \\ \kappa_y \\ \kappa_{xy} \end{Bmatrix}, \quad [\overline{Q}]_k \equiv \begin{bmatrix} Q_{11} & Q_{12} & Q_{16} \\ Q_{21} & Q_{22} & Q_{26} \\ Q_{61} & Q_{62} & Q_{66} \end{bmatrix} \tag{AI-7}$$

σ: stress (MPa)
Q: stiffnesses (MPa)
ε: strain (mm/mm)
β: hygroexpansion coefficient (mm)
c: moisture content (g/g)
ε°: strain at midplane (mm/mm)
z: distance from midplane (mm)
κ: curvature (mm^{-1})

- resultant laminate forces and moments:

$$\{N^E\} = \{N\} + \{N^T\} + \{N^M\}, \quad \{M^E\} = \{M\} + \{M^T\} + \{M^M\} \tag{AI-8}$$

$$\{N^M\} = \sum_{k=1}^{N} [\overline{Q}]_k \{\beta\}_k (z_k - z_{k-1}) c_k \tag{AI-9}$$

$$\{M^M\} = \frac{1}{2} \sum_{k=1}^{N} [\overline{Q}]_k \{\beta\}_k (z_k^2 - z_{k-1}^2) c_k \tag{AI-10}$$

N^E: total effective force (MPa)
M^M: total effective moment (MPa)
N: laminate force due to mechanical loading (MPa); 0 in this case
M: laminate moment due to mechanical loading (MPa); 0 in this case
N^T: laminate force due to temperature change (MPa); 0 in this case
M^T: laminate moment due to temperature change (MPa); 0 in this case
N^M: laminate force due to moisture (MPa)
M^M: laminate moment due to moisture(MPa)

- midplane strain and curvature

$$\begin{Bmatrix} \varepsilon^\circ \\ \cdots \\ \kappa \end{Bmatrix} = \begin{bmatrix} A' & \vdots & B' \\ \cdots & & \cdots \\ B' & \vdots & D' \end{bmatrix} \begin{Bmatrix} N^E \\ \cdots \\ M^E \end{Bmatrix} \tag{AI-11}$$

where:

$$\begin{bmatrix} A' & \vdots & B' \\ \cdots & & \cdots \\ B' & \vdots & D' \end{bmatrix} = \begin{bmatrix} A & \vdots & B \\ \cdots & & \cdots \\ B & \vdots & D \end{bmatrix}^{-1} \Rightarrow 6x6\ matrix \tag{AI-12}$$

$$A_{ij} = \sum_{k=1}^{N} \left[\overline{Q}_{ij}\right]_k \left(z_k - z_{k-1}\right) \tag{AI-13}$$

$$B_{ij} = \frac{1}{2}\sum_{k=1}^{N} \left[\overline{Q}_{ij}\right]_k \left(z_k^2 - z_{k-1}^2\right) \tag{AI-14}$$

$$D_{ij} = \frac{1}{3}\sum_{k=1}^{N} \left[\overline{Q}_{ij}\right]_k \left(z_k^3 - z_{k-1}^3\right) \tag{AI-15}$$

where:
A: extensional stiffness matrix
B: bending stiffness matrix
D: coupling stiffness matrix

Parameters:
The parameters that must be experimentally determined to use this model are:

- stiffnesses - may be moisture dependent
- hygroexpansion coefficient - model assumes a linear relationship between expansion and moisture content
- thickness
- moisture content - may be possible to predict based on Fickian diffusion, thus need diffusion coefficient

Calculation Procedure:

- determine the moisture content in each layer at time *t* based on Fickian diffusion
- determine the stiffness coefficients based on moisture content
- calculate N^M and M^M (Eq. 9 & 10)
- calculate ε° and κ (Eq. 11)
- calculate stress and strain in each layer (Eq. 5 & 6)

The curvature of the laminate and the stresses and strains at the top and bottom of each layer are calculated at time *t*. The theoretical deflection of a laminate with time for a 100 micron film of cellulose acetate laminated to a 100 micron steel beam is shown in Fig. AI-7 with the experimental results.

I.3 Experimental Methods and Materials

I.3.1 Preparation of cellulose acetate / steel laminates

Cellulose acetate on steel laminates were prepared by gluing a strip of cellulose acetate to a steel thickness gage. Preparation of cellulose acetate films was described in Sec. 4.1.1. The film preparation technique was developed to produce a film that was flat and dimensionally stable. Dimensionally stable means that the film remains flat when immersed in water. This is important so that the deflection of the laminate is a result of only the difference in mechanical properties between the two layers.

The key technique for lamination was to effectively adhere the cellulose acetate to the steel beam. There should be no delamination when the laminate is placed in water. A number of adhesives were investigated: epoxy: Miller Stephenson #907, 3M #2216; cyanoacrylate: "Krazy Glue", Loctite #414; spray adhesive: 3M Super 77; plastic adhesive: 3M #826. The best adhesive was the 3M #826, as it did not delaminate over an extended period of time in water. The use of the remainder of the adhesives resulted in delamination.

Another major challenge was to prepare laminates that were free of twisting and non-uniform bending when immersed in water. Circular curvature and absence of twisting is necessary for analysis. It was believed that the non-uniform bending arose due to the multi-axial swelling of the cellulose acetate film. This leads to bending of the laminate in both the length and width. Bending across the width leads to increased bending stiffness along the length, thus distorts uniform bending along the length. To reduce bending across the width, four methods were proposed: increase the thickness of the steel beam to reduce bending in both directions; orient the cellulose acetate film so that it will expand primarily along the length; clamp both ends of the laminate to prevent curling across the width; increase the stiffness of the steel beam across the width by attaching supports. Experiments showed that use of a thicker steel beam

minimized non-uniform bending. Laminates prepared with 102 and 152 micron steel beams showed no detectable twist and produced circular curvature. In addition, there was enough deflection to be experimentally significant. Laminates prepared with 76 microns beams showed appreciable twisting.

I.3.2 Deflection measurements

This work involves recording the deflection of the tip of the laminate with time. Deflection is determined based on the length of a line drawn between the tip of the laminate and a reference line (Fig. AI-2).

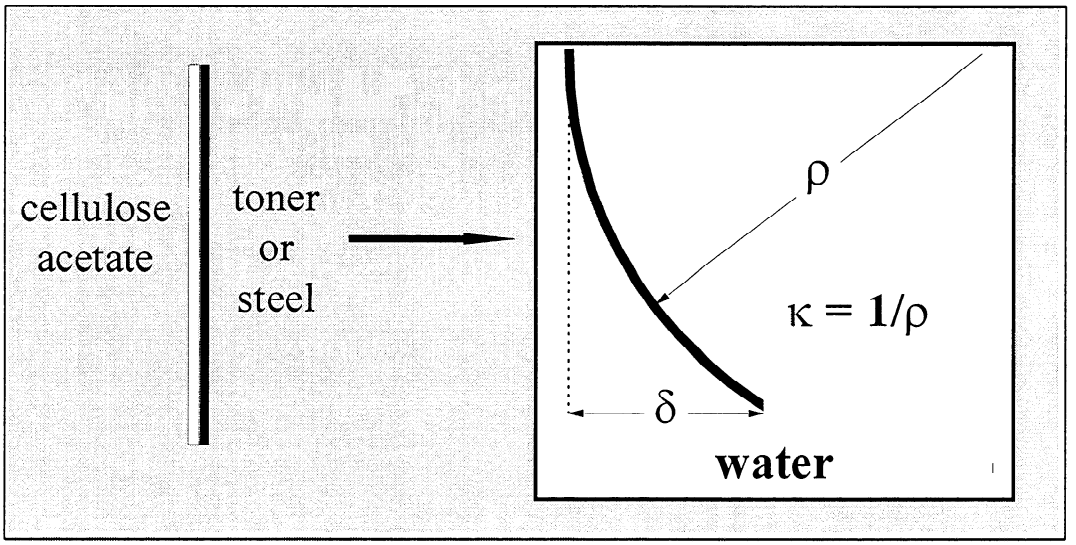

Figure AI-2: The laminate is immersed in water and the deflection, δ, is measured.

The experimental set-up for recording deflection is shown in Fig. AI-3. The laminate is fixed in a clamp, then positioned in a view-box. A metal rod is being used for the reference line and a ball bearing is used for calibration (Fig. AI-4). The reference line gives a common line to measure the deflection (Fig. AI-5), while the calibration ball provides an accurate calibration for image analysis. Previously, a grid was used for both these purposes, however this new set-up has its advantages. The rod and ball produce sharper images on the monitor than the grid, and can be mounted reproducibly and accurately in the same plane as the front of the laminate. This

is important, as a measurement made with the calibration ball significantly out-of-plane would be erroneous. The ball has the same dimension across its diameter, no matter what angle it is viewed at. The ball is a 10 mm chrome steel ball used for bearings (0.000025" sphericity, 0.0001" diameter deviation).

The deflection of the laminate was recording on a video tape. The view-box was positioned on a baseplate with a camera as shown in Fig. AI-6. Use of the baseplate assures that the laminate is consistently aligned with the camera. Digital images from the videotape were analyzed using image analysis software (OPTIMAS 5.2, Optimas Corp., Bothell, WA). The primary use of the software was to determine the line length between two points for a line "drawn" on an image monitor. The line length will depend on the calibration of the image on the monitor. The recorded tape is replayed on an image monitor connected with Optimas. The image on the image monitor can be "frozen" at any frame. Once the image is frozen, points and lines can be drawn on the image using Optimas software. Optimas can then extract the coordinates of the points and lengths of the lines and export this data either to the screen or to an Excel worksheet.

I.3.3 Analysis of deflection

The deflection at time t, δ_t, is calculated by subtracting the line length of the initial image, l_0 (t=0), from the line length in a subsequent image, l_t (t=t). Deflection at different points in time is obtained from lines in separate images. The time of each image is recorded on the screen from the videotape. The relative time of the experiment, t, is determined by subtracting the time on the initial screen, s_0, from the time on subsequent screens, s_t.

$$\delta_t = l_t - l_0$$
$$t = s_t - s_0$$

The data is reduced to curvature v. time. Plotting data as curvature normalizes the deflection to the length of the beam.

$$\kappa = \frac{1}{\rho} = \frac{2\delta}{L^2}$$

where: κ: curvature [mm^{-1}]
ρ: radius of curvature [mm]
δ: deflection [mm]
L: length of laminate (unclamped) [mm]

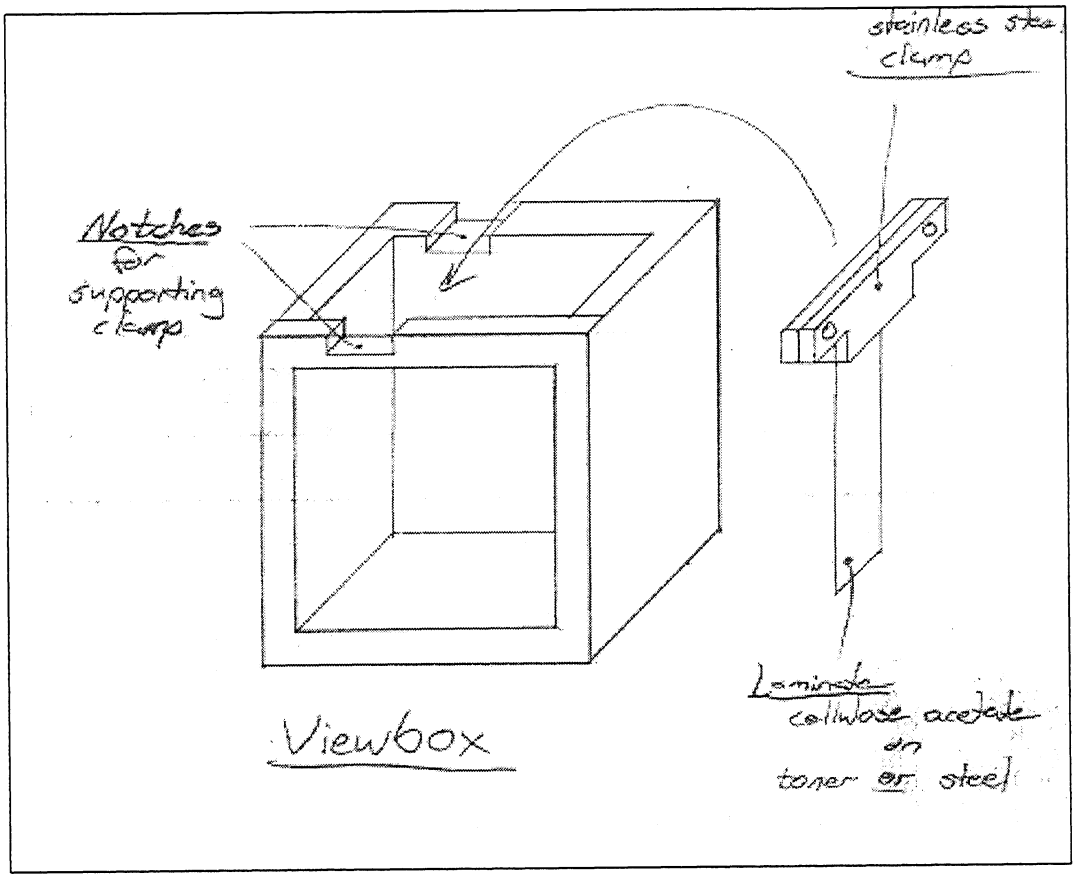

Figure AI-3: Schematic diagram of viewbox. The laminate is clamped and positioned in the viewbox, then water is added to the viewbox.

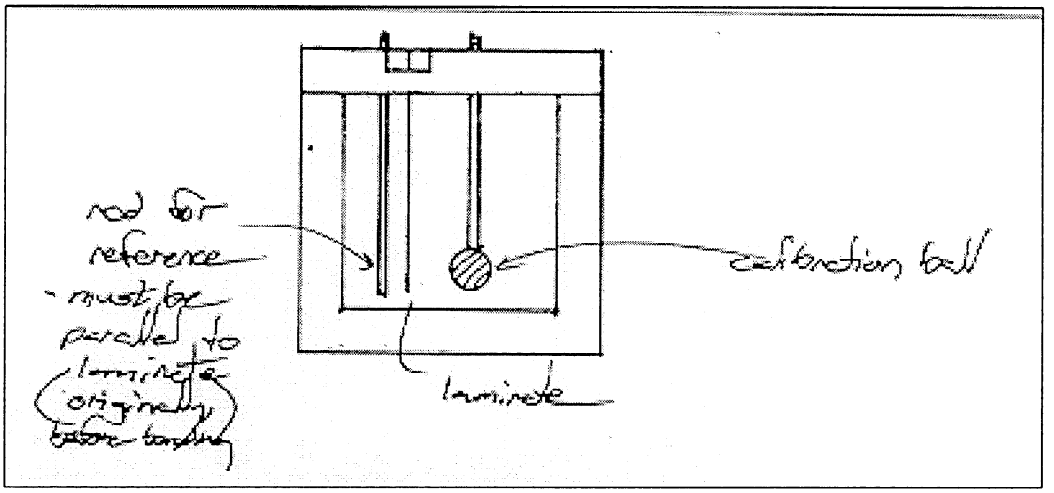

Figure AI-4: Front of the viewbox. The calibration ball is used to calibrate the image analysis software. The reference rod is used to measure the deflection.

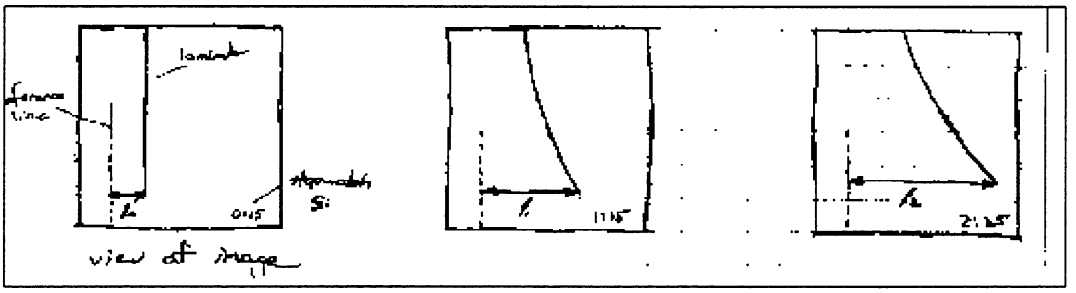

Figure AI-5: The deflection is measured with the distance between the tip of the laminate and the reference line.

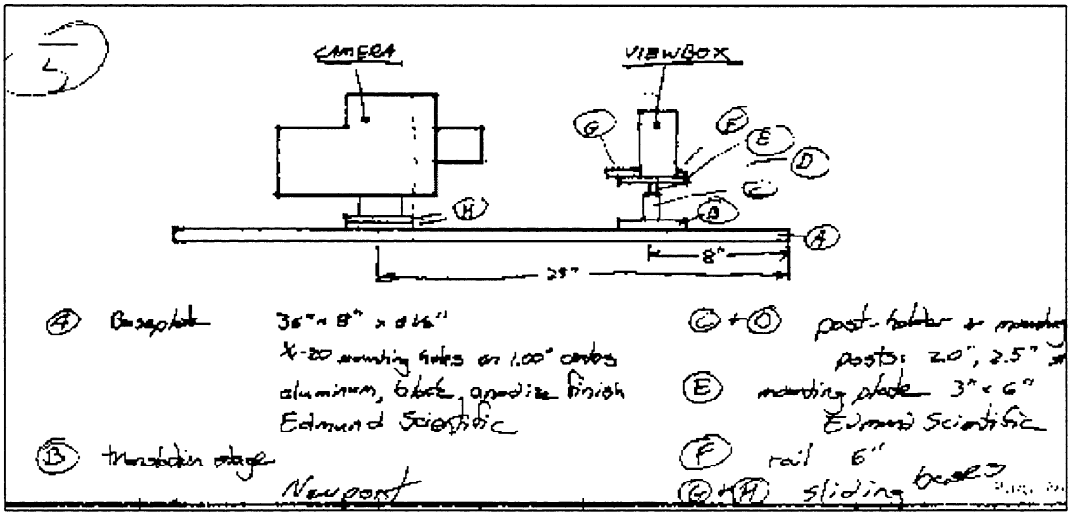

Figure AI-6: The viewbox is mounted on a baseplate with a camera so that the viewbox will be aligned for all measurements.

I.4 Results and Discussion: Deflection of a Steel-Cellulose Acetate Laminate

Results shown here are for experimental measurements from 3 laminates, two constructed with 102 micron steel beams (samples A and B) and the third with a 152 micron steel beam (sample C). Fig. AI-7 shows the bending curvature plots of the data. The samples reach equilibrium at approximately the same time, around 720 seconds (12 minutes). The data from samples A and B (constructed from 102 micron steel beams) are very similar, which gives an indication of reproducibility. Sample C (constructed from a 152 micron beam) has a lower curvature, which is expected, since the thicker beam will deflect less under a given stress.

Data was compared with the laminate model (Sec. I.2.1), using both estimated and independently measured parameters. The model fits the data very well for samples A and B up to 480 seconds. Using the same parameters except for the steel beam thickness, the model does not fit the data from sample C as well. In both cases, the model has significantly different equilibrium values, and reaches equilibrium much longer after the experimental data.

The inability of the model to fit both data sets indicates that the model is not valid for this system. The model can be fitted to the 100 micron beam data by adjusting the parameters. However, adjusting the only parameter that is different between the two sets (beam thickness) does not fit the second set. Modeling the deflection may be complicated because the cellulose acetate can behave viscoelastically. The stress in the cellulose acetate may relax with time, which would explain the leveling off of the data compared with the model. Eventually, the deflection of the laminate begins to decrease and the laminate becomes flat again.

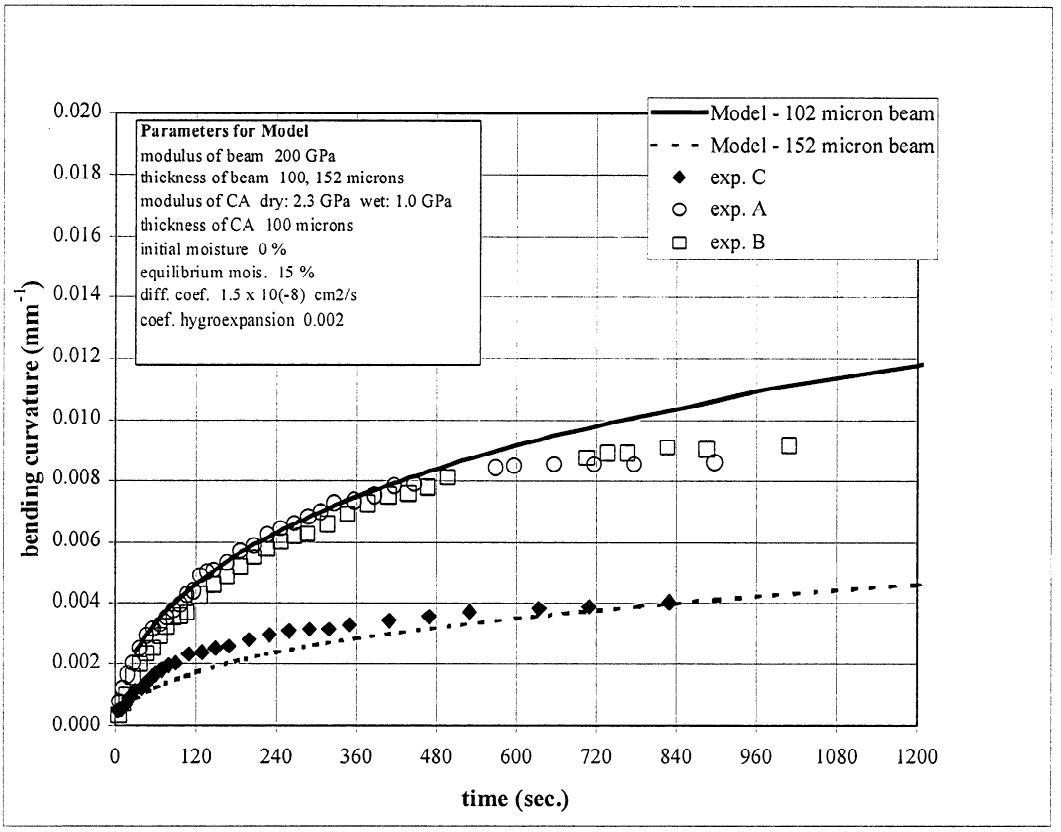

Figure AI-7: Experimental data for steel-cellulose acetate laminates compared with the theoretical model.

I.5 Conclusions

A theoretical model was used to describe the deflection of a steel-cellulose acetate laminate upon immersion in water. However, the model did not appear to describe the deflection accurately because the cellulose acetate appeared to be viscoelastic, while the model was for elastic materials. The experimental apparatus that was developed for measuring the deflection worked very well and should be suitable for other applications.

APPENDIX II: Standard Error of the Mean

The standard error of the mean with a (1 - α)100% confidence interval was calculated using the following equation (Walpole and Myers, 1989):

$$\bar{x} \pm t_{\alpha/2} \frac{s}{\sqrt{n}} \tag{AII-1}$$

where $\bar{x}$ is the mean, $t_{\alpha/2}$ is the t-value with $\nu = n - 1$ degrees of freedom, s is the standard deviation of the sample, and n is the sample size. The t-value was used because the variance, σ^2, of the population was unknown. For the segment length data, the mean and standard deviation were calculated from the length-weighted averages of the samples for each set. The standard error of the effective thickness was more complicated because it is the quotient of the average cross-sectional area divided by the average width (Eq. AI-2). The following equations were used to calculate the expected value, *E(z)*, and variance, *Var(z)* (Hahn and Shapiro, 1967). These could then be used in Eq. AI-1.

$$h = \frac{A}{w} \tag{AII-2}$$

$$z = f[x_1, x_2, \ldots] \tag{AII-3}$$

$$\bar{z} = E(z) = f[E(x_1), E(x_2), \ldots] \tag{AII-4}$$

$$s_z^2 = Var(z) = \sum_{i=1}^{n} \left(\frac{\partial f}{\partial x_i} \right)^2 Var(x_i) \tag{AII-5}$$

$$\bar{h} = \frac{\bar{A}}{\bar{w}} \tag{AII-6}$$

$$s_h^2 = \left(\frac{1}{\bar{w}} \right)^2 \cdot s_A^2 + \left(\frac{\bar{A}}{\bar{w}^2} \right)^2 \cdot s_w^2 \tag{AII-7}$$

APPENDIX III: Probability Distribution Curves

Histograms of the segment length were compared with theoretical probability distribution curves. The gamma and log-normal functions were investigated because they are functions that are bounded by zero, are skewed toward zero, and their parameters can be easily calculated from experimental data. The Weibull distribution, which is commonly used for fragmentation data, was not addressed because its parameters must be determined by either a solution of nonlinear equations or by a graphical procedure (Hahn and Shapiro, 1967).

The gamma distribution is described as a basic distribution for variables bounded at one side (Hahn and Shapiro, 1967). Theoretically, it gives the time required for a number of independent events to take place if the events occur at a constant rate. The density function is given by:

$$f(x) = \frac{1}{\beta^{\alpha}\Gamma(\alpha)} x^{\alpha-1} e^{-x/\beta} \qquad \text{(AIII-1)}$$

for $x \geq 0$ [f(x) = 0 elsewhere], $\alpha > 0$, and $\beta > 0$. The gamma parameters, α and β, can be calculated from the mean, $\bar{x}$, and variance, s^2, of experimental data (Walpole and Myers, 1989).

$$\alpha = \frac{\bar{x}^2}{s^2}$$
$$\beta = \frac{s^2}{\bar{x}} \qquad \text{(AIII-2)}$$

The log-normal distribution is the distribution for a variable whose logarithm follows a normal distribution (Hahn and Shapiro, 1967). It is described as a model for a process whose value results from the multiplication of many small errors. This distribution was used previously

by Epstein (1947) to theoretically describe the size distribution of a solid resulting from a crushing or grinding process. The density function is given by:

$$f(x) = \frac{1}{\sigma x\sqrt{2\pi}} \exp\left[-\frac{1}{2\sigma^2}(\ln x - \mu)^2\right] \qquad \text{(AIII-3)}$$

for $x \geq 0$ [f(x) = 0 elsewhere], $-\infty < \mu < \infty$, and $\sigma > 0$. The parameters, μ and σ, can also be calculated from the mean, $\bar{x}$, and variance, s^2, of experimental data (Hahn and Shapiro, 1967).

$$\mu = \ln \bar{x} - \tfrac{1}{2}\sigma^2$$
$$\sigma^2 = \ln\left(\frac{s^2}{\bar{x}^2} + 1\right) \qquad \text{(AIII-4)}$$

These distribution functions are compared with the histograms of the experimental data by determining the probability that x has a value within each size bin. The probability that x is between x_1 and x_2 (lower and upper limit of a size bin) is given as the difference of the cumulative values at the limits (Hahn and Shapiro, 1967):

$$\Pr(x_1 < x < x_2) = F(x_2) - F(x_1) \qquad \text{(AIII-5)}$$

where the cumulative values, $F(x_i)$, are determined from the density functions, $f(y)$:

$$F(x_i) = \Pr(x \leq x_i) = \int_0^{x_i} f(y)dy \qquad \text{(AIII-6)}$$

The cumulative functions are included with the Microsoft Excel spreadsheet program. These probabilities are plotted at the midpoint of each size bin and a smoothed line is drawn through the points.

The chi-squared goodness-of-fit test is used to compare the theoretical distributions with the experimental data (Hahn and Shapiro, 1967). The number (not percentage) of observed, M_i, and expected, E_i, values are compared for each size bin with at least 5 observations. The test statistic is given by:

$$X^2 = \sum \frac{(M_i - E_i)^2}{E_i} \qquad \text{(AIII-7)}$$

The chi-squared test is included with the Microsoft Excel spreadsheet program. In the figures, the percentage in parenthesis gives the probability that the data came from the given distribution. A higher percentage indicates a better fit.